Title
Nuclear VANGL2 Inhibits Mammary Differentiation

Author
Rubio, Stefany Alejandrina

Publication Date
2022

UNIVERSITY OF CALIFORNIA
SANTA CRUZ

NUCLEAR VANGL2 INHIBITS MAMMARY DIFFERENTIATION

A dissertation submitted in partial satisfaction
of the requirements for the degree of

DOCTOR IN PHILOSOPHY

in

MOLECULAR, CELL, AND DEVELOPMENTAL BIOLOGY

by

STEFANY A. RUBIO

September 2022

The Dissertation of Stefany A. Rubio
is approved:

Dr. Lindsay Hinck, Chair

Dr. Zhu Wang

Dr. William Sullivan

Peter Biehl
Vice Provost and Dean of Graduate Studies

Table of Contents

List of Figures

Abstract

NUCLEAR VANGL2 INHIBITS MAMMARY DIFFERENTIATION

Stefany Rubio

Mammals are defined by a unique tissue, the mammary glands, which secrete milk that feed their offspring. Even though a milk supply is vital to species' survival, the molecular mechanisms that regulate lactation remain obscure. Recent research shows that acquiring nutrients from mother's milk confers a lifetime of benefits, yet many women around the world are unable to produce sufficient milk to supply the needs of their infant. Establishing therapeutically targetable molecules that drive lactation promises to help women experiencing lactation insufficiency syndrome and expand the health of the population. In my thesis work, I show that the protein Van Gogh-like 2 (VANGL2) plays a novel role in the nucleus where it inhibits differentiation of mammary epithelial cells into milk producing alveolar cells. My data show that VANGL2, working in conjunction with the polycomb repressor protein BMI1, represses the transcription of pro-differentiation genes. Decreasing the nuclear localization of VANGL2 results in precocious differentiation and more milk. This research presents a novel role for VANGL2 in regulating gene transcription at a crucial point in tissue differentiation, making it an appealing clinical target for lactation insufficiency.

Acknowledgments

Thank you to Dr. Lindsay Hinck for the countless hours spent mentoring me throughout my seven years in graduate school. Thanks to the IBSC core directors, Bari Holm Nazario and Dr. Ben Abrams for supporting our research. To my partner and bioinformaticist, Chad Cockrum, thanks for the countless advice on experiments and for supporting me during our Ph.D. studies. To my Lopez and Cockrum family who always cheer me on through everything I chose to do in life. To my lab mates over the years, I learned so much from all of you. Thanks to everyone in the MCDB department for an enriching scientific training experience.

Chapter 1: VANGL2 in the mammary gland

The mammary gland is a specialized tissue that produces milk, which provides nutrients for the offspring of mammals. The milk is produced by the bilayered epithelia, comprising basal cells surrounding an inner layer of luminal cells, that grows from the nipple into the fat pad to generate a tree-like structure. Proper development of the mammary gland is important for carrying out this function (Macias, 2012). Underlying molecular and cellular mechanisms during the development of the mammary gland influence lactation; these include cell organization, proliferation and differentiation, stem cell maintenance, and the precise temporal regulation of gene expression (Lim, 2010). Investigating the biology of the cells that produce milk provides insights on how these cells work to generate milk, the specialized function of the mammary gland. The long-term goal of these investigations is to help women, who experience lactation insufficiency syndrome (LIS), benefit from targeted therapies that molecularly increase their milk production. This will decrease the reliance on artificial milk supplements.

The mammary gland is an organ that undergoes a host of changes postnatally. At birth, it is a rudimentary structure that will undergo dramatic growth only at puberty, when hormones drive a process called branching morphogenesis. At this point, the rudimentary buds at the tips of the ducts become terminal end buds that bifurcate through the stromal-rich mammary gland and bifurcating to generate the primary ductal structure (Paine, 2017; Macias, 2012). Secondary branches grow laterally and upon these branches there is tertiary budding. After puberty, these tertiary buds expand and contract with every estrus cycle. With pregnancy the epithelium undergoes another growth spurt driven by the hormonal changes occurring at this time. The tertiary buds elaborate into alveoli that will become the milk producing units of the mammary gland during lactation (Macias, 2012; Paine, 2017). At pregnancy, the mammary gland epithelium will undergo a massive expansion in preparation for lactation, termed the alveolar switch. This is a time when chromatin remodeling occurs alongside the synthesis of lactogenic proteins that aggregate in cytosolic lipid droplets (CIDs) in preparation for milk secretion into the lumen (Oakes, 2006; Russell, 2007; Gao, 2015; Monks, 2020). The mammary gland will go on to secrete milk that relies on continuous mechanical stimulation provided by oxytocin-induced contraction of the basal myoepithelial cells that form a basket-like net encircling milk-filled alveolar cells (Macias, 2012; Gimpl, 2001; Stevenson, 2020). Eventually, a lack of demand for milk will lead to the initiation of involution, a stage of remodeling that will phenotypically reverses the mammary gland into a virgin-like state characterized by a distinct gene expression profile, the involution swtich (Watson, 2011; Clarkson, 2003; Watson, 2011; Watson, 2006; Hughes, 2012; Campbell 2014). The fine orchestration of this massive tissue transformation and regeneration is one of the unique features of the mammary gland. The structural changes the mammary gland undergoes and how the extracellular space transforms to accommodate these needs is a poorly understood by mammary gland biologists.

Of the remarkable changes occurring in the postnatal mammary gland, lactation requires the most massive wave of proliferation accompanied by endoreplication that generates polyploid cells capable of the dedicated protein synthesis, which is required for milk production. Lactation is driven by specialized instructions that govern the cell proliferation and tissue changes required to generate the milk-producing structures or alveoli. Both epithelial cell populations, serving unique functions, are involved in these changes: the outer contractile myoepithelial cells (MyoECs) and the inner secretory luminal cells (LECs). MyoECs adopt two confirmations. They both surround the tubular “trunks” of the tree-like structures in an elongated pattern, and they adopt a basket-like pattern in acini stretching over the luminal cells and contracting to squeeze milk. The inner LECs line the lumen of ducts and secretory alveoli with alveolar LECs secreting milk into the lumen when the mammary gland undergoes lactation. There is tremendous remodeling of tissue that occurs with every pregnancy and the organization of these cells into their secretory structures relies on long range signals that dictate their polarity cues, mechanochemical shifts, and function. One important set of cues mediate the planar cell polarity (PCP) pathway and have been implicated in sending long range signals across the branching structures of epithelia, including the kidney, lung, and mammary gland (Smith, 2019; Godde, 2014; Baker, 2016; Yates, 2011; Davenport, 2011; Ramsbottom, 2014).

PCP refers to the organization of cells relative to the proximal-distal tissue plane; in the mammary gland the nipple is at the proximal end (Davenport, 2014; Vladar, 2009; Butler 2017). When mutations were introduced to the core PCP components (Prickle, Scribble, Flamingo/Celsr, Frizzled, Dishevelled, Diego), non-autonomous changes are observed (Adler, 2000; Gibbs, 2016; Guo, 2004; Yin, 2012). These mosaic, cell-mixing experiments suggested that PCP proteins are instruct cell behavior at the plasma membrane, and crosstalk within the intracellular space. With additional work, researchers concluded that long-range signals are propagated by this pathway (Hatakeyama, 2014; Aw, 2016). The core PCP proteins are asymmetrically organized in polarized cells, where the proximal accumulations of Vang and Pk are complementary to distal accumulations of Fz, Dsh and Dgo (Butler, 2017, Davenport 2014, Vladar, 2009; Zhang, 2009). Fz and Vang, which are transmembrane proteins, associate with physically linked Fmi homodimers that are established between the opposing plasma membranes at cell junctions. The distal, asymmetrical accumulations of Fmi and Fz are clustered through the cytosolic activity of Dsh and Dgo, whereas proximal Fmi and Vang complexes are enriched by Pk cytosolic activity (Beloit, 2012; Butler, 2017). During cell divisions daughter cells inherit the PCP components needed to retain polarity, including VANGL2, via endosomes (Heck, 2017; Smith, 2017). Thus, there is emerging knowledge that VANLG2 is localized to endosomes in different cell types (e.g., muscle, neurons, epithelia, and breast) and together these studies present a view that VANGL2 has an "intracellular life" beyond its well-established role at the plasma membrane (Puvirajesinghe, 2016).

The PCP pathway protein, Van Gogh-like 2 (VANGL2), is frequently expressed at the plasma membrane and studies show it functions in many biological processes (e.g., cell proliferation, orientation, organization, and self-renewal), tissue morphology, development, and regeneration (Davenport, 2014; Yin, 2012; Iliescu, 2011; Lake, 2009; Beloit, 2012; Poobalasingam, 2017; Ramsbottom, 2014; Roque, 2015). The transport of VANGL2 to the plasma membrane relies on its anterograde transport, from the ER/Golgi to the plasma membrane, via Sec24b+ endosomes that engage VANGL2 by a specific motif at its carboxyl terminus (C-terminus). A mutation within this locus, S464N, leads to the misfolding and degradation of VANGL2 via the endoplasmic reticulum associated degradation (ERAD) pathway (Merte, 2009). This mutation, also known as *Looptail* (*Vangl2*$^{Lp/Lp}$), was first identified in mice by Strong & Hollander (1949) because of the pigtail phenotype it produced and was mapped to the *Vangl2* gene fifty-two years later (Kibar et al. 2001, Murdoch et al. 2001a). The *Looptail* mutation leads to many developmental defects, including neural tube closure, CE extension, cystic renal defect, congenital heart disease, lung disease and breast cancer (Hatakeyama, 2014, Kibar, 2007; Lei, 2010; Goggolidou, 2013; Yates, 2011; Puvirajesinghe, 2016). Using Vangl2 mutant mice (*Vangl2*$^{Lp/Lp}$) we discovered that the cell membrane localization of VANGL2 is needed for proper mammary gland development. Some of the mammary gland developmental processes that we observed being affected are MyoEC and LEC organization, lumen size, and overall epithelia outgrowth. In the absence of pregnancy, we observed the intriguing development of acini-like structures of *Vangl2*$^{Lp/Lp}$ transplant outgrowths in comparison to wild type control transplants, but in these studies did not otherwise address the role VANGL2 plays in pregnancy and lactation. Thus, for the bulk of my thesis studies, I focused on advancing our knowledge about VANGL2 in the secretory alveolar cell lineage.

The orchestrated regulation of lactation genes relies on chromatin remodeling proteins and transcription factors that can temporally switch the state of gene expression. The polycomb repressive complex (PRC) is composed of two larger complexes, PRC1 and PRC2. In the PCR1 complex there is a noteworthy protein, BMI1, which is an E3 ubiquitin ligase protein that we see being co-regulated with VANGL2 (i.e., downregulated when VANGL2 expression decreases). In mammals, the PRC2 complex contains four core subunits, SUZ12, EED, EZH1, EZH2, the latter which catalyzes the di-/tri- methylation of lysine 27 of histone H3 (H3K27me 2/3) respectively (Chan, 2018). Where, H3K27me 2/3 are post-translational heterochromatin modifications that activate and silence gene transcription respectively. Together, these two complexes have the means to regulate the temporal genetic switches that the mammary gland requires to meet its functional needs. Functional studies have been performed to assess the role that BMI1 plays in regulating the development of the mammary gland epithelium (Paranjape, 2014; Pietersen, 2008). Researchers found that knocking-out *Bmi1* in mammary glands resulted in premature differentiation and that knock-down of Bmi1 in HC11 cells, a cell line used to model lactation, leads to increased production of the milk protein, β-Casein (CSN2) (Pietersen, 2008). When we compare the knock-out *Bmi1* mammary glands from this 2008 study with our $Vangl2^{Lp/Lp}$ mammary glands, we find a striking similarity between their phenotypes. This led us to ask how VANGL2 and BMI1 might be working together in the mammary gland to regulate cell differentiation.

Our work hinted that VANGL2 is more than just a plasma membrane protein functioning to regulate cell communication with other PCP proteins (Smith, 2019). Recent studies have also shown this to be the case, with many studies showing a rich "intracellular life" for VANGL2. For example, VANGL2 has been observed to be expressed in endosomes throughout the cytosol, near and away from the plasma membrane. Near the plasma membrane, VANGL2 is found in recycling endosomes or endosomes that are transporting it from the trans-Golgi. PCP signals are relayed via endosomes to daughter cells that are dividing from their parent cell (Heck, 2017). Where, VANGL2 expression is observed in Rab7+ endosomes, along with other PCP proteins CELSR1 and FZD6 (Heck, 2017). VANGL2 and FZD6 are also expressed in independent endosomes that are traveling to the plasma membrane from the ER via the trans-Golgi (Ma, 2018). These are a few examples of the VANGL2 cytosolic occupancy beyond the plasma membrane, but these cytosolic trafficking events contribute to its PCP roles. In contrast, other studies suggest that cytosolic VANGL2 has a role beyond the plasma membrane and the PCP pathway. Distant from the plasma membrane, VANGL2 has been identified in the perinuclear cloud of breast cancer cells. In the perinuclear cloud, VANGL2 is expressed in endosomes that co-express SQSTM1/p62, an E3 ubiquitin ligase that would typically engage in autophagy with its partner LC3-II. By engaging in these vesicles, VANGL2 and p62 communicate with the JNK pathway to upregulate cell proliferation (Puvirajesinghe, 2016). Our data, also suggests a role beyond PCP for VANGL2 and adds to its growing pleiotropic roles.

The perinuclear VANGL2 expression led us to analyze the protein sequence for clues about how VANGL2 may be sorted into these subcellular fates beyond the cell membrane. For example, proteins that are sorted into endosomes might contain information in their sequences that aid their sorting, such as a nuclear localization signal (NLS). Strikingly, analysis of the VANGL2 sequence revealed DNA binding sites at the N-terminus and C-terminus, where an NLS sequence is also located. To identify the DNA binding sites and NLS sequence, I used the DNABinder, cNLS Mapper, NLSradamus, and PredictNLS tools. This NLS sequence that was identified is recognized by the Importin α/β pathway that transports nuclear bound proteins to the nucleus using endosomes (Wang, 2010). Such NLS sequences show patterns of basic amino acid residues that loosely match two consensus sequences, K(K/R)X(K/R) AND $KRX_{10-12}KRXK$, termed monopartite and bipartite classical NLS (Kosugi, 2009; Ba, 2009). VANGL2 is a 521 amino acid protein, ~60 KDa, and the mouse and human predicted NLS for VANGL2 is ERRVRKRRAR, at amino acids 349-358 and following a more of a bipartite sequence. The discovery of this motif in zebra fish (Pan, 2014) and our identification in human and mouse VANGL2 led to my investigations surrounding its nuclear expression.

A nuclear function for the full length VANGL2 protein has never been established. While other transmembrane proteins have been found in the nucleus, my thesis presents the first data to show a component of the PCP/non-canonical WNT pathway in the nucleus. In the mammary gland, I posited that VANGL2 regulates the differentiation state of alveolar cells during lactogenesis. To test this hypothesis, I used a cell line, HC11 cells, that model lactation in vitro when exposed to lactogenic hormones (Dexamethasone, Insulin, and Prolactin). I analyzed the expression of VANGL2 throughout differentiation and observed VANGL2 leaving the nucleus of mammary gland cells along with the loss of Polycomb Repressive Complex (PRC) protein, BMI1. In non-differentiated states, we find VANGL2 and BMI1 inside the nucleus of HC11s. Thus, the two proteins may be serving as an ON/OFF switch for differentiation/lactation genes. My thesis work dives into the molecular mechanisms that regulate this expression pattern and furthers our understanding about how lactation genes may be regulated.

RESULTS

Vangl2$^{Lp/Lp}$ **outgrowths display supernumerary end buds and ectopic acini.**

Given that TEBs are the site of growth and proliferation in the mammary gland and VANGL2 is highly expressed in this region, we performed additional transplantation experiments to evaluate the postnatal consequences of VANGL loss-of-function in successful mammary outgrowths. We observed three distinct phenotypes in *Vangl2*$^{Lp/Lp}$ outgrowths (n = 20 WT/LP pairs) that were non-mutually exclusive. One phenotype was an abundance of end buds. We found that 45% (9/20) of *Vangl2*$^{Lp/Lp}$ outgrowths contained 6-fold more TEBs that were significantly larger compared to WT (Figure 1.1 A–C, I). Together, these findings suggest that VANGL2 is expressed in a gradient across the gland and loss of this graded expression enhances TEB formation.

A second phenotype (8/20) was the formation of premature acini (Figure 1.1 D, E, I, Supp. Figure 1.2 B). Our transplantation assays were performed such that WT fragments were contralaterally transplanted into the same mouse as *Vangl2*$^{Lp/Lp}$ tissue. Therefore, both tissues were exposed to the same hormonal environment, so this defect does not represent cyclic side branching. Nevertheless, we found that *Vangl2*$^{Lp/Lp}$ outgrowths contained twice as many acini per duct, compared to *WT* (Figure 1.1 D, E, I, Supp. Figure 1.2 B). To evaluate the morphology of these structures, we sectioned *WT* and *Vangl2*$^{Lp/Lp}$ tissue and immunostained with anti-CDH1, revealing a single layer of luminal cells surrounding a hollow lumen (Supp. Figure 1.2 D). In contrast, multiple layers of disorganized luminal cells frequently occluded *Vangl2*$^{Lp/Lp}$ acini (Supp. Figure 1.2 D). Thus, *WT* acini morphologically mimicked normal tertiary branching, whereas *Vangl2*$^{Lp/Lp}$ acini showed exuberant, disorganized, tertiary acini, despite being exposed to the same hormonal environment.

A third phenotype (6/20) was the presence of dilated ducts (Figure 1.1. G–I, Supp. Figure 1.2 C). We quantified the size of these ducts along their length by optically dividing each duct into horizontal sections using a grid and found that the average area of *Vangl2*$^{Lp/Lp}$ ducts was 3 times greater than *WT* (Figure 1.1 G). In addition to their increased size, *Vangl2*$^{Lp/Lp}$ ducts are also marked by pronounced constrictions along their lengths, giving the ducts a pinched appearance (Figure 1.1 H). In contrast, WT ducts are uniform in size; even if their area is expanding or contracting, the change is gradual (Figure 1.1 H). This difference was reflected in the quantification where we observed WT measurements clustering around 20 a.u., whereas *Vangl2*$^{Lp/Lp}$ measurements were more variable, echoing the abrupt changes in ductal size occurring over the length of *Vangl2*$^{Lp/Lp}$ ducts (Figure 1.1 G, H). Actin polymerization plays an important role in regulating lumen formation, and disorganized actin patterns have been observed in tubular and ductal organs of *Vangl2*$^{Lp/Lp}$ animals. To evaluate the filamentous actin cytoskeleton, we sectioned and phalloidin stained WT and *Vangl2*$^{Lp/Lp}$ tissue, observing irregular F-actin organization and reduced staining, particularly in the luminal compartment of *Vangl2*$^{Lp/Lp}$ ducts (Supp. Figure 1.2 E). In order to investigate whether this phenotype was due to a loss in PCP signaling, we examined the morphology of mammary glands from another PCP mutant mouse, Prickle2 (Pk2). PK2 is a cytoplasmic mediator of PCP signaling downstream of VANGL. Immunostaining of sectioned glands obtained from mature virgin mice with anti-PK2 antibodies revealed cytoplasmic and membrane staining in a pattern similar to VANGL2 expression (Supp. Figure 1.2 F). *Pk2* mutant mice have an embryonic lethal phenotype, resulting in termination around E3.5 before the mammary rudiment is formed. This prevented anlage rescue; therefore instead, we harvested mammary glands from adult virgin *WT* and *Pk2*$^{+/-}$ mice and performed whole mount analysis. Similar to *WT*, we found that *Pk2*$^{+/-}$ glands filled 100% of the fat pad (Supp. Figure 1.2 G), but *Pk2*$^{+/-}$ ducts were dilated except for constrictions, a phenotype also observed in *Vangl2*$^{Lp/Lp}$ outgrowths (Figure 1.1 G, H). Taken together these results suggest that loss of surface VANGL signaling regulates mammary ductal diameter.

Depletion of VANGL2 in basal versus luminal cell populations alters cyst formation.

Expression of VANGL2 in both the luminal and basal subpopulations, and the range of phenotypes displayed in the *Vangl2*$^{Lp/Lp}$ outgrowths, suggest that VANGL2 is governing different aspects of mammary gland development, perhaps by differentially influencing cell interactions and signaling in the distinct basal and luminal compartments of the mammary gland. To test this hypothesis, we used differential trypsinization to separate the two subpopulations and lentiviral-mediated knock down to reduce expression of *Vangl2* in either the basal, luminal or both cell types (Supp. Figure 1.1 A, B). By mixing knock down (KD) and WT subpopulations of cells and culturing them in Matrigel in the absence of growth factors, we generated mammary cysts that were mosaic in the expression of VANGL2, such that either the basal or luminal compartment was VANGL2-deficient (Figure 1.2 A). As a control, we also generated KD and WT cysts in which both or neither compartments were VANGL2-deficient (Figure 1.2 A). WT cells formed round cysts with approximately 3 protrusions, whereas KD cysts were half the size with no protrusions (Figure 1.2 B, C). KD of *Vangl2* in the luminal layer produced cysts similar in overall appearance to WT but 3-fold larger (Figure 1.2 A, B). Consistent with this increase in size, the KD cysts had 2-fold more cell protrusions (Figure 1.2 A, C). We immunostained these cysts with lineage markers K14 and K8 (Figure 1.2 D). Optical sections through these cysts show that, while WT cysts have clear lumens, *Vangl2* luminal KD cysts contained a filled lumen. These data show that loss of VANGL2 in the luminal population leads to disorganization, which echoes the TEB and acinar phenotypes in the *Vangl2*$^{Lp/Lp}$ full outgrowths and the narrowed lumen phenotype in the *MMTV-Cre;Vangl2*$^{flox/flox}$ glands. In contrast, KD of *Vangl2* in the basal layer, which contains a subpopulation of mammary stem cells, yielded cysts that resembled the full *Vangl2* KD cysts: half the size of WT with half the number of protrusions.

To further understand VANGL2 signaling in the mammary gland, we performed RT-qPCR on cDNA generated from *Vangl2*$^{Lp/Lp}$ and WT outgrowths and mammary tissue derived from *MMTV-Cre;Vangl2*$^{flox/flox}$ and *MMTV-Cre* only mice to evaluate the expression of genes encoding proteins that mediate the downstream signaling functions of VANGL2. To probe canonical WNT signaling, we measured expression of Axin2. In addition, as previous studies have shown that VANGL2 is a regulator of SHH, we evaluated SHH signaling by measuring the expression of downstream effectors *Bmi1* and *Ptch1* (Zhang, 2009). Although we found no change in *Axin2* or *Ptch1* expression in *Vangl2*$^{Lp/Lp}$ outgrowths compared to WT (Supp. Figure 1.1 C), we did observe a decrease in both *Axin2* and *Ptch1* in *MMTV-Cre;Vangl2*$^{flox/flox}$ compared to MMTV-Cre only mice (Supp. Figure 1.1 D). Importantly we observed a significant and consistent down regulation of *Bmi1* in both *Vangl2*$^{Lp/Lp}$ outgrowths and *MMTV-Cre;Vangl2*$^{flox/flox}$ mammary tissue compared to respective WT controls (Supp. Figure 1.1 C, D). BMI1 is part of the polycomb repressive complex 1 (PRC1) that maintains genes in a transcriptional repressive, quiescent state. Loss of its expression in *Vangl2*$^{Lp/Lp}$ tissue could explain our difficulty rescuing *Vangl2*$^{Lp/Lp}$ anlage, propagating the tissue in vivo and generating cysts with KD of *Vangl2* in the basal, stem cell containing compartment of the mammary gland. To investigate, we overexpressed *Bmi1* in *Vangl2* KD cysts and found that reconstitution of Bmi1 expression rescued the formation of cysts that were the same size as those generated with scrambled shRNA (Figure 1.1 E, F). These results show an inverse relationship between VANGL2 and *Bmi1* expression and suggest this may regulate the viability and outgrowth of mammary cells.

DISCUSSION

Although non-canonical WNT signaling has been shown to have an important role in normal mammary gland development, the mechanisms underlying the process remain elusive31. WNTs have both diverse and vast influences on mammary morphogenesis that can be explained by their ability to engage various receptors. In this study, we address non-canonical WNT/PCP signaling by directly examining the consequences of aberrant VANGL receptor function. We found that both VANGL1 and VANGL2 are expressed in the mammary gland and can be detected by immunostaining in the same cell populations; however, their loss-of-function phenotypes are different. We discovered that VANGL2 plays a more important role in both embryonic and postnatal gland development compared to VANGL1. We also observed distinct VANGL2 phenotypes depending on the genetic approach we used. Conditional loss of VANGL2 during puberty in the *MMTV-Cre; Vangl2*$^{flox/flox}$ mice led to defects in post-natal mammary duct morphogenesis whereas aberrant VANGL2 signaling during embryonic development in *Vangl2*$^{Lp/Lp}$ transplants resulted in a range of embryonic and differentiation defects consistent with impaired stem cell function.

One phenotype shared between both of our models is mis-regulation of ductal size. The non-canonical Wnt/PCP pathway regulates ductal diameter in a variety of epithelia by controlling two morphogenetic processes: convergent extension (CE) and oriented cell divisions (OCD). In this way, length-wise extension of tubules through

OCDs is balanced with the reorganization of cells along the width via CE, and, together, these mechanisms regulate ductal diameter. The *MMTV-Cre;Vangl2*$^{flox/flox}$ mammary glands display narrow ducts, whereas *Vangl2*$^{Lp/Lp}$ outgrowths contain ducts that are either uniformly wide or wide but marked with constrictions. These phenotypes suggest a role for VANGL2 in regulating mammary ductal diameter and are consistent with luminal width defects previously observed in Vangl2 mutant mice. For example, embryonic and adult airway lumen in the lungs of *Vangl2*$^{Lp/Lp}$ and *Vangl2*$^{Lp/+}$ mice, respectively, are absent or narrow[8,32], a phenotype that is reminiscent of the narrow lumens observed in *MMTV-Cre;Vangl2*$^{flox/flox}$ mammary glands. In contrast, dilated lumens are observed in both *Podocin-Cre;Vangl2*$^{flox/flox}$ and *Vangl2*$^{Lp/Lp}$ embryonic kidneys[7,9,10]. Recent studies show that OCDs are significantly off axis in *Vangl2*$^{Lp/Lp}$ embryonic kidneys compared to WT, leading to wider lumens 11. Thirty percent of *Vangl2*$^{Lp/Lp}$ mammary glands display dilated ducts, with some containing points of marked narrowing (Fig. 5F–H). Thus, it is likely that VANGL2 controls OCDs during mammary morphogenesis, but confirmation will require analysis of cell divisions and movements that occur over a longer time frame in the postnatal mammary gland. In addition, a number of other mechanisms have been implicated in mammalian lumen size control including RhoGTPase regulated actomyosin contractility, a known downstream effector of PCP signaling activity, and fluid-driven lumen expansion[33]. We did observe reduced proliferation in *MMTV-Cre;Vangl2*$^{flox/flox}$ mammary glands (Figure 3F), which may contribute to abnormal duct formation in the context of aberrant OCDs. In support of these findings in vivo, a similar reduction in proliferation with Vangl2 depletion was previously reported in two basal breast cancer lines3, and we observed that *Vangl2* deficiency, specifically in basal cells, impairs the growth of the entire cyst (Fig. 6A–C).

The fact that we observed different ductal diameter phenotypes in the *MMTV-Cre;Vangl2*$^{flox/flox}$ mammary gland versus *Vangl2*$^{Lp/Lp}$ outgrowths may be due to the timing of VANGL2 inactivation in these different models, the nature of the mutation, or both. Conditional loss of *Vangl2* was achieved using a Cre driver activated during puberty and, while it resulted in a major reduction in VANGL2 protein18, this decrease occurred after birth. In contrast, the endogenous missense mutation in the Looptail version of VANGL2 influences both embryonic and postnatal development. In the embryonic neuroepithelium and regenerating adult muscle, VANGL2 governs the asymmetric cell division of stem/progenitor cells by OCD[34,35]. In the mammary gland, VANGL2 is expressed in the stem cell-containing, basal cell population. Disruption of mammary stem cell self-renewal, expansion and/or cell fate acquisition during embryogenesis could alter the cellular dynamics of the developing gland and dramatically influence ductal morphogenesis in ways that are distinct from the loss of VANGL2 during puberty. Moreover, recent findings describe VANGL proteins functioning together in a heteromeric protein complex that prevents trafficking of VANGL1 to the cell surface in *Vangl2*$^{Lp/Lp}$ mice[22,36]. Indeed, we observed such disruption of VANGL1 localization at the cell borders of *Vangl2*$^{Lp/Lp}$ tissue (Supp.

Fig. 2B) This dual disruption can result in mislocalization of other PCP components such as Pk2, and lead to more dominant phenotypic traits22. Thus, the cell surface loss of both VANGL2 and VANGL1 from conception is likely to adversely affect both CE and OCD, and may explain the 50% decline in outgrowth potential, and the dilated ducts and other morphological phenotypes displayed in the successful *Vangl2*$^{Lp/Lp}$ outgrowths compared to *MMTV-Cre;Vangl2*$^{flox/flox}$ mammary glands.

A surprising result from this study was the identification of a link between the expression of BMI1 and VANGL2. We show that loss of VANGL2 reduces *Bmi1* expression and that overexpression of *Bmi1* rescues mammary cyst formation. BMI1 is involved in the self-renewal and maintenance of stem cells[37,38], and BMI1 KO mice have mammary glands that are stunted similar to *Vangl2*$^{Lp/Lp}$ outgrowths[38]. Furthermore, the stem cell-containing, basal cell population of the mammary gland expresses VANGL2 and previous studies have shown that VANGL2 is needed for symmetric expansion of stem cell division34,35. Because the Looptail (Vangl2$^{Lp/Lp}$) mutation is lethal, we performed anlage rescue, and this gave us our first indication of a potential stem cell defect in *Vangl2*$^{Lp/Lp}$ tissue. Compared to WT, there was a 50% reduced rescue of *Vangl2*$^{Lp/Lp}$ anlage, and a similar reduction in tissue viability with subsequent fragment passage. We also observed this decreased viability in our cyst assay when we reduced the level of Vangl2 expression in basal cells. We performed an in vivo serial transplantation assay that did not, however, reveal a difference in the passageability of WT and *Vangl2*$^{Lp/Lp}$ tissue. Although this result suggests that stem cells are not adversely affected by the loss of cell surface VANGL in *Vangl2*$^{Lp/Lp}$ tissue, an alternate explanation is that rescued tissue contains sufficient functional VANGL2 to preserve, at least some, mammary stem cell viability. Dosage sensitivity of the *Vangl2*^{Lp} allele is well documented[39], and supported in this study by the phenotypic heterogeneity observed in the mammary outgrowths produced by rescued anlage. Thus, it is tempting to speculate that VANGL2 may promote the expansion and/or self-renewal of mammary stem cells in the embryo and loss of VANGL2 signaling results in the depletion of the stem cell pool. Current experiments are aimed at understanding if VANGL2 is regulating stem cell number in the mammary gland using the null allele. Furthermore, it will be interesting to determine whether such deregulation of mammary stem cell self-renewal, expansion and/or cell fate acquisition by VANGL2 may contribute to its cancer modulatory effects.

METHODS

Mouse strains.

Vangl2$^{Lp/Lp}$ mice were obtained from Jackson Laboratory. Pk2+/− mice were generated as previously described[15,28]. Vangl2flox/flox mice were generated as previously described[18] and were crossed with Tg(MMTV-cre)1Mam (line A) provided by K Wagner[19]. This research was both approved by and conducted in accordance with the guidelines set by the University of California, Santa Cruz animal care committee (IACUC) and the Peter MacCallum Cancer Centre Animal Experimental Ethics. The research was conducted in compliance with National Health and Medical Research Council (Australia) guidelines.

Mammary gland transplantation.

Mammary anlage were dissected from Vangl2 Lp/Lp embryos, and transplanted into pre-cleared fat pads of Foxn1nu mice[40]. Contralateral outgrowths were harvested 12 weeks post-transplant and subjected to whole mount carmine staining. For serial studies, epithelial fragments were harvested and transplanted into a new host every 12 weeks.

In vivo branch quantification.

Primary branches were defined as ducts extending from the site of transplantation and terminating in an end bud. Secondary and tertiary branches were defined as branches extending from primary ducts or secondary branches, respectively. Branch number was quantified by tracing the primary ductal structure and counting the number of primary ducts and secondary/tertiary branches in Fiji (Ref 41).

RNA extraction and RT-qPCR.

Total RNA was isolated from MEC and LEC primary cell fractions (separated as described29) or from FACS-purified basal (Lin_CD24 + CD29-high) and luminal (Lin_CD24 + CD29low) cells using TRIzol reagent (Invitrogen) and prepared as previously described29. cDNA was prepared from 1 μg RNA using an iScript cDNA synthesis kit (Bio-Rad). RT-qPCR was performed in triplicate using LightCycler 480 SYBR Green I Master (Roche) and quantified using either Rotor Gene 6000 real-time PCR machine and software or Bio-Rad CFX Connect Real-Time System and CFX Manager software (Bio-Rad). Samples were normalised to GAPDH and expression levels calculated using the 2−ΔCt method. Real-time primers listed in S1 Table. Results were normalized to that of Gapdh.

Transduction of primary mammary epithelial cells.

Luminal and myoepithelial primary MECs were isolated by differential trypsinization as previously described[29]. Next, transduction of primary MECs was performed as described previously[42]. Single MECs were seeded at a density of 500,000 cells in a 24-well low-attachment plate and infected at an MOI of 30 with designated lentivirus in 800 μl of growth media. Cells were infected overnight for ∼16 h and washed three times with PBS and re-plated.

Primary mouse mammary epithelial cell cyst assay.

3D cultures were generated using the “on top” Matrigel method as previously described[43]. Briefly, transduced luminal and myoepithelial cells were trypsinized into a single cells suspension. The cells were then mixed in a 1:4 myoepithelial: luminal ratio and seeded at a final density of 25,000 cells on Matrigel-coated 8 well chamber slides. Cells were allowed to attach to the surface of the Matrigel for 30 mins at 37°C. A final volume of 10% Matrigel in growth media was added to the cells after attachment. Cells were imaged and analyzed for cyst formation after 72 hrs.

Statistical analysis.

Statistical analyses (Student’s t-test and ANOVA) were conducted on Graphpad Prism. Significance is indicated as *$p < 0.05$, **$p < 0.01$, ***$p < 0.001$, ****$p < 0.0001$. Bars represent SEM.

FIGURES

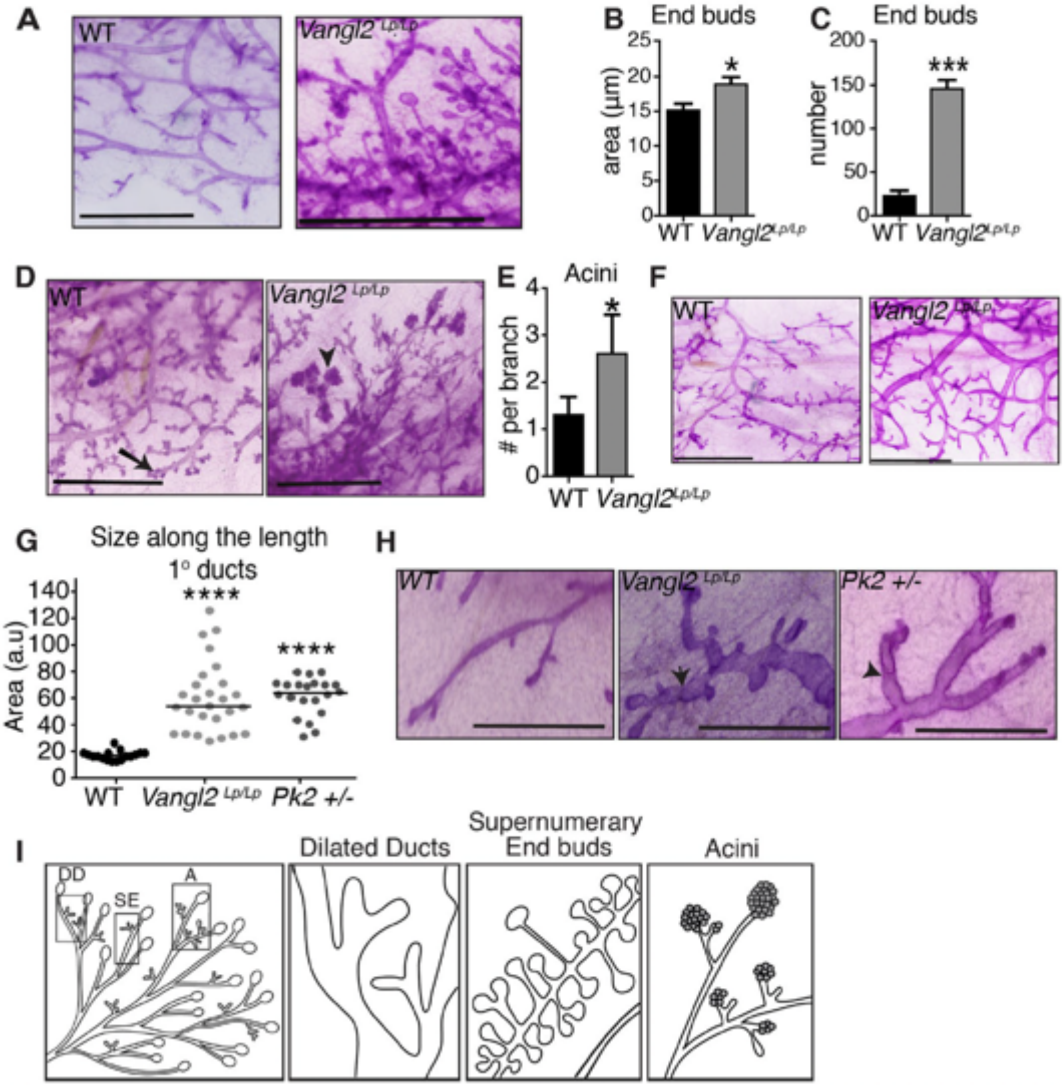

Figure 1.1: ***Vangl2*$^{Lp/Lp}$ outgrowths display distinct morphological defects.**

(A) Magnified view of supernumerary end buds in *Vangl2*$^{Lp/Lp}$ tissue from carmine stained, contralaterally transplanted WT and *Vangl2*$^{Lp/Lp}$ outgrowths 12 weeks post-transplantation; WT outgrowth contains no supernumerary end buds. Quantification of the area (B) and number (C) of end buds in WT and *Vangl2*$^{Lp/Lp}$ outgrowths. (D) Magnified view of acini in *Vangl2*$^{Lp/Lp}$ tissue from carmine stained, contralaterally transplanted *Vangl2*$^{Lp/Lp}$ tissue; WT outgrowth contains no acini. Arrow shows tertiary branching. Arrowhead denotes acinar structure. (E) Quantification of the number of acini in WT and *Vangl2*$^{Lp/Lp}$ outgrowths. (F) Magnified view of dilated ducts in tissue from carmine stained, contralaterally transplanted WT and *Vangl2*$^{Lp/Lp}$ outgrowths, harvested at 12 weeks; WT outgrowth shows smooth ductal borders with no constrictions. (G) Quantification of ductal size in WT, *Vangl2*$^{Lp/Lp}$ and *Pk2*$^{+/-}$ tissue (n = 10 ducts from 3 mice per genotype). (H) Representative images of carmine stained WT outgrowth, *Vangl2*$^{Lp/Lp}$ outgrowth and *Pk2*$^{+/-}$ ducts and displaying pinched ductal phenotype. Arrows denote constrictions. (I) Cartoon representation of the distinct phenotypes observed in *Vangl2*$^{Lp/Lp}$ outgrowths: DD, dilated ducts; SE, supernumerary end buds; A, acini. Scale bars represent 1.5 mm. Data are represented as mean ± SEM. Students t-test $^{*}p < 0.05$, $^{***}p < 0.001$, and $^{****}p < 0.0001$.

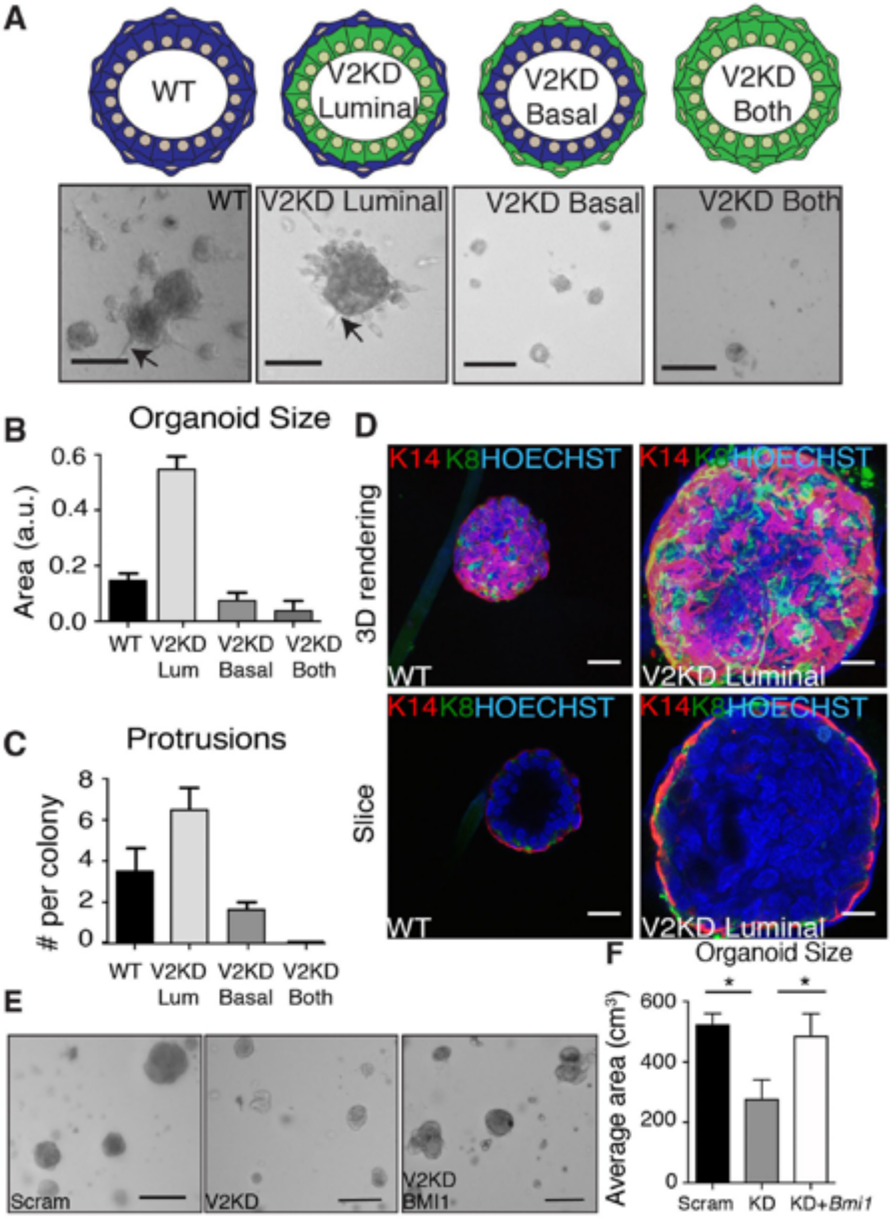

Figure 1.2 Knockdown of *Vangl2* in the basal versus luminal layers of cysts alter morphology.

(A) Schematic (top) and representative images (bottom) of mosaic cysts after 4 days in culture. Quantification of cyst size (B) and number of protrusions (C) in the mosaic cysts. (D) Immunostaining of K14 (red) and K8 (green) showing the surface (top) or inside (bottom) of WT or mosaic cysts with *Vangl2* knocked down in only luminal cells. Representative images (E) and quantification (F) of rescue of *Vangl2* KD cyst size with overexpression of Bmi1. n = 3 biological replicates. Scale bars represent 20 µm. Data are represented as mean ± SEM. Students t-test *$p < 0.05$.

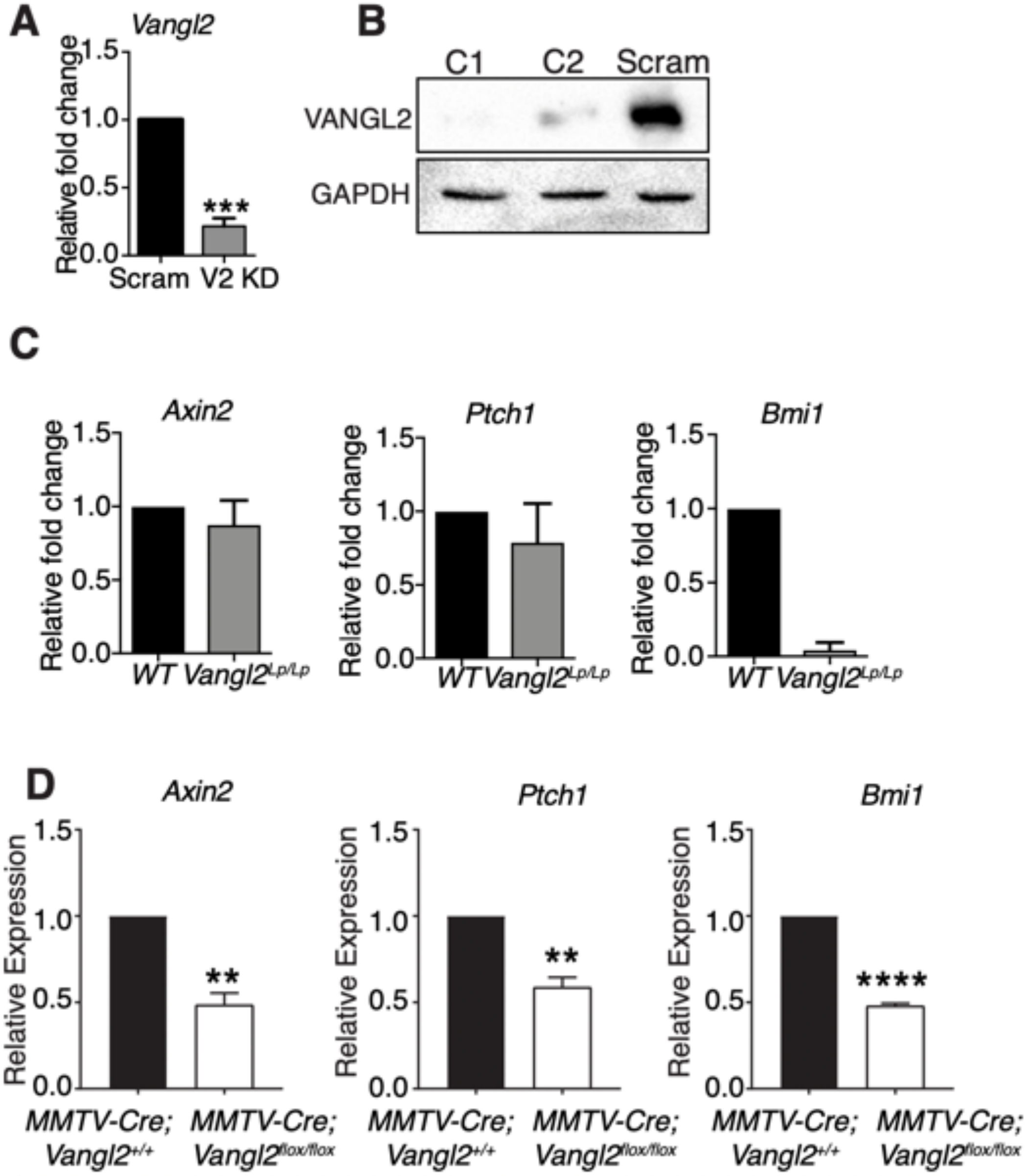

Supplemental Figure 1.1: Depletion of VANGL2 in basal versus luminal cell populations reduces Bmi1 expression.

(A) RT-qPCR analysis of *Vangl2* mRNA levels in WT and *Vangl2* knockdown primary cells. (B) Representative immunoblots of VANGL2 and GAPDH (control) in primary cells transduced with two constructs (C1, C2) to knockdown *Vangl2* (n=3). (C) qRT- PCR analysis of *Axin2*, *Ptch2* and *Bmi1* expression in WT and *Vangl2Lp/Lp* outgrowths. (D) qRT- PCR analysis of *Axin2, Ptch2* and *Bmi1* expression in *MMTV-Cre;Vangl*$^{flox/flox}$ mammary glands compared to Cre only control. n=3 biological replicates. Data are represented as mean ± SEM.

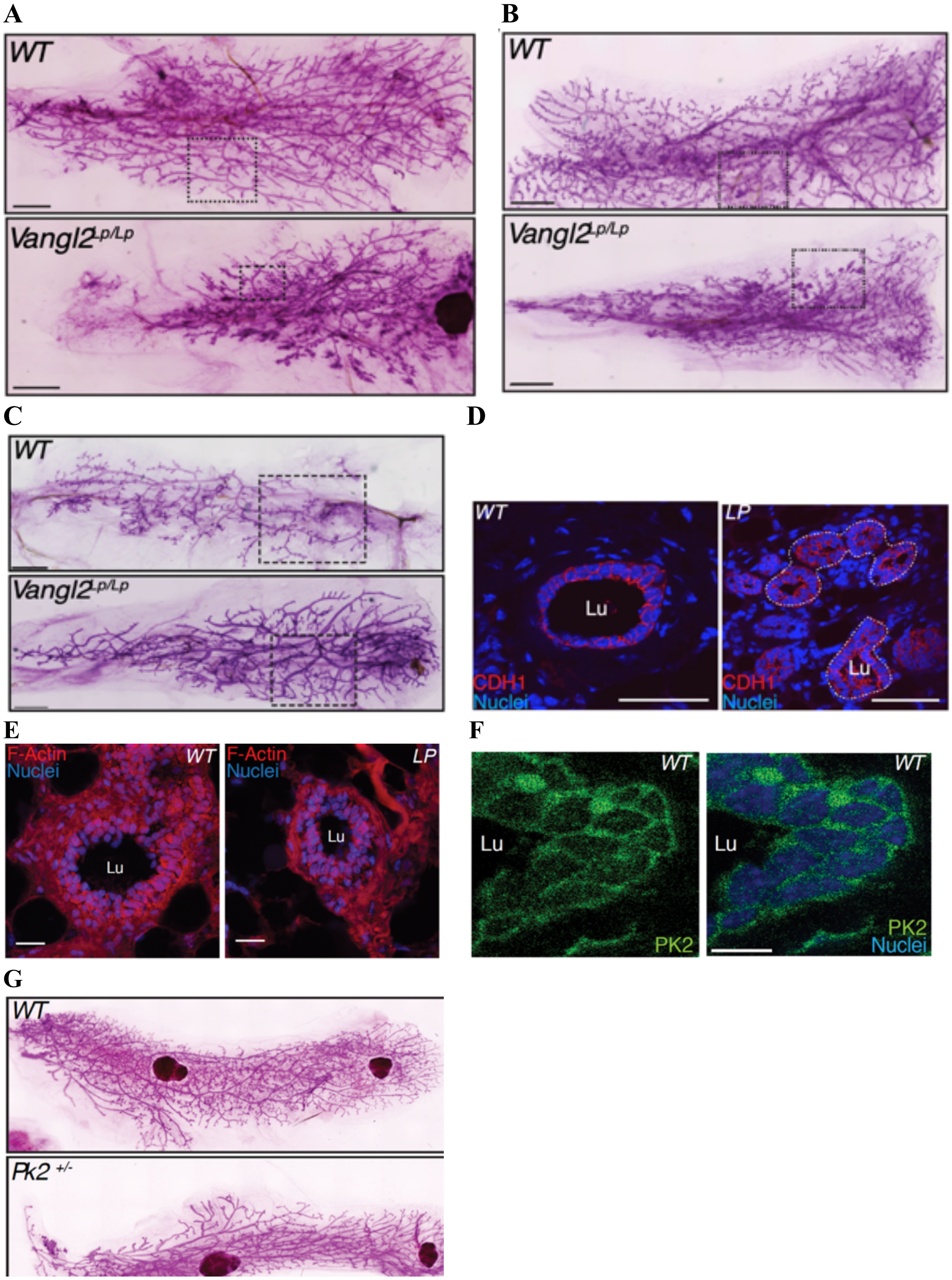

Supplemental Figure 1.2: VANGL loss of function phenotypes in the mammary gland phenocopy PCP defects.

(A-B) Representative whole mount images of contralaterally transplanted, carmine stained WT and *Vangl2*$^{Lp/Lp}$ outgrowths 12 weeks post-transplantation, showing supernumerary end buds (A) and acini (B). (C) Representative whole mount images of contralaterally transplanted, carmine stained WT and *Vangl2*$^{Lp/Lp}$ outgrowths 12 weeks post-transplantation, showing dilated ducts. (D) CDH1 immunostaining (red) of WT and *Vangl2*$^{Lp/Lp}$ tissue showing altered morphologyin *Vangl2*$^{Lp/Lp}$ ducts. (E) Phalloidin (red) staining in WT and *Vangl2*$^{Lp/Lp}$ ducts. (F) Immunostaining of WT 8-week tissue showing PK2 cytoplasmic and membrane localization in mammary ducts. (G) Representative whole mount images of carmine stained *Pk2*$^{+/-}$ outgrowths 12 weeks post-transplantation display dilated ducts compared to WT control. Lu denoted lumen. Scale bars represent 1.5mm (A, B, C, G) and 20μm (D, E, F).

REFERNCES

1. Lange A, Mills RE, Lange CJ, Stewart M, Devine SE, Corbett AH: J Biol Chem 2007, 282(8):5101-5. Epub 2006 Dec 14.

2. Poon IK, Jans DA: Regulation of nuclear transport: central role in development and transformation? Traffic 2005, 6(3):173-86.

3. Puvirajesinghe, T. M. et al. Identification of p62/SQSTM1 as a component of non-canonical Wnt VANGL2-JNK signalling in breast cancer. Nat Commun 7, 10318, https://doi.org/10.1038/ncomms10318 (2016).

4. Macias, H. & Hinck, L. Mammary gland development. Wiley Interdiscip Rev Dev Biol 1(4), 533–57 (2012)

5. Alexander, C. M., Goel, S., Fakhraldeen, S. A. & Kim, S. Wnt signaling in mammary glands: plastic cell fates and combinatorial signaling. Cold Spring Harb Perspect Biol 4, https://doi.org/10.1101/cshperspect.a008037 (2012)

6. Devenport, D. The cell biology of planar cell polarity. J Cell Biol 207, 171–179, https://doi.org/10.1083/jcb.201408039 (2014).

7. Yates, L. L. et al. The planar cell polarity gene Vangl2 is required for mammalian kidney-branching morphogenesis and glomerular maturation. Hum Mol Genet 19, 4663–4676, https://doi.org/10.1093/hmg/ddq397 (2010).

8. Yates, L. L. et al. The PCP genes Celsr1 and Vangl2 are required for normal lung branching morphogenesis. Hum Mol Genet 19, 2251–2267, https://doi.org/10.1093/hmg/ddq104 (2010).

9. Babayeva, S., Zilber, Y. & Torban, E. Planar cell polarity pathway regulates actin rearrangement, cell shape, motility, and nephrin distribution in podocytes. Am J Physiol Renal Physiol 300, F549–560, https://doi.org/10.1152/ajprenal.00566.2009 (2011).

10. Rocque, B. L. et al. Deficiency of the planar cell polarity protein Vangl2 in podocytes affects glomerular morphogenesis and increases susceptibility to injury. J Am Soc Nephrol 26, 576–586, https://doi.org/10.1681/ASN.2014040340 (2015).

11. Kunimoto, K. et al. Disruption of Core Planar Cell Polarity Signaling Regulates Renal Tubule Morphogenesis but Is Not Cystogenic. Curr Biol 27, 3120–3131 e3124, https://doi.org/10.1016/j.cub.2017.09.011 (2017).

12. Lim, E. et al. Transcriptome analyses of mouse and human mammary cell subpopulations reveal multiple conserved genes and pathways. Breast Cancer Res 12, R21, https://doi.org/10.1186/bcr2560 (2010).

13. Devenport, D., Oristian, D., Heller, E. & Fuchs, E. Mitotic internalization of planar cell polarity proteins preserves tissue polarity. Nat Cell Biol 13, 893–902, https://doi.org/10.1038/ncb2284 (2011).

14. Gao, B. et al. Wnt signaling gradients establish planar cell polarity by inducing Vangl2 phosphorylation through Ror2. Dev Cell 20, 163–176, https://doi.org/10.1016/j.devcel.2011.01.001 (2011).

15. Vladar, E. K., Bayly, R. D., Sangoram, A. M., Scott, M. P. & Axelrod, J. D. Microtubules enable the planar cell polarity of airway cilia. Curr Biol 22, 2203–2212, https://doi.org/10.1016/j.cub.2012.09.046 (2012).

16. Kibar, Z. et al. Identification of a new chemically induced allele (Lp(m1Jus)) at the loop-tail locus: morphology, histology, and genetic mapping. Genomics 72, 331–337, https://doi.org/10.1006/geno.2000.6493 (2001).

17. Kibar, Z. et al. Ltap, a mammalian homolog of Drosophila Strabismus/Van Gogh, is altered in the mouse neural tube mutant Looptail. Nat Genet 28, 251–255, https://doi.org/10.1038/90081 (2001).

18. Ramsbottom, S. A. et al. Vangl2-regulated polarisation of second heart field-derived cells is required for outflow tract lengthening during cardiac development. PLoS Genet 10, e1004871, https://doi.org/10.1371/journal.pgen.1004871 (2014).

19. Wagner, K. U. et al. Cre-mediated gene deletion in the mammary gland. Nucleic Acids Res 25, 4323–4330 (1997).

20. Mailleux, A. A., Overholtzer, M. & Brugge, J. S. Lumen formation during mammary epithelial morphogenesis: insights from in vitro and in vivo models. Cell Cycle 7, 57–62, https://doi.org/10.4161/cc.7.1.5150 (2008).

21. Strong, L. & Hollander, W. Hereditary loop-tail in the house mouse accompanied by imperforate vagina and craniorachischisis when homozygous. J Hered 40, 329–334 (1949).

22. Yin, H., Copley, C. O., Goodrich, L. V. & Deans, M. R. Comparison of phenotypes between different vangl2 mutants demonstrates dominant effects of the Looptail mutation during hair cell development. PLoS One 7, e31988, https://doi.org/10.1371/journal.pone.0031988 (2012).
23. Iliescu, A., Gravel, M., Horth, C., Kibar, Z. & Gros, P. Loss of membrane targeting of Vangl proteins causes neural tube defects. Biochemistry 50, 795–804, https://doi.org/10.1021/bi101286d (2011).

24. Deome, K. B., Faulkin, L. J. Jr., Bern, H. A. & Blair, P. B. Development of mammary tumors from hyperplastic alveolar nodules transplanted into gland-free mammary fat pads of female C3H mice. Cancer Res 19, 515–520 (1959).

25. Harburg, G. et al. SLIT/ROBO2 signaling promotes mammary stem cell senescence by inhibiting Wnt signaling. Stem Cell Reports 3, 385–393, https://doi.org/10.1016/j.stemcr.2014.07.007 (2014).

26. Daniel, C. W. Finite growth span of mouse mammary gland serially propagated in vivo. Experientia 29, 1422–1424 (1973).

27. Nagaoka, T. et al. The Wnt/planar cell polarity pathway component Vangl2 induces synapse formation through direct control of N-cadherin. Cell Rep 6, 916–927, https://doi.org/10.1016/j.celrep.2014.01.044 (2014).

28. Tao, H. et al. Nuclear localization of Prickle2 is required to establish cell polarity during early mouse embryogenesis. Dev Biol 364,138–148, https://doi.org/10.1016/j.ydbio.2012.01.025 (2012).

29. Macias, H. et al. SLIT/ROBO1 signaling suppresses mammary branching morphogenesis by limiting basal cell number. Dev Cell 20, 827–840, https://doi.org/10.1016/j.devcel.2011.05.012 (2011).

30. Zhang, Y. & Levin, M. Left-right asymmetry in the chick embryo requires core planar cell polarity protein Vangl2. Genesis 47, 719–728, https://doi.org/10.1002/dvg.20551 (2009).

31. Yu, Q. C., Verheyen, E. M. & Zeng, Y. A. Mammary Development and Breast Cancer: A Wnt Perspective. Cancers (Basel)8, (2016).

32. Poobalasingam, T. et al. Heterozygous Vangl2(Looptail) mice reveal novel roles for the planar cell polarity pathway in adult lung homeostasis and repair. Dis Model Mech 10, 409–423, https://doi.org/10.1242/dmm.028175 (2017).

33. Navis, A. & Bagnat, M. Apicobasal Polarity and Lumen Formation During Development. Cell Polarity 2: Role in Development and Disease, 67–92, https://doi.org/10.1007/978-3-319-14466-5_3 (2015).

34. Lake, B. B. & Sokol, S. Y. Strabismus regulates asymmetric cell divisions and cell fate determination in the mouse brain. J Cell Biol 185, 59–66, https://doi.org/10.1083/jcb.200807073 (2009).

35. Le Grand, F., Jones, A. E., Seale, V., Scime, A. & Rudnicki, M. A. Wnt7a activates the planar cell polarity pathway to drive the symmetric expansion of satellite stem cells. Cell Stem Cell 4, 535–547, https://doi.org/10.1016/j.stem.2009.03.013 (2009).

36. Belotti, E. et al. Molecular characterisation of endogenous Vangl2/Vangl1 heteromeric protein complexes. PLoS One 7, e46213, https://doi.org/10.1371/journal.pone.0046213 (2012).

37. Paranjape, A. N. et al. Bmi1 regulates self-renewal and epithelial to mesenchymal transition in breast cancer cells through Nanog. BMC Cancer 14, 785, https://doi.org/10.1186/1471-2407-14-785 (2014).

38. Pietersen, A. M. et al. Bmi1 regulates stem cells and proliferation and differentiation of committed cells in mammary epithelium. Curr Biol 18, 1094–1099, https://doi.org/10.1016/j.cub.2008.06.070 (2008).

39. Copp, A. J., Checiu, I. & Henson, J. N. Developmental basis of severe neural tube defects in the loop-tail (Lp) mutant mouse: use of microsatellite DNA markers to identify embryonic genotype. Dev Biol 165, 20–29, https://doi.org/10.1006/dbio.1994.1230 (1994).

40. Young, L. J. T. The Cleared Mammary Fat Pad and the Transplantation of Mammary Gland Morphological Structures and Cells. (Kluwer Academic/Plenum Press, 2000).

41. Schindelin, J. et al. Fiji: an open-source platform for biological-image analysis. Nature methods 9, 676–682, https://doi.org/10.1038/nmeth.2019 (2012).

42. Welm, B. E., Dijkgraaf, G. J., Bledau, A. S., Welm, A. L. & Werb, Z. Lentiviral transduction of mammary stem cells for analysis of gene function during development and cancer. Cell Stem Cell 2, 90–102, https://doi.org/10.1016/j.stem.2007.10.002 (2008).

43. Lee, G. Y., Kenny, P. A., Lee, E. H. & Bissell, M. J. Three-dimensional culture models of normal and malignant breast epithelial cells. Nature methods 4, 359–365, R345–356, https://doi.org/10.1530/ERC-14-0141 (2007).

44. Russell TD, Schaack J, Orlicky DJ, Palmer C, Chang BH, Chan L, McManaman JL. Adipophilin regulates maturation of cytoplasmic lipid droplets and alveolae in differentiating mammary glands. J Cell Sci. 2011 Oct 1;124(Pt 19):3247-53. doi: 10.1242/jcs.082974.

45. Gao Q, Goodman JM. The lipid droplet-a well-connected organelle. Front Cell Dev Biol. 2015 Aug 12;3:49. doi: 10.3389/fcell.2015.00049.

46. Monks J, Ladinsky MS, McManaman JL. Organellar Contacts of Milk Lipid Droplets. Contact (Thousand Oaks). 2020 Jan-Dec;3:10.1177/2515256419897226. doi: 10.1177/2515256419897226. Epub 2020 Jan 23.

47. Gimpl G, Fahrenholz F. The oxytocin receptor system: structure, function, and regulation. Physiol Rev. 2001 Apr;81(2):629-83. doi:10.1152/physrev.2001.81.2.629.

48. Stevenson AJ, Vanwalleghem G, Stewart TA, Condon ND, Lloyd-Lewis B, Marino N, Putney JW, Scott EK, Ewing AD, Davis FM. Multiscale imaging of basal cell dynamics in the functionally mature mammary gland. Proc Natl Acad Sci U S A. 2020 Oct 27;117(43):26822-26832. doi: 10.1073/pnas.2016905117. Epub 2020 Oct 8.

49. Clarkson RW, Watson CJ. Microarray analysis of the involution switch. J Mammary Gland Biol Neoplasia. 2003 Jul;8(3):309-19. doi: 10.1023/b:jomg.0000010031.53310.92.

50. Watson CJ, Kreuzaler PA. Remodeling mechanisms of the mammary gland during involution. Int J Dev Biol. 2011;55(7-9):757-62. doi: 10.1387/ijdb.113414cw. PMID: 22161832.

51. Watson CJ. Involution: apoptosis and tissue remodelling that convert the mammary gland from milk factory to a quiescent organ. Breast Cancer Res. 2006;8(2):203. doi: 10.1186/bcr1401. Epub 2006 Apr 10.

52. Hughes K, Watson CJ. The role of Stat3 in mammary gland involution: cell death regulator and modulator of inflammation. Horm Mol Biol Clin Investig. 2012 Jun;10(1):211-5. doi: 10.1515/hmbci-2012-0008.

53. Hughes K, Watson CJ. The spectrum of STAT functions in mammary gland development. JAKSTAT. 2012 Jul 1;1(3):151-8. doi: 10.4161/jkst.19691.

54. Campbell JJ, Botos LA, Sargeant TJ, Davidenko N, Cameron RE, Watson CJ. A 3-D in vitro co-culture model of mammary gland involution. Integr Biol (Camb). 2014 Jun;6(6):618-26. doi: 10.1039/c3ib40257f. PMID: 24722402.

55. Vladar EK, Antic D, Axelrod JD. Planar cell polarity signaling: the developing cell's compass. Cold Spring Harb Perspect Biol. 2009 Sep;1(3):a002964. doi: 10.1101/cshperspect.a002964.
56. Gibbs BC, Damerla RR, Vladar EK, Chatterjee B, Wan Y, Liu X, Cui C, Gabriel GC, Zahid M, Yagi H, Szabo-Rogers HL, Suyama KL, Axelrod JD, Lo CW. Prickle1 mutation causes planar cell polarity and directional cell migration defects associated with cardiac outflow tract anomalies and other structural birth defects. Biol Open. 2016 Feb 16;5(3):323-35. doi: 10.1242/bio.015750.

Chapter 2: Nuclear VANGL2 Inhibits Mammary Differentiation

INTRODUCTION

The mammary gland (MG) is a tissue that defines the *Mammalia* class of animals because the ability to lactate is crucial for the survival of most mammalian offspring. This gland is composed of bi-layered epithelial ducts that form a tree-like structure by growing from the nipple into the adipocyte-rich stroma. These ducts branch via end bud bifurcation, which lays down the primary ductal architecture; secondary side branching fills the spaces in-between. In response to hormones over the estrus cycle, short tertiary side-branches form and should a pregnancy occur, prodigious cell proliferation and differentiation produces sphere-like alveoli at the termini of these tertiary branches. These alveolar structures are composed of a single layer of polarized, milk-producing luminal epithelial cells, surrounded by a single net-like layer of myoepithelial cells that will eventually contract to squeeze milk into the lumen. The changes in MG form and function during pregnancy require massive remodeling, raising the question of how this growth, organization and differentiation of cells is coordinated to generate these specialized milk-producing structures.

Planar cell polarity (PCP) refers to the alignment and organization of cells relative to the proximal-distal tissue plane. Van Gogh like proteins (Vangl1 and Vangl2) are members of a suite of evolutionarily conserved, core PCP proteins that are characterized by asymmetric localization patterns in many tissues. The asymmetric localization of these core proteins depends on their differential trafficking that is highly regulated both from the trans Golgi network (TGN) following their synthesis and from the plasma membrane when VANGL2 is internalized and redistributed during tissue morphogenesis and cell division (Merte, 2010; Kowalczyk, 2021, Mahaffey, 2013; Devenport, 2011; Heck, 2017). More recently, a role for VANGL2 has been identified in controlling chaperone-mediated autophagy in the lysosome to block osteogenesis by binding LAMP2A and preventing the selective degradation of OB-lineage-inhibiting factors (Gong, 2021). Furthermore, there have been reports of VANGL2 in perinuclear endocytic vesicles in a variety of contexts including a breast cancer cell line, hUVECs under low fluid shear stress, in complexes with the cytoplasmic scaffold protein GIPC, and when induced by either the depletion of nucleocytoplasmic shuttling protein, Dapper1 or the adapter protein 3 (Sheng, 2022, Puvirajesinghe, 2016; Giese, 2012; Hagenmueller, 2014; Tower-Gilchrist, 2019). Taken together, these studies suggest that in addition to the key role VANGL2 plays in organizing planar cell polarity on the plasma membrane, it has yet undiscovered roles within the membranous compartments of the cell.

It is now well established that transmembrane proteins, including growth factor and G-protein coupled receptors are trafficked into the nucleus where they participate in not only the regulation of specific target gene transcription, but also in a wide range of processes, including DNA replication, DNA repair and RNA metabolism (Planque, 2006). We previously showed that the Vangl2 is required for normal MG development. Loss of *Vangl2* function by either conditional knock-out or by missense mutation (*Vangl2*$^{LP/LP}$), which disrupts trafficking to the plasma membrane, results in several, incompletely penetrant morphological phenotypes that in the virgin animal include disorganized, exuberant tertiary alveolar-like structures, suggesting a role for VANGL2 in regulating alveolar differentiation (Smith, 2019). We also observed significant downregulation of *Bmi1* in both *Vangl2*$^{Lp/Lp}$ outgrowths and *MMTV-Cre;Vangl2*$^{fl/fl}$ mammary tissue. BMI1 is a major component of the polycomb group complex 1 (PRC1) that functions in the nucleus as an epigenetic repressor through chromatin remodeling (Li, 2014; Guo, 2011). In the MG, loss of *Bmi1* results in the formation of premature alveolar-like structures in the virgin animal, echoing the phenotype observed in *Vangl2*$^{Lp/Lp}$ outgrowths. The regulation of Bmi1 expression by Vangl2 and the convergence of their loss-of-function phenotypes raised the possibility of a nuclear function for VANGL2 in directly repressing the transcription of genes governing alveologenesis through its influence on BMI1. Here, we identify VANGL2 in the nucleus of mammary cells and show a role for nuclear localized VANGL2 in restricting alveolar differentiation by regulating BMI1 levels.

RESULTS

VANGL2 localizes to the nucleus in HCC1569 cells.

To investigate the subcellular localization of VANGL2, we initially turned to HCC1569 cells, a highly proliferative, HER2+ breast cancer cell line that expresses high levels of *Vangl2* (Uhlen, 2015, Dai, 2017). We immunostained these cells for VANGL2, E-cadherin (CDH1), Lamin B-1 (LMNB1), collecting a z-stack of images that allowed us to identify and focus on the mid-plane of the nucleus. We observed CDH1 clearly outlining the cell membrane where it co-localizes with VANGL2 (Fig. 1 A). We calculated the Mander's (MCC_{VANGL2}= 0.81; MCC_{CDH1}= 0.82) and Pearson's (r_c= 0.34) co-localization coefficients and the large difference between them indicates that VANGL2 is at the plasma membrane of these cells, adjacent to but not overlapping, with CDH1 (Fig. 1 B-C) (Adler, 2010). We further observed VANGL2 puncta throughout the cytoplasm and also in the nucleus, which is outlined by nuclear marker LMNB1 (Fig. 1 A). To further investigate these nuclear puncta, we measured the co-localization between VANGL2 and Hoechst, finding ~45% of VANGL2 co-localizes with HOECHST and ~59% of Hoechst co-localizes with VANGL2 (r_c= 0.75; MCC_{VANGL2}= 0.52; $MCC_{HOECHST}$ = 0.66) (Fig. D-E). Next, we explored trafficking of VANGL2 to the nucleus by examining potential trafficking partners. Charged multivesicular body protein 1A (CHMP1A), is both a cytoplasmic vesicle trafficking protein that functions as part of the ESCRT-III complex (Stauffer, 2001), and a nuclear matrix protein that co-localizes with BMI1 (Howard, 2001).

CHMP1A (90%) colocalized with VANGL2 (91%) in puncta in the cytoplasm and in the nucleus (r_c= 0.53; $MCC_{VANGL2} = 0.95$; $MCC_{CHMP1A} = 0.92$) adjacent to but not overlapping (Fig. 2.1 F-H).

Because VANGL2 is not known to be localized in the nucleus, we further examined its subcellular localization by fractionating the cells into cytosolic/membrane, nuclear, and insoluble nuclear fractions and immunoblotting for VANGL2, using antibodies directed against the hyperphosphorylated form (S79/S82/S84) and the N-terminal (Fig. 2.1 I, J). The antibody targeting the N-terminal detects all four forms of VANGL2 (unphosphorylated, #; hypophosphorylated, *; phosphorylated, **; and hyperphosphorylated, ***) in the WCL. The unphosphorylated form, #, of VANGL2 was slightly present in the cytosolic/membrane fraction, and the phosphorylated, **, and hyperphosphorylated, ***, forms of VANGL2 were dominant. In the nuclear fraction the unphosphorylated, #, form is clearly present and the hypophosphorylated, *, and phosphorylated, **, VANGL2 forms were dominant, and the hyperphosphorylated, ***, form of VANGL2 was slightly expressed. There was little to no VANGL2 in the nuclear insoluble fraction. Taken together, these studies suggest that VANGL2 localizes to the nucleus in this breast cancer cell line where it at least partially localizes with CHMP1A and HOECHST (Fig. 2.1 J).

VANGL2 localizes to the nucleus in undifferentiated but not differentiated HC11 cells.

To investigate a potential functional role for VANGL2, we used HC11 cells that offer an *in vitro* model of lactogenic differentiation (Danielson, 1984). These cells undergo a multistep differentiation process by first being grown to confluency, then primed by removing EGF and finally differentiated using the lactogenic hormones dexamethasone, insulin and prolactin to induce the production of milk-filled domes (Fig. 2.2 A). We performed immunostaining for VANGL2 and BMI1 over the time course of differentiation using phalloidin and HOECHST to label F-actin and nuclei, respectively (Fig. 2.2 B-D). We collected a z-stack of images and focused on the mid-plane of the nucleus. At confluency, we observed strong nuclear VANGL2 and BMI1 staining, which for BMI1 remained strongly nuclear at priming (Fig. 2.2 C). In contrast, VANGL2 staining at priming was less nuclear and more diffuse, appearing in a punctate pattern in the cytoplasm (Fig. 2.2 C). By seven days of differentiation, there was little to no nuclear VANGL2 and it appeared, instead, primarily in puncta in the cytoplasm. BMI1 staining remained nuclear except for areas that contained milk-filled domes (Fig. 2.2 D). These data suggest that VANGL2 and BMI1 were present in the nucleus of undifferentiated cells and that differentiation resulted in a loss of nuclear VANGL2 and BMI1 (Sup. Fig. 2.2 A).

We further examined the subcellular localization of VANGL2 over the time course of HC11 cell differentiation by fractionating confluent cells (C), primed, (P) and differentiated (D) cells into cytosolic/membrane, nuclear, and insoluble nuclear fractions and immunoblotting for VANGL2 using antibodies directed against phosphorylated forms (S79/S82/S84) and the N-terminus (Fig. 2.2 E, G). With the pVANGL2 antibody, we observed pVANGL2 in all fractions at every time point; however, consistent with the immunocytochemical results, the nuclear fraction contained significantly less pVANGL2 at differentiation (Fig. 2.2 F).

Using the N-terminally directed antibody, we observed four forms of VANGL2 (unphosphorylated, #; hypophosphorylated, *; phosphorylated, **; and hyperphosphorylated, ***) in whole cell lysates (WCL), with the dominant form being phosphorylated VANGL2. In the cytosolic/membrane fraction, this phosphorylated form of VANGL2 is dominant at all three time points (Fig. 2.2 G, H). In contrast, in the nuclear fraction, the dominant forms of VANGL2 are the unphosphorylated, #, and hypophosphorylated, *, which is in the lysates from confluent and primed cells, but little to no VANGL2 dimer is observed in lysates from differentiated cells (Fig. 2.2 G, H). The insoluble nuclear fraction also contained the unphosphorylated, #, and hypophosphorylated, *, dimer in confluent and primed lysates along with the hyperphosphorylated form, ***, which appeared highest in these insoluble fractions, although again, there was little to no insoluble nuclear VANGL2 in lysates from differentiated cells (Fig. 2.2 G, H).

To examine the expression of VANGL2 in developmental time, we interrogated a recently published, single cell RNA sequencing (sc-RNAseq) dataset (Bach et al., 2017). We used diffusion maps to infer the differentiation trajectory of the luminal compartment that recapitulates the luminal differentiation process. Using sc-RNAseq data from mammary glands from 8-week virgin nulliparous (NP) and day 14.5 gestation (G). The arrows indicate the organization of the cells based on the cell state and/or alveolar or hormone sensing luminal lineage. These data support a function for VANGL2 in the cell nucleus where it may regulate the genes that drive lactation/mammary differentiation.

VANGL2 Contains a Nuclear Localization Signal that Inhibits Proliferation and Acini Formation.

Proteins that translocate to the nucleus frequently contain DNA binding sites and at least one nuclear localization signal (NLS). To search for DNA binding sites in VANGL2, we analyzed the mouse and human VANGL2 protein sequences using computational protein prediction tools (e.g. by DNAbinder, DRNApred, DP-Bind and DisoRDPbind) that query an array of databases for proteins that are reported to interact with DNA via positively charged amino acids (Fig. 2.3 A). We also used cNLS mapper and identified a putative monopartite nuclear localization signal between amino acids 349-358 (Kosugi, 2009; Kosugi, 2008). C-terminal to the NLS are two PDZ domains, an internal unconventional and a typical class I. The internal

PDZ domain contains the *Looptail* mutation (S464N) and the Class I PDZ domain contains the CD4 mutation and are both interacting sites for other PCP proteins (*Dischevelled, Scribble, Prickle, and Flamingo)* and PDZ proteins that aid its transport and signaling. (Bailly et al, 2017, Belloti et al., 2013, Kallay, et al., 2006). To further examine the localization of VANGL2 inside nuclei, we isolated nuclei from confluent HC11 cells and performed immunostaining for VANGL2, BMI1 and LMNB1, showing intact nuclei with HOECHST and LMNB1 (Fig. 2.3 B). Examining VANGL2 with LMNB1, we observe some VANGL2 puncta overlapping with LMNB1 staining within the nuclear envelope (Fig. 2.3 B, arrow). BMI1 staining with LMNB1 and with VANGL2 shows overlapping BMI1 and VANGL2 staining (Fig. 3 B, arrowhead). We analyzed the co-localization and determined that ~49% of VANGL2 pixels co-localized with HOECHST and ~47% of HOECHST pixels co-localized with VANGL2, showing that VANGL2 and DNA occupy the same space and perhaps interact (Fig. 2.3 C, D). Next, we analyzed the co-localization of VANGL2 and BMI1 pixels, finding that ~36% of VANGL2 co-localized with BMI1 and ~25% of BMI1 with VANGL2, showing that BMI1 and VANGL2 also occupy space together within the nucleus (Fig. 2.3 E, F).

To expand this analysis, we isolated nuclei from the HCC1569 cells and performed VANGL2 immunostaining using both N-terminally and C-terminally directed antibodies and co-stained with BMI1. We analyzed co-localization and found that ~42% of BMI1 co-localizes with N-terminally-labelled VANGL2, whereas only

~25% of BMI1 co-localizes the C-terminally-labelled VANGL2, indicating that BMI1 associates with N-terminal region of VANGL2 that contains the most DNA binding sites (Sup. Fig. 2.3, D-F).

To evaluate the potential functional role of the NLS, we knocked out (KO) *Vangl2* in HC11 cells using CRISPR/*Cas9* with two different sets of guides, generating two independently targeted clones. To examine the phenotype of these *Vangl2* KO clones, we performed FACS analysis that showed KO cells were larger than WT and significantly more of them contain DNA content >4N, indicating polyploidy, which is a key feature of differentiated mammary epithelial cells (Fig. 2.3 G-I, Supp. Fig. 2.3 G-H).

Next, we plated 5000 WT and KO HC11 cells in Matrigel and allowed them to grow as mammary acini for 5 days, before fixing and immunostaining them with the basal marker Keratin 14 (KRT14) and the proliferation marker Ki67; GFP marks lentivirus transduction efficiency. Wild type HC11 cells were significantly less proliferative than KO cells and the acini appear smaller with both clones yielding similar results (Fig. 2.3 K-O and Supp. Fig. 2.3 J). To determine if the *Vangl2* KO phenotype could be rescued, we overexpressed either *Vangl2* or *Vangl2DNLS* in KO cells (Fig. 2.3 J) and evaluated the phenotype of these rescued clones. *Vangl2*$_{oe}$, but not *Vangl2*$_{DNLS}$, rescued the proliferation defect and acini size of the KO HC11 clones. Taken together, these data demonstrate that nuclear localized VANGL2 inhibits proliferation of HC11 cells.

VANGL2 Inhibits Expression of Genes Regulating HC11 Cell Differentiation.

To investigate whether loss of *Vangl2* results in changes in gene expression, we performed RNA-seq analysis on Wild type and *Vangl2* KO HC11 cells. Comparing two clones to the parent HC11 cells, we see clear differential expression of genes. In clone 1, 540 down and 752 up, and in clone 2, 397 down and 823 up genes; with 135 down and 143 up overlapping genes in the two clones (Supp. Fig. 2.4 A, B). HC11 cells, however, are a heterogenous population and, accordingly, we found that the two KO clones have different transcriptomes. Both clones appear to be luminal because they express genes that are enriched in the Stat5 pathway (Fig. 4 A). We reasoned that the gene expression changes shared between the two clones in relation to the Wild type gene expression would yield insight into the consequences of *Vangl2* KO (Supp. Fig. 2.4 C, D).

We performed pathway enrichment analysis using Erichr and discovered a shared upregulation of STAT5, IRF8 and IRF1 pathways (Fig. 2.4 A) (Chen, 2013; Kuleshov, 2016; Xie, 2021). JAK/STAT5 signaling is activated downstream of Prolactin signaling and culminates in expression of milk protein genes, including beta-casein (CSN2) and whey acidic protein (WAP) both of which contain STAT5 responsive elements in their promoters (Yamaji, 2009). We further saw a very strong, shared downregulation of PRC pathway components SUZ12, EZH2 and MTF2 and RNF2 (Fig. 2.4 B). BMI1 is known to work with these other PRC proteins to regulate gene expression and stem cell maintenance (Biehs, 2017; Cho, 2013; Pietersen, 2008; Sinivasan, 2017).

To confirm our results, we performed immunocytochemistry on confluent Wild type and *Vangl2* KO confluent HC11 cells and saw downregulation of BMI1 and upregulation of differentiation markers pSTAT5A, ELF5 and CSN2 (Fig. 2.4 C-G). Taken together, our results suggest that nuclear localized VANGL2 both restricts HC11 cell proliferation and inhibits their differentiation, possibly through the regulation of BMI1.

We further explored this precocious differentiation phenotype by culturing cells in 3D Matrigel for 5 days prior to inducing differentiation with dexamethosone, insulin and prolactin for an additional 5 days. We fixed and immunostained the acini for KRT14 and milk. Again, we observe that *Vangl2* KO cells form large structures that expressed more milk than WT acini (Fig. 2.4 H-L). Overexpression of WT *Vangl2* ($V2_{oe}$) rescues this phenotype, whereas overexpression of *Vangl2DNLS* ($V2_{DNLS}$) does not, further support that nuclear VANGL2 inhibits differentiation.

Nuclear Function of VANGL2 Inhibits Differentiation of Mammary Organoids.

To further validate our discovery of a nuclear function for VANGL2 in another cellular context, we turned to primary mammary epithelial cells in organoid culture. We have previously shown that loss of *Vangl2* in the basal versus luminal compartments of the mammary gland results in different phenotypes {Smith, 2019 #1340}. Basal loss of *Vangl2* led to small acini, whereas luminal loss resulted in larger acini. To examine whether loss of *Vangl2* in either luminal or basal cells, or both luminal and basal cells, is responsible for the observed differentiation phenotype, we generated mosaic organoids in which *Vangl2* was knocked down in either the basal (KD/WT), luminal (WT/KD) compartments, in both (KD/KD) or neither (WT/WT) compartments (Fig. 2.5 A). We performed differential trypsinization to separate the luminal and basal subpopulations and then knocked down *Vangl2* in each subpopulation using lentivirus (Rubio, 2020). Next, we mixed KD and WT subpopulations, cultured in Matrigel and then differentiated the organoids. KD of *Vangl2* in both compartments resulted in very small, lumenless acini, a phenotype that was recapitulated when *Vangl2* was only knocked out in the basal compartment. In contrast, KO of *Vangl2* in only the luminal compartment resulted in acini that were significantly larger than WT (Fig. 5 B-C). Immunostaining these organoids for milk revealed more milk staining in organoids with luminal *Vangl2* KD (WT/KD) than in WT/WT organoids, suggesting that it is loss of Vangl2 from the luminal compartment that influences differentiation. This is supported by the observation that KD of Vangl2 in both the luminal and basal compartments (KD/KD) showed more milk staining than KD in the basal compartment alone.

Next, we focused on the nuclear of VANGL2 in the luminal compartment by performing a rescue experiment on mosaic organoids. As outlined above, we generated WT/WT and WT/KD organoids. In addition, we overexpressed either *Vangl2oe* or *Vangl2ΔNLS* in luminal KD cells and mixed these with WT basal cells, generating WT/$V2_{oe}$ and WT/$V2_{DNLS}$ organoids that we immunostained with for milk. Once again, we found that luminal KD of *Vangl2* resulted in larger organoids that express more milk (Fig. 2.5 E-G). Both the size and milk production were rescued back to WT/WT levels by overexpressing *Vangl2* whereas overexpressing *Vangl2ΔNLS* resulted in only partial rescue. Together, these data present a role for VANGL2 in regulating the genes that drive the differentiation of mammary gland cells.

WNT5A recruits VANGL2 to the cell membrane and out of the nucleus.

WNT5A/B are noncanonical WNTs that function in the PCP pathway. One way these WNT ligands initiate PCP signaling is by binding ROR2 receptors on the plasma membrane, leading to the phosphorylation of VANGL2 by Casein Kinase 1 (CK1E and CK1D) at multiple conserved serine/ threonine (S/T) residues located in two N-terminal clusters (Gao, 2011). WNT dosage gradients govern the extent of phosphorylation, which translates into the activity level of VANGL2 in mediating PCP. Phosphorylation of VANGL2 also regulates its intracellular trafficking with a phospho-mutant displaying decreased expression on the plasma membrane and increased localization to endosomes and lysosomes (Yang, 2017). These data suggest that phosphorylation stabilizes the surface expression of VANGL2 and regulates intracellular trafficking such that unphosphorylated VANGL2 is endocytosed and degraded.

To evaluate the effect of WNT5A on the nuclear localization of VANGL2, we treated HCC1569 cells with 100nM WNT5A for 24H, followed by biochemical fractionation and immunoblotting with an antibody that recognizes the full-length form of VANGL2. Whereas we observe robust VANGL2 in the insoluble nuclear membrane in the BSA control, VANGL2 shifts to the membrane fraction upon WNT5A treatment, suggesting that WNT5A stabilizes the membrane form VANGL2, potentially pulling VANGL2 out of the nucleus. We next used primary cells to test the effects of WNT5A on VANGL2 localization. In the BSA treated organoids, we observe accumulation of VANGL2 on the plasma membrane between cells. The Hoechst staining of the nuclei is not readily apparent in the organoids because it is obscured by VANGL2 staining. In the WNT5A treated organoids, we see nuclei clear of VANGL2 staining and an increase of VANGL2 at the membrane encircling the cells (Figure 2.6 C).

Next, we investigated whether we could observe this shift in nuclear VANGL2 in response to WNT5A *in vivo*, using slow-release ELVAX pellets that provide locally delivery of proteins to adjacent mammary gland tissue (Silberstein, 1982). The mammary glands from 12-week-old mice that had ELVAX transplants for one-week were harvested, cryopreserved, sectioned and used for immunohistochemistry analyses. In the epithelia adjacent to control BSA pellets, we observe accumulation of VANGL2 on the plasma membrane between cells. The Hoechst staining of the nuclei is not readily apparent in the epithelia because it is obscured by VANGL2 staining. This masking of nuclear Hoechst in control tissue is readily apparent in tissue adjacent to WNT5A pellets, we see nuclei clear of VANGL2 staining and an increase of VANGL2 at the membrane encircling the cells (Figure 2.6 D). To test if WNT5A influences the nuclear exit of VANGL2 we transfect HC11 cells with the translocon Sec61b that is fused with a fluorescent marker, mApple, and with a GFP tagged VANGL2. We measure the colocalization of SEC61B and VANGL2 and find a 70% decrease in their colocalization upon WNT5A exposure for 30 minutes (Figure 2.6 E).

Based on our data, where WNT5A recruits VANGL2 to the cell membrane, we hypothesized that the decrease in nuclear VANGL2 would lead to an increase in milk production. To test this hypothesis, we grew HC11 cells to confluency and primed them for lactation by adding dexamethasone, insulin and prolactin (DIP). We then treated the cells with WNT5A (100 nM, 3 days) and analyzed the expression of the milk protein, casein beta (CSN2), relative to control BSA samples. The western blot analysis for CSN2 show a 2-fold increase in WNT5A treated samples compared to BSA controls. These data show that the change in nuclear localization of VANGL2 influence milk production, and that WNT5A is able to mediate this function.

DISCUSSION

Investigations surrounding the function of VANGL2 in the mammary gland are recent (Smith, 2019). These studies focused on the embryo and puberty developmental stages and showed ectopic acini due to a loss-of-function *Vangl2* mutation (*Looptail)*. Although we gained some knowledge about the role VANGL2 plays in mammary gland development, we still did not understand how VANGL2 was communicating with a nuclear protein, BMI1. To investigate the molecular mechanisms that VANGL2 was governing in later developmental stages (e.g., lactation), I sought a cell model system that would address these outstanding questions, HC11 cells. The benefit of HC11 cells is that they mimic lactation onset well in a dish and allow for the introduction of mutations that would be otherwise difficult to investigate in vivo like that of Vangl2. These investigations also expand our knowledge about how PCP signaling may function in lactation.

The PCP pathway is mostly known for orienting cells along the proximal-distal tissue plane, and novel roles beyond polarity cues have emerged recently. The VANGL2 receptor can be cued for PCP signaling at the plasma membrane by the non-canonical WNT ligands WNT5A/B, WNT11 and WNT7A (Gao 2011; Le Grande, 2009; Messéant, 2017). Though the role that these ligands play in lactation is not well understood, and only few reports have queried the expression of WNT5A and WNT5B in the different mammary gland cell populations (Roarty, 2015).

Interestingly, WNT5A expression was the highest in mature luminal and alveolar progenitor cells. Using our HC11 cell line model we were able to analyze if WNT5A increases milk production, and by western blot we see an increase of the milk protein CSN2. Beyond, the cell membrane not much is known about VANGL2 and what its function is in endosomes.

My studies establish a novel role for VANGL2 inside the cell nucleus, beyond the plasma membrane. Using breast cancer cells, we show the subcellular expression of VANGL2: at the cell membrane, cytosol, vesicles, paranuclear cloud, at the nuclear periphery, inside of the nuclei, and around chromatin. We discover a striking expression pattern for VANGL2 in differentiated cells. Where VANGL2 localizes to the nucleus in undifferentiated but not differentiated HC11 cells. A nuclear localization signal (NLS) is used to transport proteins from the cytosol and to the cell nucleus. We find that the mouse and human VANGL2 sequence contain an NLS at the C-terminal. To test if the NLS of VANGL2 plays a functional role in cell differentiation we overexpress a mutant NLS construct in a knock-out *Vangl2* background. My data show that VANGL2 NLS inhibits the proliferation and formation of acini. To understand the genes that regulate this phenotype we sequenced the transcriptomes of *Vangl2* knock-out and compared them to Wild-type cells. We find two key pathways to be influenced by the loss of Vangl2, the STAT5 pathway and PRC pathway.

To explore the role of VANGL2 inside the nucleus we used several different methods to analyze its nuclear expression and function. Via western blotting and immunofluorescent microscopy, we established that VANGL2 is expressed in the nucleus of mammary gland cells. Using CUT&RUN we were able to address if VANGL2 binds DNA. Our preliminary data show that VANGL2 vacates the nucleus of differentiated mammary gland cells. Zooming into the Stat5a gene we see that VANGL2 is binding the promoter region of cells when they are undifferentiated. Strikingly, when we analyze the Stat5a promoter of the differentiated cells we see that VANGL2 occupancy is absent or decreased, thus allowing for the activation of the STAT5 pathway. Together with our biochemical and functional analyses of VANGL2, RNA-sequencing of Vangl2-KO cells, and CUT&RUN analyses we have identified a potential role for VANGL2 in the nucleus of mammary gland cells. We present a novel mechanism for VANGL2 inside of the cell nucleus, where it seems to be acting as a transcriptional inhibitor of differentiation genes. We are the first group to report a nuclear function for a PCP protein and our data opens the possibility to other proteins adopting a similar mode of action.

METHODS

Plasmids

The lentivirus plasmids used to transduce cells have the different forms of *Vangl2* cloned into NheI/NotI digested pCDH-CMV-MCS-EF1-Puro. At the N-terminal of *Vangl2* there is a fused 3XFLAG-GFP. The Vangl2DNLS construct contains a span of mutations in the Nuclear Localization Signal (NLS) motif of VANGL2, amino acids 349-358 ERRVRKRRAR → EEEVEEEEAE. The plasmids were made by Epoch Life Science, Inc. (Sugarland, TX).

CRISPR/Cas9

Two sgRNA's were designed for mouse *Vangl2* using Synthego and validated using the UCSC genome browser. *Vangl2* was knocked out by Nucloefecting (Lonza program #DS-138) HC11 cells with individual sgRNA's and 100nM of homology directed repair (HDR) template containing a stop codon and restriction digest site not found within *Vangl2* (HindIII: AAGCTT) to use as a genotype selection for successful HDR. The HDR template was designed by spanning 50±bp from the PAM cut site, at which a stop codon 5'-TAACTAACTAA-3' and a species-specific unique restriction digest site were added. The cells were grown in 24-well dishes until confluency before isolating into single cells that were grown into single colonies in a 96-well dish and mutants were validated by Western Blotting. Two successful clones were used for experiments presented here.

Immunocytochemistry

Cells were seeded in an 8-well chamber slide coated with Poly-Lysine for 30 minutes at room temperature followed by 2X DPBS washes and grown overnight at 37 ˚C/ 5 % CO2. Cells were fixed using 4 % paraformaldehyde for 10 minutes on ice, permeabilized for 10 minutes on ice using PBS-T (Phosphate Buffered Saline + 0.25% Triton-X 100), blocked using 1 % donkey serum in 300 nM glycine dissolved in PBS for 1 hour, and incubated over night at 4 ˚C on a rocking surface with respective primary antibodies in PBS + 1 % NDS. Secondary antibodies were incubated the following day for 1 hour at room temperature on a rocking surface blocked from light and washed 3X using PBS/1 % NDS and lastly with HOECHST in PBS (DNA Dye for nucleus) for 5 minutes at room temperature each. Cells were mounted in Fluoromount G and dried over night before sealing with clear nail polish.

3D cell cultures

HC11 cells were grown in 3D as previously described (Rubio et al., 2021, Liu et al., 2015). Briefly, 5,000 HC11 cells were embedded in 10% Matrigel atop a denser base layer of 50% Matrigel (on-top method). Cells were grown in 3D for 10 days before fixation. The cell media was changed on the cells every 2 days, and the cells were fixed for immunofluorescent analysis by fixing the whole cultures in each well of an 8-well chamber slide.

Mosaic Organoids

Organoids from primary cells were generated as previously described (Rubio et al., 2020). The differential trypsinized cells were independently transduced with lentivirus constructs at 30 MOI for 72 hours prior to their embedding in Matrigel.

Western blotting

Subcellular fractionation was done as reported previously (Baghirova *et al.*, 2015), with minor modifications: Hexaylene Glycol was substituted for 10% Glycerol in the buffers and 3 washes were performed in between each fraction. Protein expression was determined by running the lysates dissolved in equal volume of 2X Laemli Buffer on an SDS-Page gel for 1.5 hours at 100 V. The proteins were transferred to a PVDF membrane for 1.5 H at 400 mA and blocked using 5 % BSA rocking at room temperature for 1 hour. Primary antibody (in 5 % BSA) incubation was done overnight on a rocking platform at 4 ˚C. Membranes were washed 3X using TBST-High Salt for 5 minutes on a rocking surface at room temperature before being incubated with a secondary antibody, that is specific to the species of the primary antibody and tagged with Horseradish Peroxidase (HRP), for 45 minutes in 5% Non-fat dry milk rocking at room temperature. The membranes were washed 3X using TBST-High Salt and 1X using TBST-Low Salt for 5 minutes rocking at room temperature. Protein expression was determined relative to a house keeping protein specific to each cell compartment probed.

Single nuclei microscopy

Nuclei were isolated from HC11 and HCC1569 cells using the EZ Nuclei Kit. Nuclei from these cells in PBS is added to positively charged slides and fixed by adding 100% MeOH (totaling 50% MeOH fix) for 2 minutes at room temperature. A second fixation step is performed using 100% MeOH for 2 minutes. The nuclei are blocked using 1% Donkey Serum in PBS + 0.3M glycine for 1 hour and primary antibodies specific to each protein is added in 1% Donkey Serum in PBS overnight at 4ºC in a humid chamber. The next day, the nuclei are washed 2X using 0.1% PBST (Triton X-100) for 5 minutes each wash. Secondary antibody specific to each target was added to the nuclei for 1 hour at room temperature in a humid chamber. The nuclei are washed 2X using 0.1% PBS (Triton X-100) for 5 minutes each wash, and a third wash using Hoechst 33342 in PBS for 5 minutes. The nuclei were mounted in Fluoromount G and dried over night before sealing with clear nail polish.

Microscopy and Co-Localization Analyses

Samples were images using a Solamere Confocal Microscope. Data analyses was performed using Imaris. Nuclear colocalization was determined by masking the Region of Interest (ROI) to HOECHST and thresholding within that ROI for each respective channel. The average Pearson's Coefficient are reported for the ROI colocalization (r_c). The average Mander's Coefficient is reported for each colocalization analyses.

Area and integrated density measurements

3D z-stacks were captured using a Spinning Disk Confocal Microscope. The z-stacks were reconstructed in FIJI set to the max intensity. Using the Cy5 channel, specific to milk, the area and Integrated Density of the 3D HC11 colonies was measured. Shortly, the threshold of the Cy5 channel was set using the Default setting, the image was converted to binary, and the colonies with an area greater than 500 μm^2 were accounted for.

RNA-sequencing

poly-A selected transcripts from Wild type and Vangl2-KO HC11 cells were processed for RNA-sequencing libraries using the NEBNext kit. 50 PE Nova-Seq platform was used to read the fragments. Differential expression analysis was performed using DEseq2. The enriched pathways were determined using ENRICHR.

Statistics

The mean ± SEM is reported. P-values are determined using unpaired *t*-test with a Welch's correction, unless specified. Significance is denoted as non-significant ($P \geq 0.05$), ns, significant ($0.05 < P < 0.01$), *, very significant ($0.01 < P < 0.001$), **, and extremely significant ($P < 0.001$), ***, ****.

FIGURES

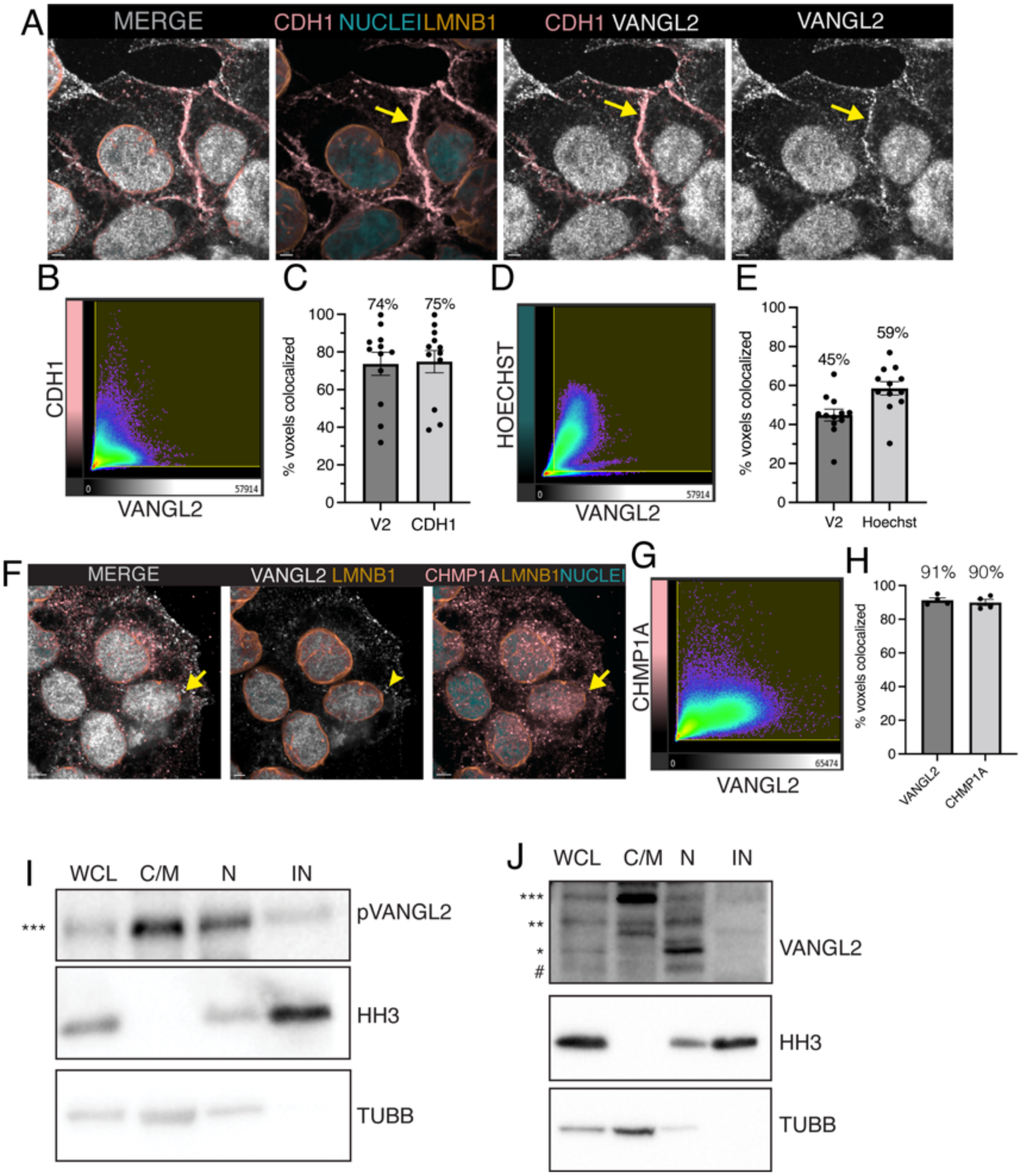

Figure 2.1 VANGL2 localizes to the nucleus in HCC1569 cells.

A) Representative micrographs of HCC1569 cells immunostained for VANGL2 (white), cell membrane protein CDH1 (pink), nuclear lamina protein LMNB1 (gold) and DNA dye Hoechst 33342 (blue). The yellow arrow points to the cell membrane co-occupancy of VANGL2 and CDH1. Scale = 3 µm. N=12.

B) Co-localization scatterplot for VANGL2 (*x*-axis) and CDH1 (*y*-axis). The yellow square gates the region of interest (ROI).

C) Plot of the quantification for the percent of VANGL2 and CDH1 voxels that are co-localized in HCC15690 cells (Mander's colocalization coefficient (MCC), MCC_{V2}= 0.81±0.06), and MCC_{CDH1}= 0.82±0.05), Pearson's colocalization coefficient (r_c) of 0.34±0.03. The mean voxels are plotted the whiskers represent ± SEM. N=12.

D) Co-localization scatterplot for VANGL2 (*x*-axis) and HOECHST (*y*-axis). The yellow square gates the ROI.

E) Plot of the quantification for the percent of voxels that are colocalized in the nuclei of HC11 cells (Mander's colocalization coefficient (MCC), MCC_{V2} = 0.52±0.04, and $MCC_{HOECHST}$ = 0.66±0.04, Pearson's colocalization coefficient (r_c) of 0.75±0.03. The mean voxels ± SEM. N=12.

F) Representative micrographs of HCC1569 cells immunostained for VANGL2 (white), cell membrane protein CHMP1A (pink), nuclear lamina protein LMNB1 (gold) and DNA dye Hoechst (blue). Scale = 4 µm.

G) Co-localization scatterplot for VANGL2 (*x*-axis) and CHMP1A (*y*-axis). The yellow square gates the ROI.

H) Plot of the quantification for the percent of VANGL2 and CHMP1A voxels that are colocalized in HCC1569 cells (Mander's colocalization coefficient (MCC), MCC_{V2}= 0.95±0.02, and MCC_{CHMP1A}= 0.92±0.02, Pearson's colocalization coefficient (r_c) of 0.53±0.03. The means are plotted ± SEM. N=4.

J) Representative Western blot of hyperphosphorylated VANGL2 (***) using HCC1569 whole cell lysates (WCL) and subcellular fractionated lysates: cytosolic/membrane (C/M), soluble nuclear (N), and insoluble nuclear (IN) with fractions assessed using specific antibodies: ß-tubulin I (TUBB) for cytoplasmic/membrane fraction and histone H3 (HH3) for nuclear fraction. N=*3*.

J) Representative Western blot of all forms of VANGL2 using HCC1569 lysates fractionated: cytosolic/membrane (C/M), soluble nuclear (N), and insoluble nuclear (IN) with fractions assessed using specific antibodies: ß-tubulin I (TUBB) for cytoplasmic/membrane fraction and histone H3 (HH3) for nuclear fraction. Four forms of VANGL2 are observed: unphosphorylated, #; hypophosphorylated, *; phosphorylated, **; and hyperphosphorylated, ***. N=*3*.

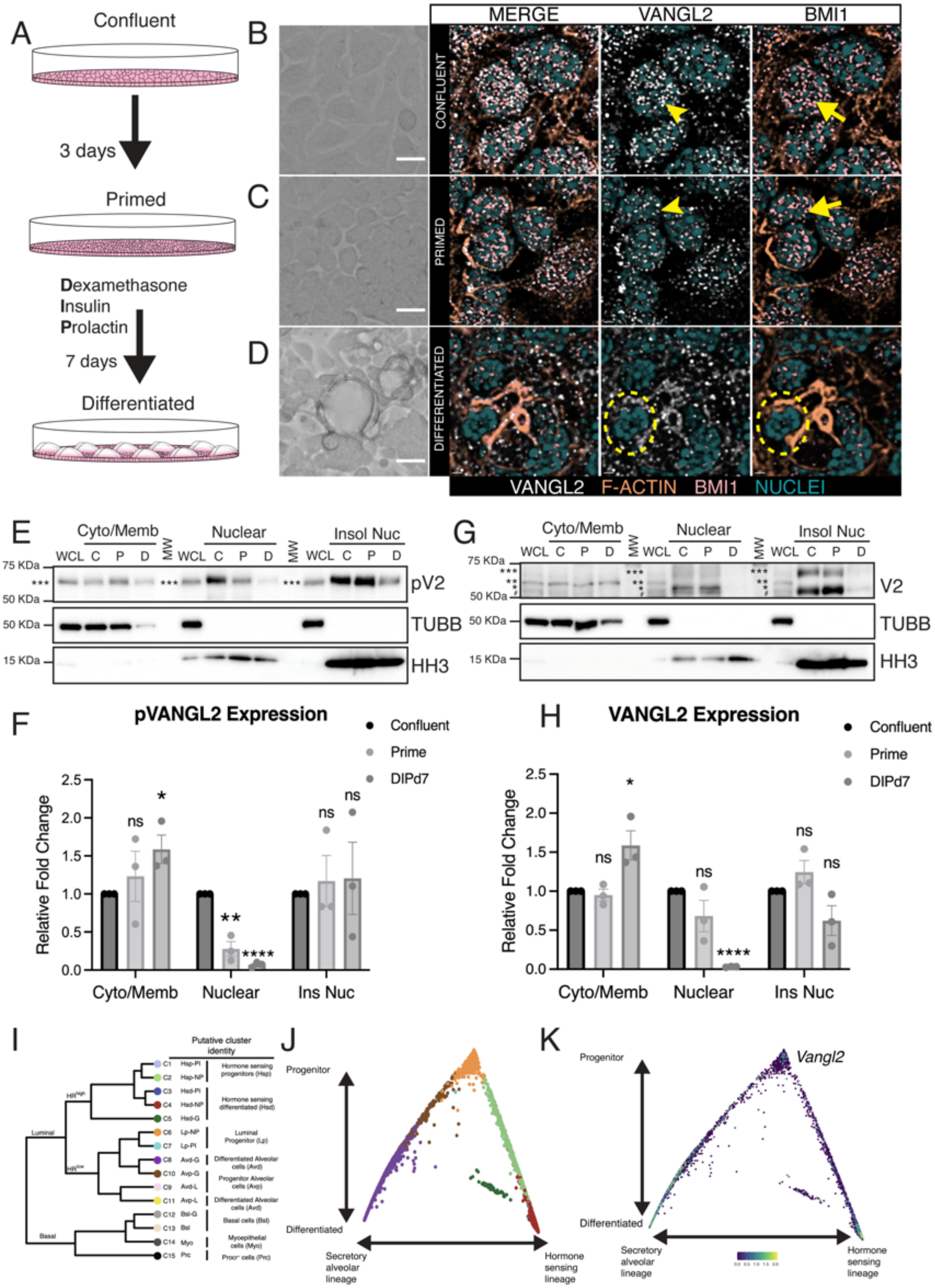

Figure 2.2 VANGL2 localizes to the nucleus in undifferentiated but not differentiated HC11 cells.

A) Cartoon illustration of the HC11 cell differentiation process, cells are grown to confluence, cultured for 3 days and then primed for 24 hours in the absence of EGF. Finally, they are differentiated in the presence of dexamethasone, insulin and prolactin.

B-D) Representative micrographs of HC11 cells at different stages of differentiation: confluent (B), primed (C) and differentiated (D) by bright field (BF) (left, scale 20 µm) and immunofluorescence (right) stained for VANGL2 (white), F-actin (gold), BMI1 (pink), and DNA dye HOECHST (blue). Scale = 1 µm. Lower magnification images are available in Supplementary Figure 2.2.

E) Representative Western blot of phospho-VANGL2 (S79/S82/S84) at different stages of differentiation: confluent (C), primed (P) and differentiated (D). HC11 lysates were fractionated: cytosolic/membrane, soluble nuclear, and insoluble nuclear with fractions assessed using specific antibodies: ß-tubulin I (TUBB) for cytoplasmic/membrane fraction and histone H3 (HH3) for nuclear fraction.

F) Quantification of phospho-VANGL2 relative to its loading control**s,** which are TUBB for cytoplasmic/membrane fraction and histone H3 (HH3) for nuclear fraction. VANGL2 levels at the different stages of differentiation are normalized relative to the confluent stage. N=3 independent experiments, data are represented as mean ± SEM. P-values are determined using unpaired *t*-test with a Welch's correction. Significance is denoted as non-significant ($P \geq 0.05$), ns, significant ($0.05<P<0.01$), *, very significant ($0.01<P<0.001$), **, and extremely significant ($P<0.001$), ***.

G) Representative Western blot of VANGL2 at different stages of differentiation: confluent (C), primed (P) and differentiated (D). HC11 lysates were fractionated: cytosolic/membrane, soluble nuclear, and insoluble nuclear with fractions assessed using specific antibodies: ß-tubulin I (TUBB) for cytoplasmic/membrane fraction and histone H3 (HH3) for nuclear fraction. Four forms of VANGL2 are observed: unphosphorylated, #; hypophosphorylated, *; phosphorylated, **; and hyperphosphorylated, ***.

H) Quantification of all forms of VANGL2 relative to their loading controls, which are TUBB for cytoplasmic/membrane fraction and histone H3 (HH3) for nuclear fraction. VANGL2 levels at the different stages of differentiation are normalized relative to the confluent stage. N=3 independent experiments, data are represented as mean ± SEM. P-values are determined using unpaired *t*-test with a Welch's correction. Significance is denoted as non-significant ($P \geq 0.05$), ns, significant ($0.05<P<0.01$), *, very significant ($0.01<P<0.001$), **, and extremely significant ($P<0.001$), ***.

I) Dendrogram of clusters based on sc-RNAseq data from a previous study (Bach et al., 2017).

J) Differentiation trajectory of the luminal compartment that recapitulates the luminal differentiation process. Using sc-RNAseq data from mammary glands from 8-week virgin nulliparous (NP) and day 14.5 gestation (G). The arrows indicate the organization of the cells based on the cell state and/or alveolar or hormone sensing luminal lineage. sc-RNAseq are from (Bach et al., 2017).

K) Differentiation trajectory of the luminal compartment colored by the normalized and scaled expression values of *Vangl2.*

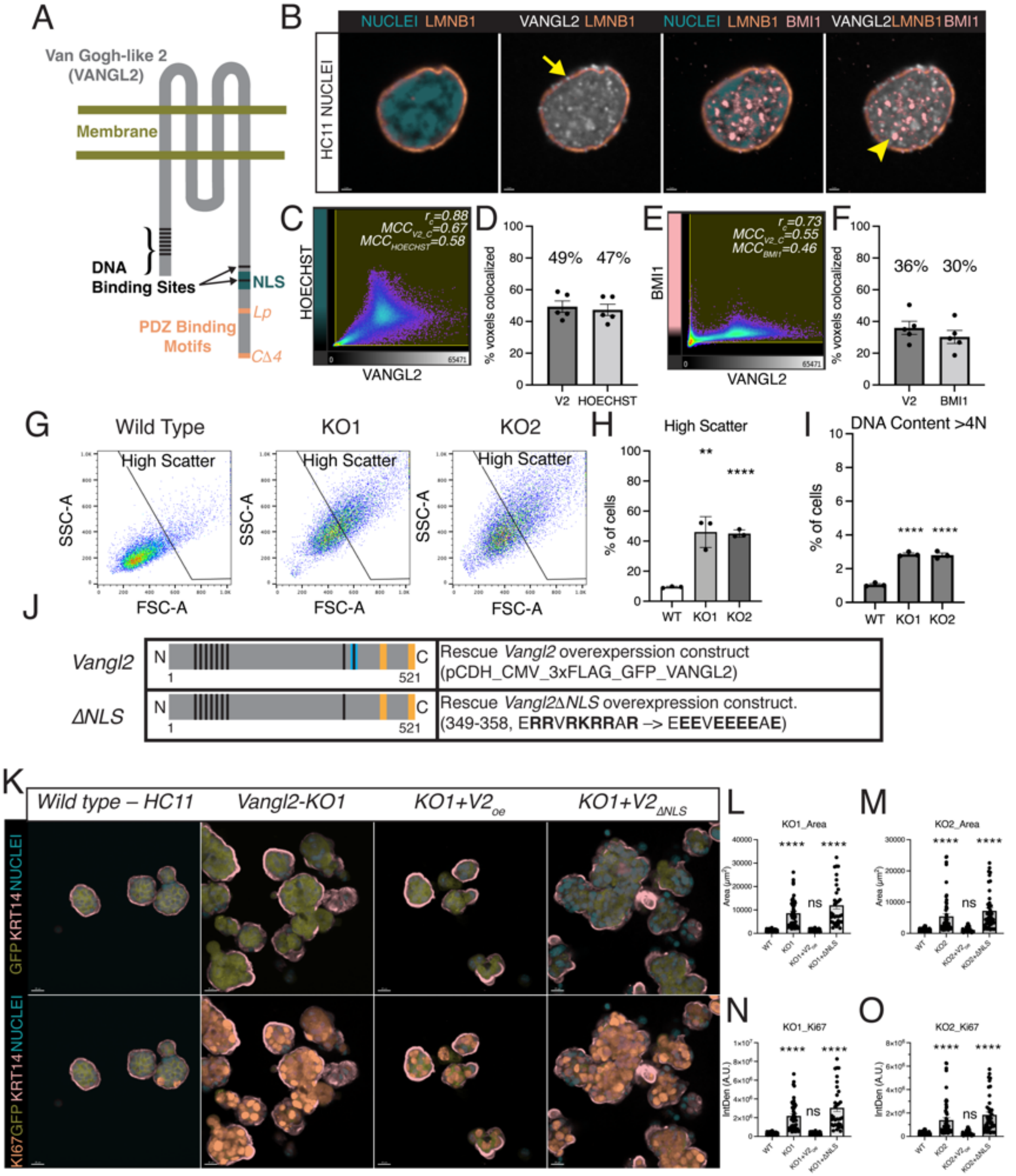

Figure 2.3 VANGL2 Contains a Nuclear Localization Signal that Inhibits Proliferation and Acini Formation

A) Cartoon illustration of the tetra-transmembrane VANGL2 protein. The novel DNA binding sites (black) are found at the N-terminus and C-terminus. Additionally, a Nuclear Localization Signal (blue) is found at the C-terminus. Two previously identified PDZ binding motifs (orange) are also at the C-terminus.

B) Nuclei isolated from HC11 cells are immunolabeled with nuclear Lamin B1 (LMNB1, gold), BMI1 (pink), VANGL2 (white), and DNA dye Hoechst 33342 (Nuclei, blue). Scale=1 μm.

C) Co-localization scatterplot for VANGL2 (*x*-axis) and HOECHST (*y*-axis). ROI in yellow box.

D) Plot of the quantification for the percent of VANGL2 and HOECHST voxels that are colocalized in the nuclei of HC11 cells (Mander's colocalization coefficient (MCC), $MCC_{V2} = 0.67 \pm 0.03$, and $MCC_{HOECHST} = 0.58 \pm 0.03$, Pearson's colocalization coefficient (r_c) of 0.88 ± 0.01. Mean ± SEM. N=5.

E) Co-localization scatterplot for VANGL2 (*x*-axis) and BMI1 (*y*-axis). ROI in yellow box.

F) Plot of the quantification for the percent of VANGL2 and BMI1 voxels that are colocalized in the nuclei of HC11 cells (Mander's colocalization coefficient (MCC), $MCC_{V2}= 0.55 \pm 0.02$, and $MCC_{BMI1}= 0.46 \pm 0.06$, Pearson's colocalization coefficient (r_c) of 0.73 ± 0.01. Mean ± SEM. N=5.

G) Fluorescent activated cell sorting (FACS) scatter plots SSC-A (*y*-axis) and FSC-A (*x*-axis) of cells stained with DNA dye, propidium iodide (PI). A high scatter gate binds the cells that are more complex (SSC-A) and larger (FSC-A). Images of cells in Supplementary Figure 2.3 I.

H) The percent of cells that are withing this gate is quantified in the plot. P-values are determined using unpaired *t*-test with a Welch's correction. Significance is denoted as non-significant ($P \geq 0.05$), ns, significant ($0.05<P<0.01$), *, very significant ($0.01<P<0.001$), **, and extremely significant ($P<0.001$), ***, ****.

I) The DNA content of these cells was also measured. The plot for the percent of cells that contain DNA content greater than 4 (>4N) is represented here, and measurements for <4N are in supplementary figure 2.3 G-H.

J) Cartoon illustration of the VANGL2 lentivirus Wild type *Vangl2* (*$V2_{oe}$*) and mutant *Vangl2DNLS* ($V2_{DNLS}$) constructs. The constructs contain two tags fused to the N-terminus, a 3xFLAG and GFP tag. The mutant DNLS construct contains mutations along the 349-358 amino acids of VANGL2.

K) HC11 cells grown in 3D and immunolabeled for the basal cell marker Keratin 14 (KRT14, pink), proliferation marker Ki67 (gold), and DNA dye (HOECHST, blue), row 1. To exhibit their change in proliferation the cultures are shown in the second row with Ki67. Each column represents an independent condition, Wildtype (column

1), *Vangl2*-KO (column 2), *Vangl2*-KO + *Vangl2* overexpression construct (column 3), and *Vangl2*-KO + DNLS mutant construct (column 4). Scale=20 µm.

L-M) Quantification of the size of the different 3D HC11 cell cultures. Where the KO and KO+$\mathrm{V2}_{DNLS}$ are significantly larger and the $V2_{oe}$ construct rescues the size to similar Wild type area.

M-O) Measure of proliferation using Ki67 integrated density (IntDen). Where the KO and KO+$\mathrm{V2}_{DNLS}$ are significantly more proliferative and the $V2_{oe}$ construct rescues similar to Wild type Ki67 IntDen levels. P-values are determined using unpaired *t*-test with a Welch's correction. Significance is denoted as non-significant ($P \geq 0.05$), ns, significant ($0.05 < P < 0.01$), *, very significant ($0.01 < P < 0.001$), **, and extremely significant ($P < 0.001$), ***, ****.

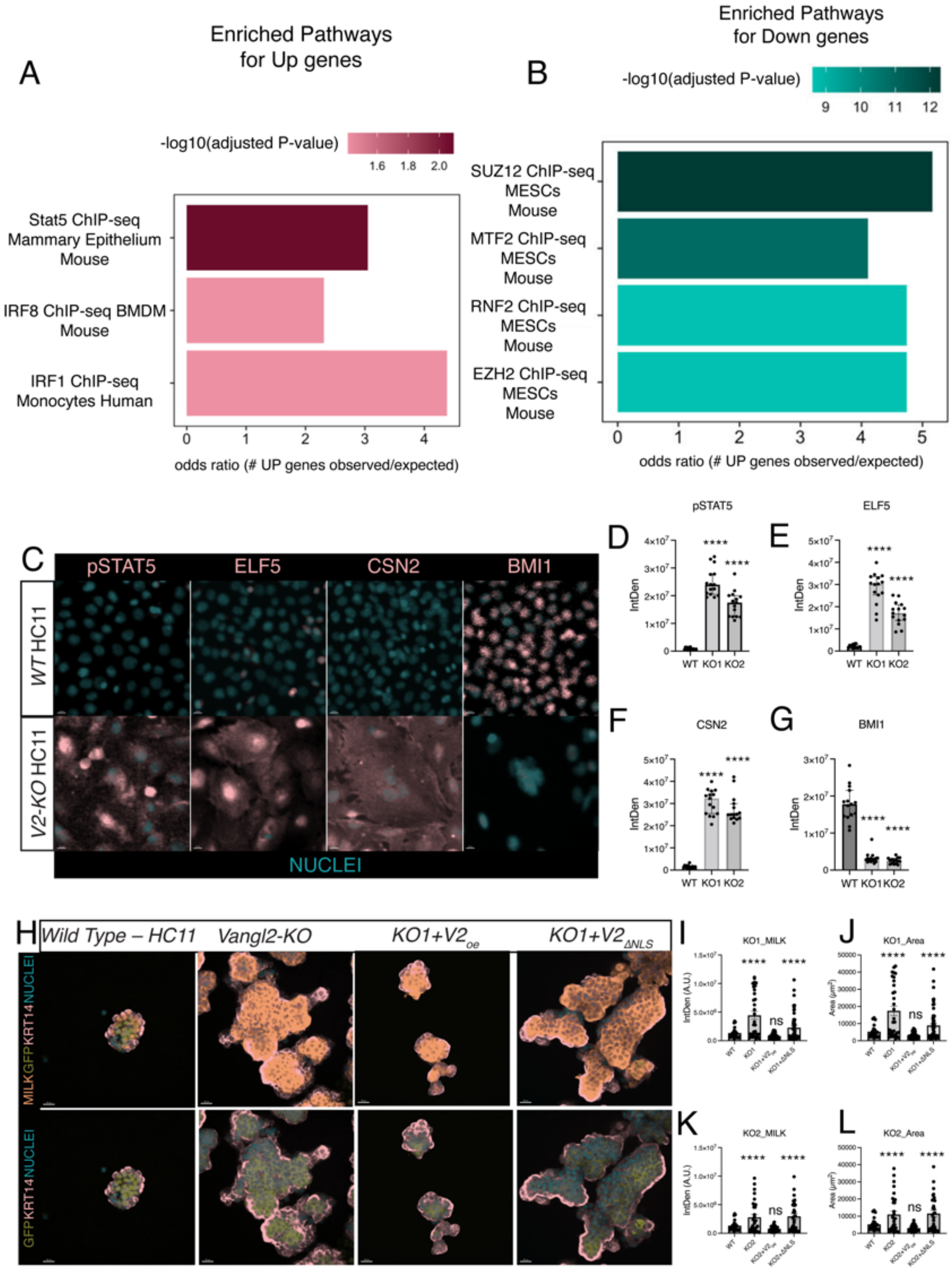

Figure 2.4 VANGL2 Inhibits Expression of Genes Regulating HC11 Cell Differentiation

A) The enriched pathways from the genes upregulated in *Vangl2*-KO HC11 cells. The colored scale is set to a log scale, and the darker pink color represents higher P-value.

B) The enriched pathways from the genes downregulated in *Vangl2*-KO HC11 cells. Using the same scaling as before, the darker blue tone represents a higher P-value.

C) Immunocytochemistry analysis of Wild type and *Vangl2*-KO HC11 cells to confirm RNA-seq results. The cells are immunolabeled with the DNA dye Hoechst 33342 (Blue) and pSTAT5, ELF5, CSN2 and BMI1 (pink). Scale = 10 µm. N=15.

D-G) Integrated Density measurements of HC11 Wild type and *Vangl2* KO clone 1 (KO1) and *Vangl2* KO clone 2 (KO2) of the four markers used in the immunocytochemistry. The data show a significant increase of pSTAT5, ELF5, CSN2 and a decrease in BMI. P-values are determined using unpaired *t*-test with a Welch's correction. Significance is denoted as non-significant ($P \geq 0.05$), ns, significant ($0.05 < P < 0.01$), *, very significant ($0.01 < P < 0.001$), **, and extremely significant ($P < 0.001$), ***, ****.

H) HC11 cell acini immunolabeled for MILK (gold), Cytokeratin 14 (KRT14, pink), and Nuclei (Hoechst DNA dye, blue). Wild type and *Vangl2*-KO cells are transduced with control lentivirus shScr (column 1 and 2), *Vangl2*-KO cells are also transduced with *Vangl2* and *Vangl2DNLS* overexpressing lentivirus ($V2_{oe}$ and $V2_{DNLS}$). Scale = 20 µm.

I-J) Quantification of the size of the different 3D HC11 cell acini. Where the KO and KO+$V2_{DNLS}$ are significantly larger and the $V2_{oe}$ construct rescues the size to similar Wild type area. Clone 1 I) and clone 2 J).

K-L) Measure of Milk integrated density (IntDen). Where the KO and KO+$V2_{DNLS}$ produce significantly more milk and the $V2_{oe}$ construct rescues similar to Wild type milk IntDen levels. P-values are determined using unpaired *t*-test with a Welch's correction. Significance is denoted as non-significant ($P \geq 0.05$), ns, significant ($0.05 < P < 0.01$), *, very significant ($0.01 < P < 0.001$), **, and extremely significant ($P < 0.001$), ***, ****. Clone 1 K) and clone 2 L).

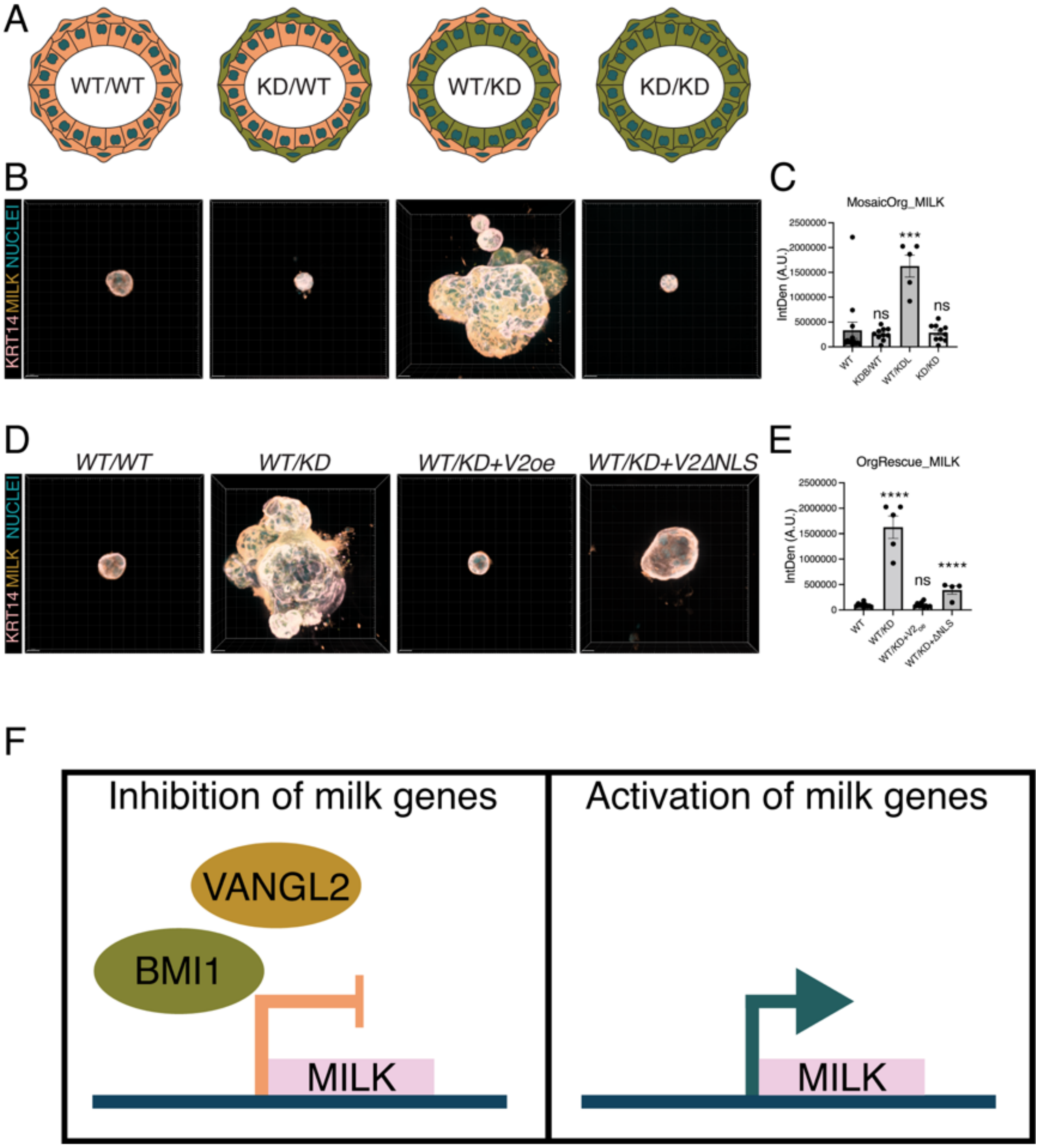

Figure 2.5 Nuclear Function of VANGL2 Inhibits Differentiation of Mammary Organoids

A) Cartoon illustration of mosaic organoids, where the two mammary gland cell compartments have different genotypes. In the first condition the basal and luminal cells are both the same genotype, Wild type (scramble control) (WT/WT). In the second condition *Vangl2* is knocked-down (KD) in the outer basal cells (green), and the inner luminal cells (orange) are of wildtype genotype (KD/WT). In the third condition, the outer basal cells (orange) are of wildtype genotype and *Vangl2* is KD in the inner luminal cells (green) (WT/KD). In the fourth condition, *Vangl2* is KD in both cell compartments (KD/KD).

B) Representative immunofluorescent images of the mosaic organoids, which are immunolabeled with the outer basal cell marker Cytokeratin 14 (KRT14), MILK (gold), and Nuclei (HOECHST, DNA Dye). Scale = 10 μm.

C) The integrated density (IntDen) of Milk is measured for each mosaic organoid conditions. When compared to WT/WT the WT/KD colonies contain a significant amount of milk, and the KD/WT and KD/KD contain similar amount of milk. . P-values are determined using unpaired *t*-test with a Welch's correction. Significance is denoted as non-significant ($P \geq 0.05$), ns, significant ($0.05 < P < 0.01$), *, very significant ($0.01 < P < 0.001$), **, and extremely significant ($P < 0.001$), ***, ****. Mean ± SEM.

D) Organoids where the outer basal cells (orange) are of wildtype genotype and *Vangl2* is KD in the inner luminal cells (green) (WT/KD) are infected with lentiviral constructs that overexpress *Vangl2* ($V2_{oe}$) or the mutant *Vangl2* NLS construct ($V2_{DNLS}$).

E) The integrated density (IntDen) of milk is quantified for the conditions in the rescue experiment. When compared to WT/WT the WT/KD ± $V2_{DNLS}$ colonies contain more milk and the WT/KD ± $V2_{oe}$ contain a similar amount of milk. . P-values are determined using unpaired *t*-test with a Welch's correction. Significance is denoted as non-significant ($P \geq 0.05$), ns, significant ($0.05 < P < 0.01$), *, very significant ($0.01 < P < 0.001$), **, and extremely significant ($P < 0.001$), ***, ****. Mean ± SEM.

F) Cartoon of a model molecular mechanism for how VANGL2 and BMI1 are working together in mammary gland cells. In non-differentiated cells VANGL2 and BMI1 localize to the nucleus to inhibit milk genes (differentiation genes). And in differentiated cells VANGL2 and BMI1 vacate genes and allow for a differentiation gene program to launch and thus milk production to occur.

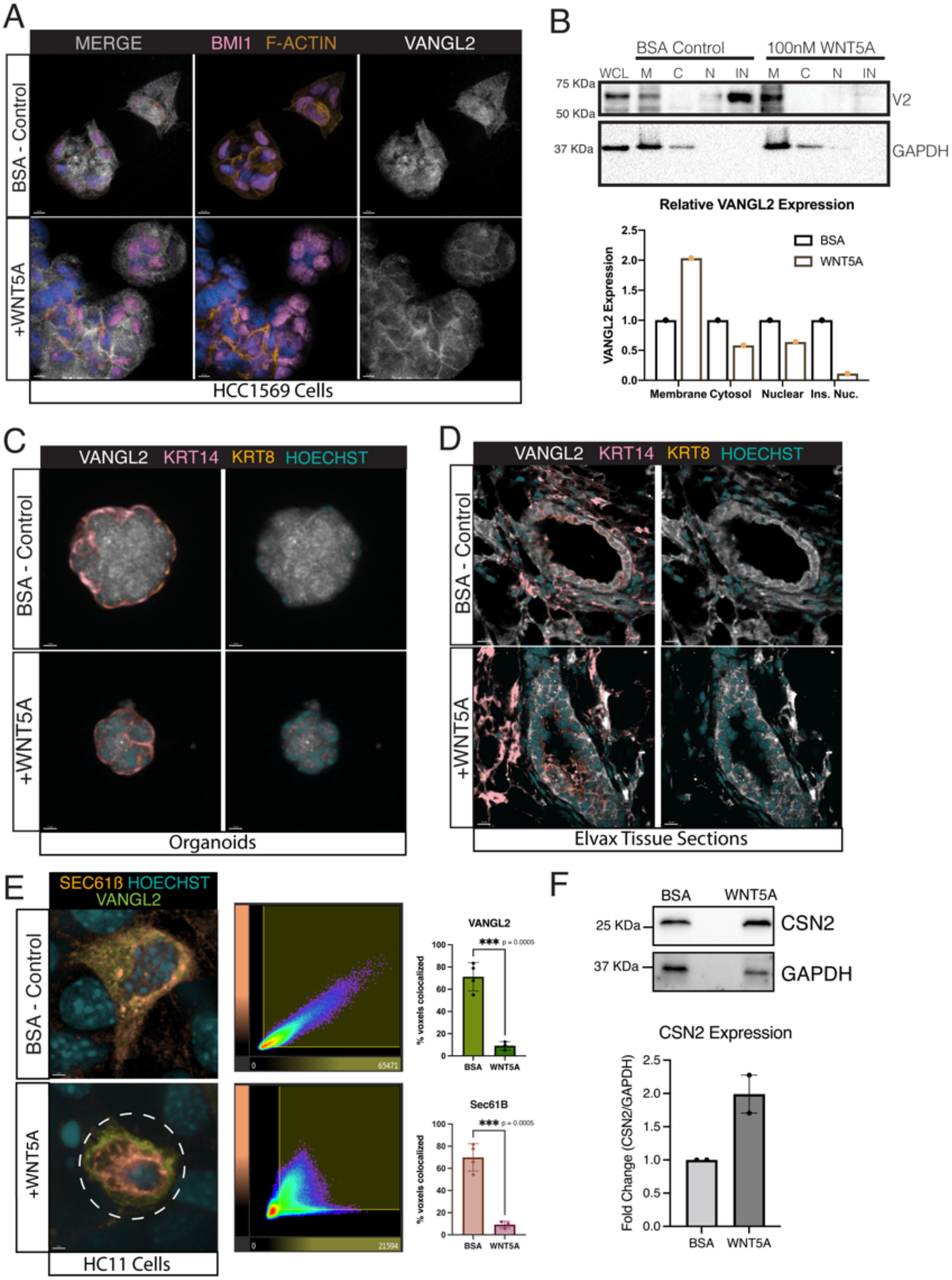

Figure 2.6 WNT5A recruits VANGL2 to the cell membrane and out of the nucleus.

A) Micrographs of immunocytochemistry analysis using HCC1569 cells, the top row shows the control cells (BSA) and the bottom row shows the WNT5A treated samples (100nM for 24 hours). The cells are immunolabeled with VANGL2 (white), BMI1 (pink), and F-ACTIN (gold). = 10 µm.

B) Representative Western blot of lysates from fractionated HCC1569 cells: cytosolic/membrane (C/M), soluble nuclear (N), and insoluble nuclear (IN) with fractions assessed using specific antibodies: ß-tubulin I (TUBB) for cytoplasmic/membrane fraction and histone H3 (HH3) for nuclear fraction. The changes in expression for each compartment are quantified in the bar graph.

C) Representative immunofluorescent images of organoids, which are immunolabeled with the outer basal cell marker Cytokeratin 14 (KRT14) (pink), inner luminal cell marker Cytokeratin 18 (CK18) (gold), VANGL2 (white), and Nuclei (HOECHST, DNA Dye). Scale = 5 µm.

D) Tissue cross sections from mammary glands that were transplanted with slow releasing ELVAX beads that release BSA or WNT5A over one week before harvested, cryo-preserved/sectioned, and processed. The tissue sections are immunolabeled with the outer basal cell marker Cytokeratin 14 (KRT14) (pink), inner luminal cell marker Cytokeratin 18 (CK18) (gold), VANGL2 (white), and Nuclei (HOECHST, DNA Dye). Scale = 10 µm.

E) Micrographs of HC11 cells labeled with VANGL2 (green), SEC61B (gold), and Hoechst (blue). The top row shows the control cells (BSA) and the bottom row shows the WNT5A treated samples (100nM for 24 hours). Co-localization scatterplot for BSA samples VANGL2 (*y*-axis) and SEC61B (*x*-axis). ROI in yellow box. Plot of the quantification for the percent of VANGL2 and SEC61B voxels that are colocalized in HC11 cells. Pearson's colocalization coefficient (r_c) for BSA= 0.88 ± 0.01 and WNT5A =0.65 ± 0.01. Mean ± SEM. N=5. Scale = 2 µm.

F) Representative Western blot of lysates from HC11 assessed using milk specific antibodies, CSN2, and loading control GAPDH. The changes in expression for each compartment are quantified in the bar graph, where CSN2 levels are normalized to GAPDH. N=2. Mean ± SEM.

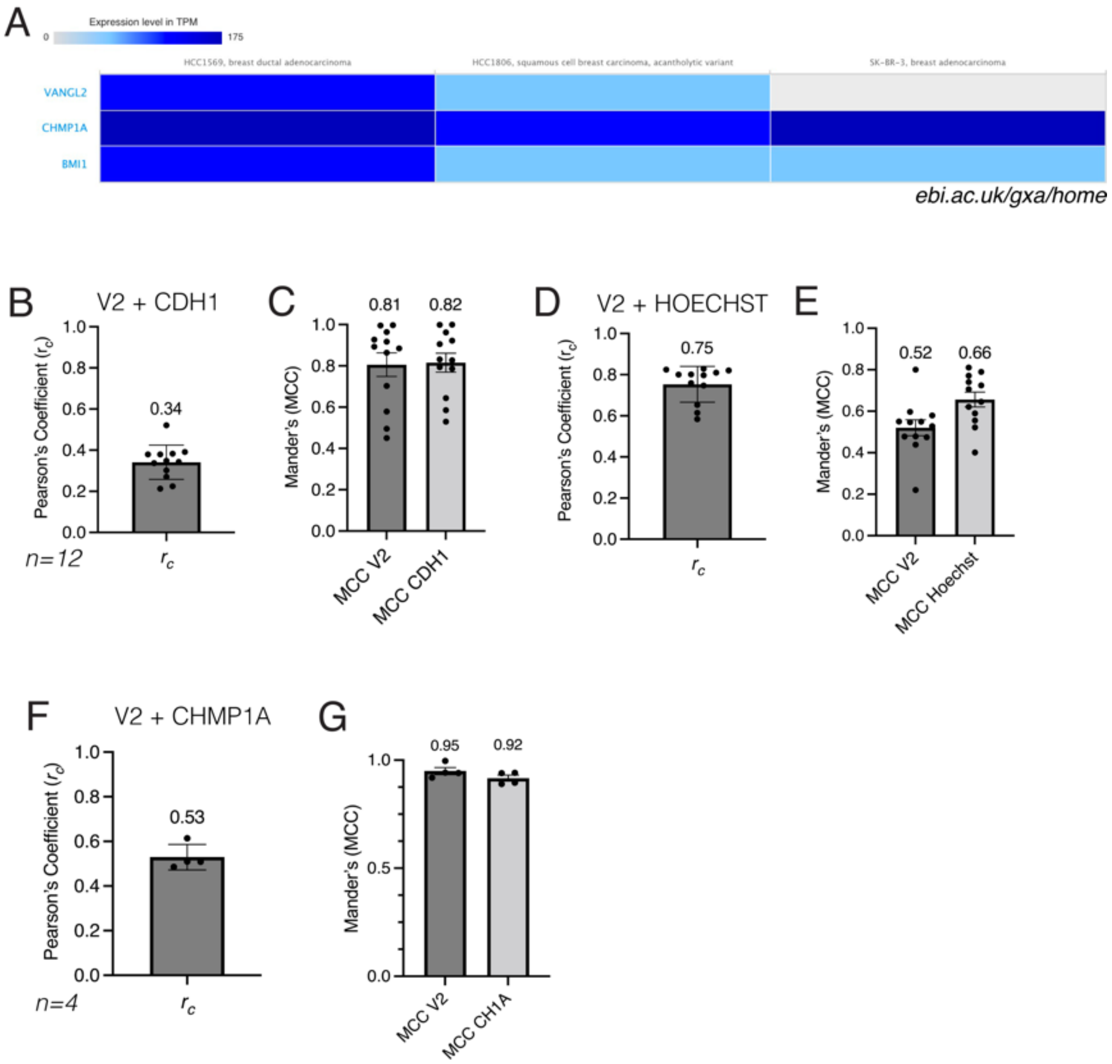

Supplementary Figure 2.1 Supporting data for the subcellular expression of VANGL2 in HCC1569 cells

A) Heat map, generated using the Expression Atlas, colored by the normalized and scaled expression values of Vangl2, Chmp1a, and Bmi1 for three breast cancer cell lines, HCC1569, HCC1806, and SK-BR-3. We selected the HCC1569 cell line because of its abundant expression of Vangl2, Chmp1a, and Bmi1 allowing for robust detection of the proteins in immunocytochemistry analysis.

B-C) Plots of the co-localization coefficient values for VANGL2 and CDH1. Pearson's colocalization coefficient (r_c) of 0.34±0.03 and Mander's colocalization coefficient (MCC), MCC_{V2}= 0.81±0.06), and MCC_{CDH1}= 0.82±0.05). Mean ± SEM. N=12.

D-E) Plots of the co-localization coefficient values for VANGL2 and HOECHST. Pearson’s colocalization coefficient (r_c) of 0.75±0.03 and Mander’s colocalization coefficient (MCC), MCC_{V2} = 0.52±0.04, and $MCC_{HOECHST}$ = 0.66±0.04. Mean ± SEM. N=12.

F-G) Plots of the co-localization coefficient values for VANGL2 and CHMP1A. Pearson’s colocalization coefficient (r_c) of 0.53±0.03and Mander’s colocalization coefficient (MCC), MCC_{V2}= 0.95±0.02, and MCC_{CHMP1A}= 0.92±0.01. Mean ± SEM. N=4.

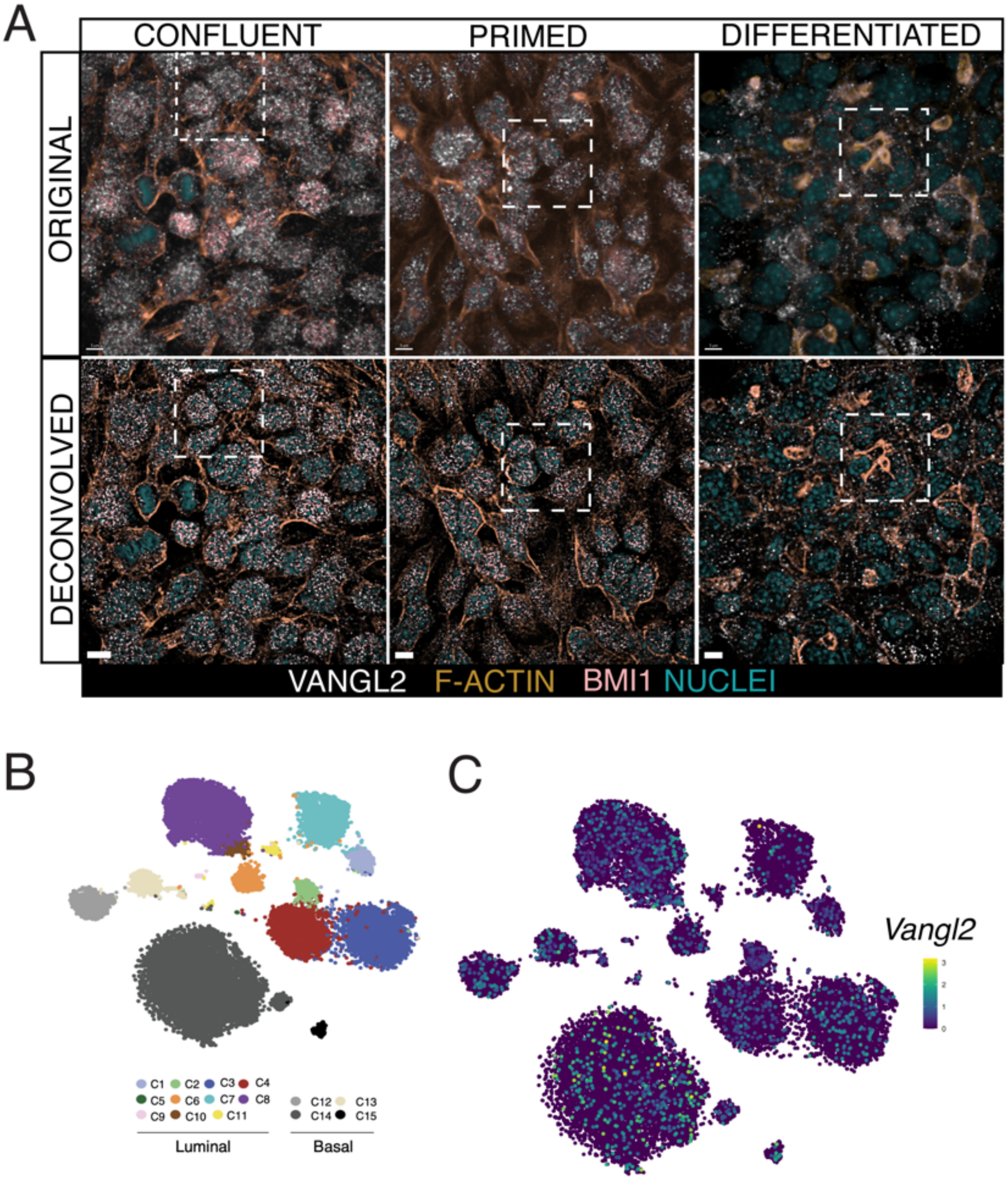

Supplementary Figure 2.2 The expression of VANGL2 in mammary gland cells

A) Representative micrographs of HC11 cells at different stages of differentiation: confluent (B), primed (C) and differentiated (D). The top row shows the images in their original state and the bottom row shows the images post deconvolution.

B) sc-RNAseq cell clusters based on cell type as indicated by the different colors.

C) The scaled expression of *Vangl2* across the different cell types.

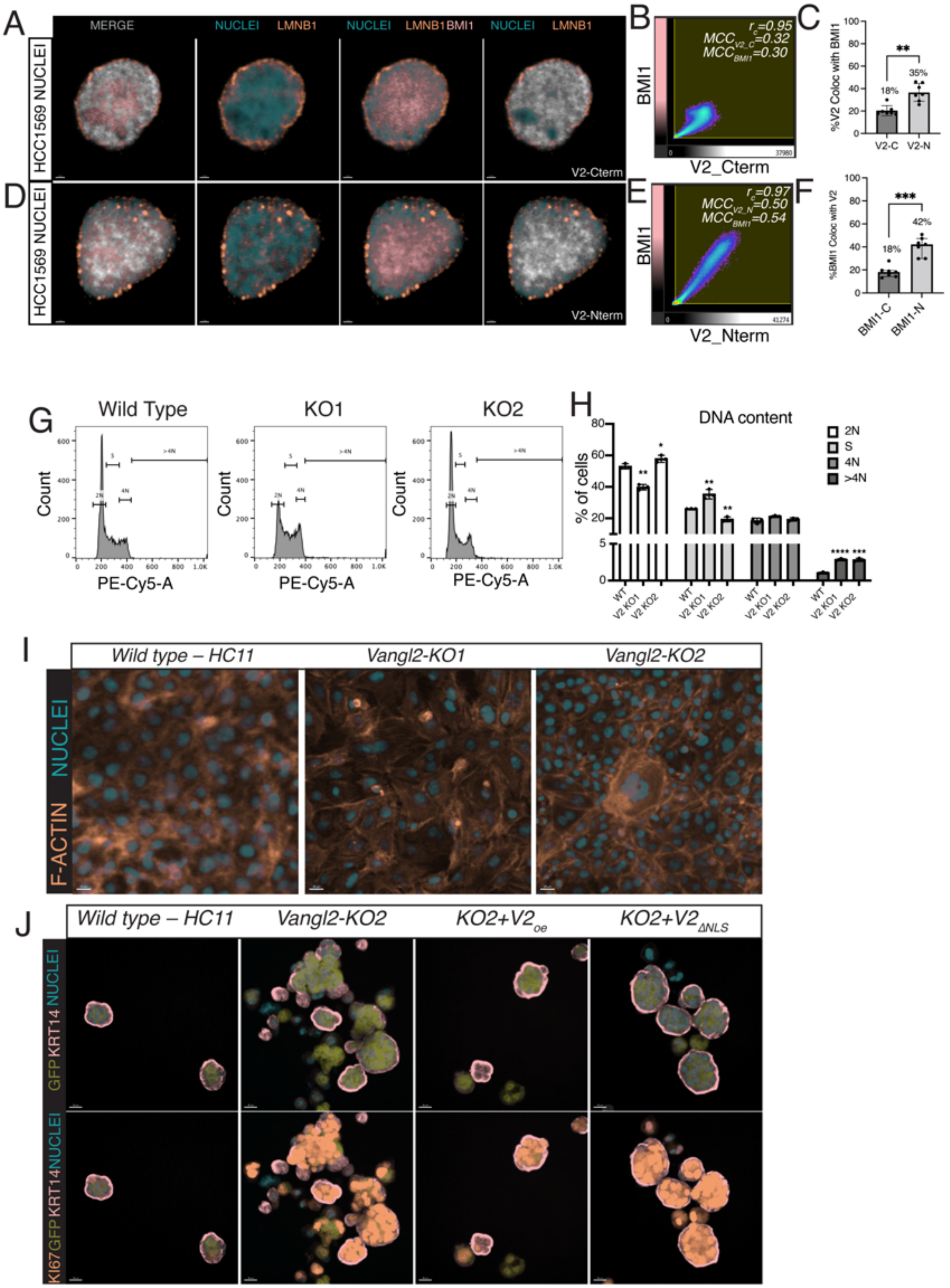

Supplementary Figure 2.3 VANGL2 in the nuclei of mammary gland cells

A) Nuclei isolated from HC1569 cells are immunolabeled with nuclear Lamin B1 (LMNB1, gold), BMI1 (pink), VANGL2 targeting C-terminal (white), and DNA dye HOECHST (Nuclei, blue). Scale=1 µm.

B) Co-localization scatterplot for V2_Cterm (*x*-axis) and BMI1 (*y*-axis). ROI in yellow box.

C) Plot of the quantification for the percent of voxels that are colocalized in the nuclei of HC11 cells (Mander's colocalization coefficient (MCC), $MCC_{V2\_C} = 0.32 \pm 0.03$, and $MCC_{BMI1} = 0.3 \pm 0.03$, Pearson's colocalization coefficient (r_c) of 0.95 ± 0.001. Mean ± SEM. *n*=7.

D) Nuclei isolated from HC1569 cells are immunolabeled with nuclear Lamin B1 (LMNB1, gold), BMI1 (pink), VANGL2 targeting N-terminal (white), and DNA dye HOECHST (Nuclei, blue).

E) Co-localization scatterplot for V2_Nterm (*x*-axis) and BMI1 (*y*-axis). ROI in yellow box.

F) Plot of the quantification for the percent of voxels that are colocalized in the nuclei of HC11 cells (Mander's colocalization coefficient (MCC), $MCC_{V2\_N} = 0.5 \pm 0.04$, and $MCC_{BMI1} = 0.54 \pm 0.02$, Pearson's colocalization coefficient (r_c) of 0.97 ± 0.003. Mean ± SEM. N=7.

G) Cell cycle analysis of of HC11 Wild type and *Vangl2* KO cells stained with propidium iodide (PI).

H) The DNA content of these cells was measured for the different levels of DNA content. P-values are determined using unpaired *t*-test with a Welch's correction. Significance is denoted as non-significant ($P \geq 0.05$), ns, significant ($0.05 < P < 0.01$), *, very significant ($0.01 < P < 0.001$), **, and extremely significant ($P < 0.001$), ***, ****.

I) 2D images of HC11 Wild type and *Vangl2* KO cells stained with Phalloidin (F-actin, gold) and HOECHST (DNA Dye, blue) showing the difference in size. The KO cells are larger than the Wild type cells. Scale=10 µm.

J) HC11 cells grown in 3D and immunolabeled for the basal cell marker Keratin 14 (KRT14, pink), proliferation marker Ki67 (gold), and DNA dye (HOECHST, blue), row 1. To exhibit their change in proliferation the cultures are shown in the second row with Ki67. Each column represents an independent condition, Wildtype (column 1), *Vangl2*-KO2 (column 2), *Vangl2*-KO + *Vangl2* overexpression construct (column 3), and *Vangl2*-KO + DNLS mutant construct (column 4). Scale=20 µm.

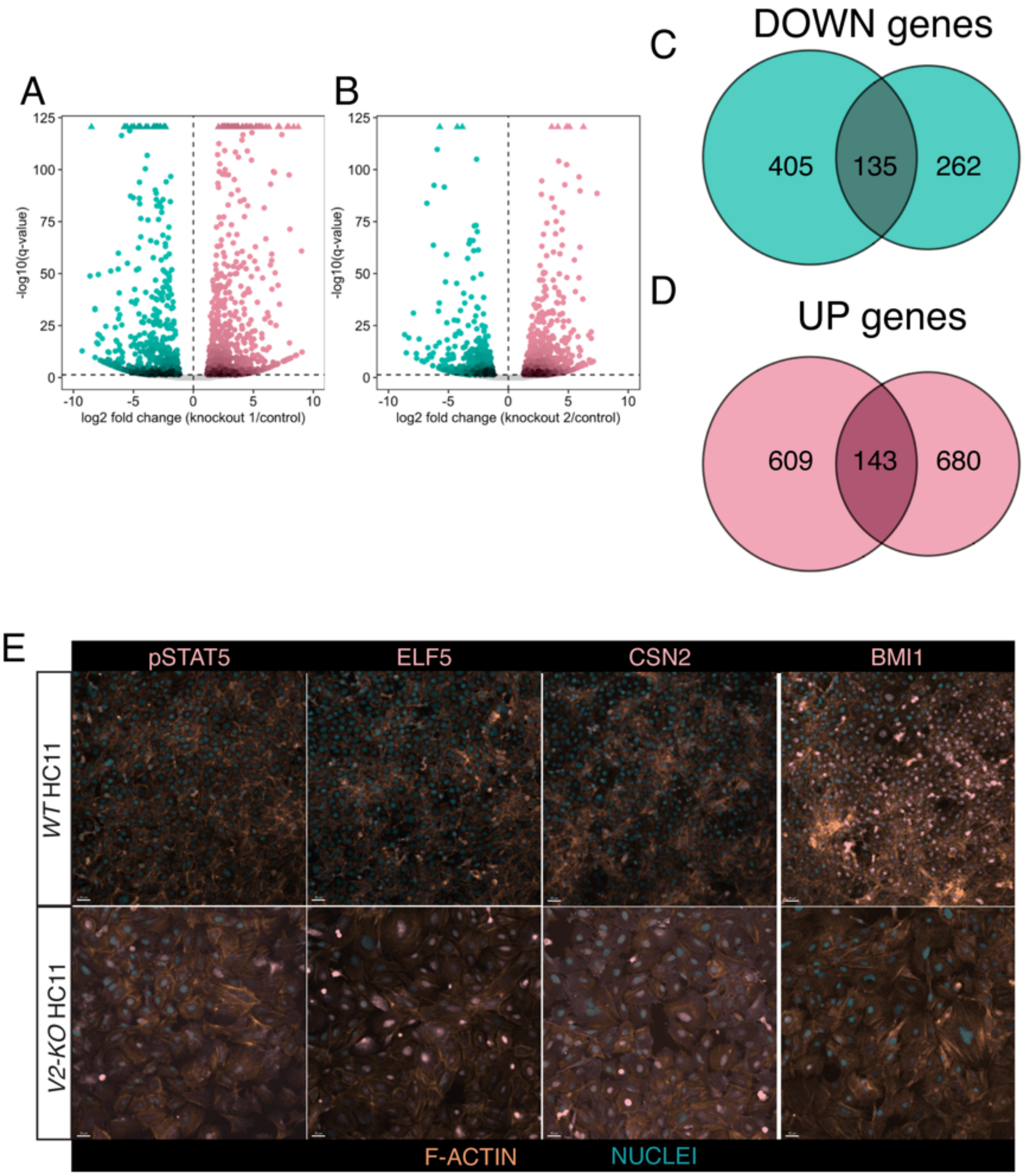

Supplementary Figure 2.4 Loss of *Vangl2* activates the Stat5 pathway

A-B) Volcano plots showing the differential expression of the *Vangl2*-KO1 and *Vangl2*-KO2 clones in comparison to Wild type. Each dot represents a gene, and the teal colors show the genes with low expression and the pink shows the genes that are upregulated in the KO samples.

C) Venn diagram showing the total number down genes in KO1, 405, and KO2, 262. The shared differentially expressed genes, 135, where used to generate the enriched pathway plots in the main figure.

D) Venn diagram showing the total number up genes in KO1, 609, and in KO2, 680. The shared differentially expressed genes, 143, where used to generate the enriched pathway plots in the main figure.

E) Zoomed out images of the immunocytochemistry of Wild type and *Vangl2*-KO HC11 cells to confirm RNA-seq results. The cells are immunolabeled with pSTAT5, ELF5, CSN2 and BMI1 (pink), F-ACTIN (Phalloidin, gold), and HOECHST (DNA dye, blue). The images also show the KO cells are larger than Wild type. Scale = 30 µm. N=15.

REFERENCES

1. Abdouh, M., Hanna, R., El Hajjar, J., Flamier, A., Bernier, G., 2016. The polycomb repressive complex 1 protein BMI1 is required for constitutive heterochromatin formation and silencing in mammalian somatic cells. J. Biol. Chem. 291, 182–197.

2. Adler, J., Parmryd, I., 2010. Quantifying Colocalization by Correlation : The Pearson Correlation Coefficient is Superior to the Mander ' s Overlap Coefficient. https://doi.org/10.1002/cyto.a.20896

3. Bach, K., Pensa, S., Grzelak, M., Hadfield, J., Adams, D.J., Marioni, J.C., Khaled, W.T., 2017. Differentiation dynamics of mammary epithelial cells revealed by single-cell RNA sequencing. Nat. Commun. 8.

4. Baghirova, S., Hughes, B.G., Hendzel, M.J., Schulz, R., 2015. MethodsX Sequential fractionation and isolation of subcellular proteins from tissue or cultured cells. MethodsX 2, 440–445.

5. Biehs, B., Hu, J.K.-H., Strauli, N.B., Sangiorgi, E., Jung, H., Heber, R.-P., Ho, S., Goodwin, A.F., Dasen, J.S., Capecchi, M.R., Klein, O.D., 2013. BMI1 represses Ink4a/Arf and Hox genes to regulate stem cells in the rodent incisor. Nat. Cell Biol. 15, 846–852.

6. Butler, M.T., Wallingford, J.B., 2017. Planar cell polarity in development and disease. Nat. Publ. Gr. 18, 375–388.

7. Chen EY, Tan CM, Kou Y, Duan Q, Wang Z, Meirelles GV, Clark NR, Ma'ayan A. Enrichr: interactive and collaborative HTML5 gene list enrichment analysis tool. BMC Bioinformatics. 2013; 128(14).

8. Cho, J.-H., Dimri, M., Dimri, G.P., 2013. A positive feedback loop regulates the expression of polycomb group protein BMI1 via WNT signaling pathway. J. Biol. Chem. 288, 3406–18.

9. Devenport, D., D. Oristian, E. Heller, and E. Fuchs. 2011. Mitotic internalization of planar cell polarity proteins preserves tissue polarity. *Nat Cell Biol*. 13:893-902.

10. Devenport, D., 2014. The cell biology of planar cell polarity. J. Cell Biol. 207, 171–179.

11. Gao, B., Ajima, R., Yang, W., Li, C., Song, H., Anderson, M.J., Liu, R.R., Lewandoski, M.B., Yamaguchi, T.P., Yang, Y., 2018. Coordinated directional

outgrowth and pattern formation by integration of wnt5a and Fgf signaling in planar cell polarity. Dev. 145.

12. Giese, A.P., J. Ezan, L. Wang, L. Lasvaux, F. Lembo, C. Mazzocco, E. Richard, J. Reboul, J.P. Borg, M.W. Kelley, N. Sans, J. Brigande, and M. Montcouquiol. 2012. Gipc1 has a dual role in Vangl2 trafficking and hair bundle integrity in the inner ear. *Development*. 139:3775-3785.

13. Giri, D.K.; Ali-Seyed, M.; Li, L.Y.; Lee, D.F.; Ling, P.; Bartholomeusz, G.; Wang, S.C.; Hung, M.C. Endosomal Transport of ErbB-2: Mechanism for Nuclear Entry of the Cell Surface Receptor. Mol. Cell. Biol. 2005, 25,11005–11018.

14. Gong, Y., Li, Z., Zou, S., Deng, D., Lai, P., Hu, H., Yao, Y., Hu, L., Zhang, S., Li, K., Wei, T., Zhao, X., Xiao, G., Chen, Z., Jiang, Y., Bai, X., Zou, Z., 2021. Vangl2 limits chaperone-mediated autophagy to balance osteogenic differentiation in mesenchymal stem cells. Dev. Cell 56, 2103-2120.e9.

15. Guo, B.H., Y. Feng, R. Zhang, L.H. Xu, M.Z. Li, H.F. Kung, L.B. Song, and M.S. Zeng. 2011. Bmi-1 promotes invasion and metastasis, and its elevated expression is correlated with an advanced stage of breast cancer. *Mol Cancer*. 10:10.

16. Hagenmueller, M., J.H. Riffel, E. Bernhold, J. Fan, H.A. Katus, and S.E. Hardt. 2014. Dapper-1 is essential for Wnt5a induced cardiomyocyte hypertrophy by regulating the Wnt/PCP pathway. *FEBS Lett*. 588:2230-2237.

17. Heck, B.W., Devenport, D., 2017. Trans-endocytosis of Planar Cell Polarity Complexes during Cell Division. Curr. Biol. 27, 3725-3733.e4.

18. Howard, T.L., Stauffer, D.R., Degnin, C.R., Hollenberg, S.M., 2001. CHMP1 functions as a member of a newly defined family of vesicle trafficking proteins. J. Cell Sci. 114, 2395–2404.

19. Kosugi S., Hasebe M., Tomita M., and Yanagawa H. (2009) Systematic identification of yeast cell cycle-dependent nucleocytoplasmic shuttling proteins by prediction of composite motifs. Proc. Natl. Acad. Sci. USA 106, 10171-10176.

20. Kosugi S., Hasebe M., Matsumura N., Takashima H., Miyamoto-Sato E., Tomita M., and Yanagawa H. (2009) Six classes of nuclear localization signals specific to different binding grooves of importin α. J. Biol. Chem. 284, 478-485.

21. Kosugi S., Hasebe M., Entani T., Takayama S., Tomita M., and Yanagawa H. (2008) Design of peptide inhibitors for the importin α/β nuclear import pathway by activity-based profiling. Chem. Biol. 15, 940-949.

22. Kowalczyk, I., C. Lee, E. Schuster, J. Hoeren, V. Trivigno, L. Riedel, J. Gorne, J.B. Wallingford, A. Hammes, and K. Feistel. 2021. Neural tube closure requires the endocytic receptor Lrp2 and its functional interaction with intracellular scaffolds. *Development*. 148.

23. Kuleshov MV, Jones MR, Rouillard AD, Fernandez NF, Duan Q, Wang Z, Koplev S, Jenkins SL, Jagodnik KM, Lachmann A, McDermott MG, Monteiro CD, Gundersen GW, Ma'ayan A. Enrichr: a comprehensive gene set enrichment analysis web server 2016 update. Nucleic Acids Research. 2016; gkw377.

24. Le Grand, F., Jones, A.E., Seale, V., Scimè, A., Rudnicki, M.A., 2009. Wnt7a Activates the Planar Cell Polarity Pathway to Drive the Symmetric Expansion of Satellite Stem Cells. Cell Stem Cell 4, 535–547.

25. Lehmann, L., Ferrari, R., Vashisht, A.A., Wohlschlegel, J.A., Kurdistani, S.K., Careys, M., 2012. Polycomb repressive complex 1 (PRC1) disassembles RNA polymerase II preinitiation complexes. J. Biol. Chem. 287, 35784–35794.

26. Li, H., F. Song, X. Chen, Y. Li, J. Fan, and X. Wu. 2014. Bmi-1 regulates epithelial-to-mesenchymal transition to promote migration and invasion of breast cancer cells. *Int J Clin Exp Pathol*. 7:3057-3064.

27. Liu, F., Pawliwec, A., Feng, Z., Yasruel, Z., Lebrun, J.J., Ali, S., 2015. Prolactin/Jak2 directs apical/basal polarization and luminal linage maturation of mammary epithelial cells through regulation of the Erk1/2 pathway. Stem Cell Res. 15, 376–383. https://doi.org/10.1016/j.scr.2015.08.001

28. Luis, N.M., Morey, L., Di Croce, L., Benitah, S.A., 2012. Polycomb in stem cells: PRC1 branches out. Cell Stem Cell 11, 16–21.

29. Mahaffey, J.P., J. Grego-Bessa, K.F. Liem, Jr., and K.V. Anderson. 2013. Cofilin and Vangl2 cooperate in the initiation of planar cell polarity in the mouse embryo. *Development*. 140:1262-1271.

30. Merte, J., D. Jensen, K. Wright, S. Sarsfield, Y. Wang, R. Schekman, and D.D. Ginty. 2010. Sec24b selectively sorts Vangl2 to regulate planar cell polarity during neural tube closure. *Nat Cell Biol*. 12:41-46; sup pp 41-48.

31. Mourgues, L., Imbert, V., Nebout, M., Colosetti, P., Neffati, Z., Lagadec, P., Verhoeyen, E., Peng, C., Duprez, E., Legros, L., Rochet, N., Maguer-Satta, V., Nicolini, F.-E., Mary, D., Peyron, J.-F., 2015. The BMI1 polycomb protein represses cyclin G2-induced autophagy to support proliferation in chronic myeloid leukemia cells. Leukemia 29, 1993–2002.

32. Pan, X., Sittaramane, V., Gurung, S., Chandrasekhar, A., 2014. Structural and temporal requirements of Wnt/PCP protein Vangl2 function for convergence and extension movements and facial branchiomotor neuron migration in zebrafish. Mech. Dev. 131, 1–14.

33. Paranjape, A.N., Balaji, S.A., Mandal, T., Krushik, E.V., Nagaraj, P., Mukherjee, G., Rangarajan, A., 2014. Bmi1 regulates self-renewal and epithelial to mesenchymal transition in breast cancer cells through Nanog. BMC Cancer 14, 1–14. https://doi.org/10.1186/1471-2407-14-785

34. Pherson, M., Misulovin, Z., Gause, M., Mihindukulasuriya, K., Swain, A., Dorsett, D., 2017. Polycomb repressive complex 1 modifies transcription of active genes. Sci. Adv. 3, e1700944.

35. Pietersen, A.M., Evers, B., Prasad, A.A., Tanger, E., Cornelissen-Steijger, P., Jonkers, J., van Lohuizen, M., 2008. Bmi1 Regulates Stem Cells and Proliferation and Differentiation of Committed Cells in Mammary Epithelium. Curr. Biol. 18, 1094–1099.

36. Pivetti, S., Fernandez-Perez, D., D'Ambrosio, A., Barbieri, C.M., Manganaro, D., Rossi, A., Barnabei, L., Zanotti, M., Scelfo, A., Chiacchiera, F., Pasini, D., 2019. Loss of PRC1 activity in different stem cell compartments activates a common transcriptional program with cell type–dependent outcomes. Sci. Adv. 5.

37. Planque, N. 2006. Nuclear trafficking of secreted factors and cell-surface receptors: new pathways to regulate cell proliferation and differentiation, and involvement in cancers. *Cell Commun Signal*. 4:7.

38. Puvirajesinghe, T.M., Bertucci, F., Jain, A., Scerbo, P., Belotti, E., Audebert, S., Sebbagh, M., Lopez, M., Brech, A., Finetti, P., Charafe-Jauffret, E., Chaffanet, M., Castellano, R., Restouin, A., Marchetto, S., Collette, Y., Gonçalvès, A., Macara, I., Birnbaum, D., Kodjabachian, L., Johansen, T., Borg, J.-P., 2016. Identification of p62/SQSTM1 as a component of non-canonical Wnt VANGL2–JNK signalling in breast cancer. Nat. Commun. 7, 10318.
39. Rubio, S., Cazares, O., Macias, H., Hinck, L., 2020. Generation of mosaic mammary organoids by differential trypsinization. J. Vis. Exp. 2020, 1–10. https://doi.org/10.3791/60742

40. Scelfo, A., Piunti, A., Pasini, D., 2015. The controversial role of the Polycomb group proteins in transcription and cancer: How much do we not understand Polycomb proteins? FEBS J. 282, 1703–1722.

41. Sheng, X., S. Gao, Y. Sheng, X. Xie, J. Wang, and Y. He. 2022. Vangl2 participates in the primary ciliary assembly under low fluid shear stress in hUVECs. *Cell Tissue Res*. 387:95-109.

42. Smith, P., N. Godde, S. Rubio, M. Tekeste, E.K. Vladar, J.D. Axelrod, D.J. Henderson, M. Milgrom-Hoffman, P.O. Humbert, and L. Hinck. 2019. VANGL2 regulates luminal epithelial organization and cell turnover in the mammary gland. *Scientific reports*. 9:7079.

43. Srinivasan, M., Bharali, D.J., Sudha, T., Khedr, M., 2017. Downregulation of Bmi1 in breast cancer stem cells suppresses tumor growth and proliferation 8, 38731–38742.

44. Stachowiak, M.K.; Maher, P.A.; Stachowiak, E.K. Integrative Nuclear Signaling in Cell Development—A Role for FGF Receptor-1. DNA Cell Biol. 2007, 26, 811–826

45. Stauffer, D.R., Howard, T.L., Nyun, T., Hollenberg, S.M., 2001. CHMP1 is a novel nuclear matrix protein affecting chromatin structure and cell-cycle progression. J. Cell Sci. 114, 2383–2393.

46. Taherbhoy, A.M., Huang, O.W., Cochran, A.G., 2015. BMI1-RING1B is an autoinhibited RING E3 ubiquitin ligase. Nat. Commun. 6, 1–13.

47. Tower-Gilchrist, C., S.A. Zlatic, D. Yu, Q. Chang, H. Wu, X. Lin, V. Faundez, and P. Chen. 2019. Adaptor protein-3 complex is required for Vangl2 trafficking and planar cell polarity of the inner ear. *Mol Biol Cell*. 30:2422-2434.

48. Wang, Y.-N.; Wang, H.; Yamaguchi, H.; Lee, H.-J.; Lee, H.-H.; Hung, M.-C. COPI-mediated retrograde trafficking from the Golgi to the ER regulates EGFR nuclear transport. Biochem. Biophys. Res. Commun. 2010,399, 498–504.

49. Wei, X.L., Dou, X.W., Bai, J.W., Luo, X.R., Qiu, S.Q., Xi, D. Di, Huang, W.H., Du, C.W., Man, K., Zhang, G.J., 2015. ERα inhibits epithelial-mesenchymal transition by suppressing Bmi1 in breast cancer. Oncotarget 6, 21704–21717.

50. Xie Z, Bailey A, Kuleshov MV, Clarke DJB., Evangelista JE, Jenkins SL, Lachmann A, Wojciechowicz ML, Kropiwnicki E, Jagodnik KM, Jeon M, & Ma'ayan A. Gene set knowledge discovery with Enrichr. Current Protocols, 1, e90. 2021.

51. Yamaji, D., Kang, K., Robinson, G.W., Hennighausen, L., 2013. Sequential activation of genetic programs in mouse mammary epithelium during pregnancy depends on STAT5A/B concentration. Nucleic Acids Res. 41, 1622–1636.

52. Yates, L.L., Schnatwinkel, C., Murdoch, J.N., Bogani, D., Formstone, C.J., Townsend, S., Greenfield, A., Niswander, L.A., Dean, C.H., 2010. The PCP genes Celsr1 and Vangl2 are required for normal lung branching morphogenesis. Hum. Mol. Genet. 19, 2251–2267.

Chapter 3: Generation of Mosaic Mammary Organoids by Differential Trypsinization

INTRODUCTION

The mammary gland (MG) is a tree-like, tubular epithelial structure embedded within an adipocyte rich stroma. The bilayered ductal epithelium comprises an outer, basal layer of contractile, myoepithelial cells (MyoECs) and an inner layer of luminal, secretory epithelial cells (LECs), encircling a central lumen[1]. During lactation when the outer MyoECs contract to squeeze milk from the inner alveolar LECs, the mammary gland undergoes numerous changes that are under the control of growth factors (e.g., EGF and FGF) and hormones (e.g. progesterone, insulin, and prolactin). These changes cause the differentiation of specialized structures, alveoli, which synthesize and secrete milk during lactation[1]. The mammary epithelia can be experimentally manipulated using techniques in which either epithelial tissue fragments, cells, or even a single basal cell are transplanted into host mammary fat pads, precleared of endogenous mammary parenchyma, and allowed to grow out to reconstitute an entire, functional epithelial tree[2-5]. Transplantation is a powerful technique, but it is time-consuming and impossible if a mutation results in early embryonic lethality (prior to E14) that prevents the rescue of transplantable mammary anlage. Furthermore, investigators frequently wish to research the roles of the two different compartments, which are derived from lineage-restricted progenitor cells. While Cre-lox technology allows differential genetic manipulation of MyoECs and

LECs, this is also a time-consuming and expensive undertaking. Thus, since the 1950s, investigators have used in vitro mammary organoids as a relatively easy and efficient way to address questions concerning mammary tissue structure and function[6,7].

In early protocols describing the isolation and culture of primary mammary epithelial cells, investigators found that a basement membrane matrix (BME), composed of a plasma clot and chicken embryo extract, was required for MG fragments grown on a dish[6]. In the following decades, extracellular matrices (ECMs, collagen, and jellylike protein matrix secreted by Engelbreth-Holm-Swarm murine sarcoma cells) were developed to facilitate 3D culture and better mimic the in vivo environment[7-10]. Culturing cells in 3D matrices revealed by multiple criteria (morphology, gene expression, and hormone responsiveness) that such a microenvironment better models in vivo physiological processes[9-12]. Research using primary murine cells identified key growth factors and morphogens necessary for the extended maintenance and differentiation of organoids[13]. These studies have set the stage for the protocol presented here, and for the culture of human breast cells as 3D organoids, which is now a modern clinical tool, allowing for drug discovery and drug testing on patient samples[14]. Overall, organoid culturing highlights the self-organization capacities of primary cells and their contributions to morphogenesis and differentiation.

Presented here is a protocol to culture murine epithelia that can be differentiated into milk-producing acini. A differential trypsinization technique is used to isolate the MyoECs and LECs that comprise the two distinct MG cell compartments. These separated cell fractions can then be genetically manipulated to overexpress or knockdown gene function. Because lineage-intrinsic, self-organization is an innate property of mammary epithelial cells[15-17], recombining these cell fractions allows researchers to generate bilayered, mosaic organoids. We begin by enzymatically digesting the adipose tissue, and then incubating the mammary fragments on a tissue culture dish for 24 h (**Figure** 3.**1**). The tissue fragments settle on polystyrene dishes as bilayered fragments with their in vivo organization: outer myoepithelial layer surrounding inner luminal layers. This cellular organization allows for the isolation of the outer MyoECs by trypsin-EDTA (0.5%) treatment for 3–6 min followed by a second round of trypsin-EDTA (0.5%) treatment that detaches the remaining inner LECs (**Figure** 3.**2**). Thus, these cell types with different trypsin sensitivity are isolated and can subsequently be mixed and plated in ECM (**Figure 3.1**). The cells undergo self-organization to form bilayered spheres, comprising an outer layer of MyoECs surrounding inner LECs. Lumen formation occurs as the cells grow in a medium containing a cocktail of growth factors (see recipes for Growth Medium)[13]. After 5 days, organoids can be differentiated into milk-producing acini by switching to Alveologenesis Medium (see recipes and **Figure 3.1 F**) and incubated for another 5 days. Alternatively, organoids will continue to expand and branch in Growth Medium for at least 10 days. Organoids can be analyzed using immunofluorescence (**Figure** 3.**3**

D–**F**) or released from the ECM using a recovery solution (see **Table of Materials**) and analyzed via other methods (e.g., immunoblot, RT-qPCR).

PROTOCOL:

All methods described here have been approved by the Institutional Animal Care and Use Committee (IACUC) of the University of California, Santa Cruz.

Day 1: Mammary gland digestion

1.1. Prepare to harvest the MGs from mature female mice 10–14 weeks of age.

1.1.1. Perform the harvesting on an open bench under aseptic conditions.

1.1.2. Sterilize all surgical supplies, cork boards, and pins by autoclaving and soaking in 70% alcohol for 20 min prior to surgery.

1.1.3. Anesthetize animals with sodium pentobarbital (2X anesthetic dose of 0.06 mg/g body weight) delivered via intraperitoneal injection with a 0.5 mL insulin syringe.

1.1.4. Monitor the level of anesthesia by pinching the animal's toes to check for a reflex response and commence the protocol only after the animal is fully anesthetized.

1.1.5. Place the animal on its back, pin its appendages to the corkboard, and wipe down its abdomen and chest with ethanol.

1.2. To harvest the #2, 3, 4, and 5 MGs from one mouse (i.e., 8 MGs, **Figure 1A**), identify the midline between the two hind legs and make a small incision (1 cm) on the abdominal skin with sharp scissors, then extend the cut up to the neck[18].

1.3. Follow by making small cuts laterally towards the legs and arms to allow for the release of the skin using a cotton swab. Pull the skin away and stretch it tight before pinning it down on one side (**Figure** 3.**1 B**, step 1)[18]. Remove the MGs by cutting under them, and remove the lymph nodes from the #4 glands (**Figure 1B**, steps 2, 3)[18]. Repeat the procedure on the other side of the body.

1.4. Collect the MG tissue in 50 mL of 4 ˚C Dulbecco's Modified Eagle's Media (DMEM)/Nutrient Mixture F12 (F12) supplemented with 5% fetal bovine serum (FBS) and 1X Antibiotic-Antimycotic (Anti-Anti)[18].

1.5. Chop the glands in a 35 mm dish or on a ceramic plate using a razor blade or tissue chopper. Rotate the plate every five manual chops or every round on the tissue chopper until the tissue pieces can fit through a 1 mL micropipette tip with ease (~0.1 mm/fragment, **Figure** 3.**1 C**).

1.6. Digest the MGs in Digestion Medium (see **Table 1**) for 14 h in a 6 well low adhesion dish at 37 ˚C, 5% CO_2.

Day 2: Isolation of mammary epithelial tissue fragments

2.1. After 14 h of digestion, gently mix by pipetting the digested tissue 10X using a 1 mL micropipette to break down any remaining stroma or adipose tissue, ensuring that neither bubbles nor excess mechanical force are generated.

NOTE**:** If there is incomplete digestion after 14 h, this could be due to the accumulation of sheared DNA. In this case, add 1 µL of 1 mg/mL deoxyribonuclease I (DNase I) per 2 mL of Digestion Medium. Incubate for another 30 min at 37 ˚C, 5% CO_2.

2.2. Collect tissue in a 15 mL tube and rinse the well used for digestion with 2–3 mL of tissue culture grade 1X Dulbecco's Phosphate Buffered Saline (DPBS) free of Ca^{2+} and Mg^{2+}. Centrifuge at 600 x *g* for 10 min.

2.3. Evacuate the supernatant containing the lipid layer and medium, and then resuspend the pellet in 5 mL of DPBS and switch to a new 15 mL tube. Centrifuge at 600 x *g* for 10 min.

2.4. During centrifugation place a 70 µm nylon cell strainer in a 50 mL tube and prewet the strainer using 10 mL of 37 ˚C DMEM/F12.

2.5. Resuspend tissue fragments from protocol step 2.4 using 5 mL of DPBS and pass the suspension through a prewet 70 µm nylon cell strainer to remove stromal cells and single cells (**Figure** 3.**1 D**).

2.6. Collect the tissue fragments on the cell strainer. Rinse 4X with 10 mL of 37 ˚C DMEM/F12 (**Figure** 3.**1 D**).

CAUTION: Incomplete rinsing will result in cultures contaminated with non-epithelial cells.

2.7. Release the tissue fragments by holding the strainer tab with gloved fingers, inverting the strainer over a 60 mm tissue culture dish and passing 1 mL aliquots of Maintenance Medium (see **Table 1**) through the bottom of the strainer 4X (**Figure** 3.**1 E**).

2.8. Check the strainer for tissue fragment remnants, which will be visible by the naked eye, and rinse the strainer 1X more with 1 mL of Maintenance Medium if any fragments are still adhering to the strainer. The rinsed tissue fragments should now be free of stromal cells.

2.9. Quickly examine the 60 mm dish containing the MG fragments from protocol step 2.8 under an inverted microscope (4X or 10X objective, **Figure** 3.**1 F**). A typical preparation of eight MGs yields ~500 fragments. Look for single cells or fat droplets and whether there are contaminating cells.

NOTE: If there are contaminating cells, repeat the filtration step by collecting the medium and fragments from the 60 mm dish using a 5 mL pipette and filtering the fragment again through a fresh 70 µm strainer, repeating protocol steps 2.6, 2.8–2.10.

2.10. Incubate 24 h at 37 ˚C, 5% CO_2, allowing the tissue fragment to adhere and generate bilayered fragments (**Figure** 3.**2 A**).

NOTE: If the fragments have not settled by 24 h, continue to incubate until adhered. If the fragments do not adhere well, the separation of the cell compartments will not work. If researchers are concerned about adhesion, the tissue culture plates can be treated to promote fragment attachment (e.g., poly-L-lysine).

Day 3: Differential trypsinization of myoepithelial and luminal epithelial cells

3.1. To separate MyoECs from LECs, empty the media from the dish, rinse 1x with 1 mL of DPBS and add 1 mL of fresh trypsin-EDTA (0.5%), and carefully monitor the digestion under an inverted microscope (10X or 20X objective, **Figure 2B**, **Figure C**, **Figure F**). The detachment of the outer MyoEC layer will require 3–6 min, depending on trypsin-EDTA (0.5%) strength.

NOTE: Please see **Figure 2** for representative images showing this process. Under brightfield illumination, the MyoECs appear rounded and have a brighter appearance in comparison to the LECs, which remain adhered in the center and appear darker.

3.2. Collect the MyoEC fraction in a 15 mL tube containing 2 mL 10% FBS/DPBS. Without disturbing the LECs, gently rinse the 60 mm dish with 2 mL of DPBS and then dispose of the DPBS (**Figure** 3.**2 H**–**I**).

NOTE: The usual recovery for MyoECs is within a range of (3.5 x 10^6–1.5 x 10^6) depending on the size of the MGs.

3.3. To remove the LEC fraction, add 1 mL of trypsin-EDTA (0.5%) to the dish again and incubate 7–15 min, monitoring carefully to prevent overdigestion. Quench the trypsin-EDTA (0.5%) on the dish with 2 mL of 10% FBS/DPBS. Collect the LEC fraction in a new 15 mL tube.

NOTE: The usual recovery for LECs is within a range (2×10^6–4.2×10^6) depending on the size of the MGs. Routinely, the purity of both fractions as assayed by immunohistochemistry is ~90%[19] (**Figure** 3.**2 E**).

3.4. Centrifuge each fraction for 5 min at 300 x *g* to remove the trypsin-EDTA (0.5%). Resuspend the pellet in 250 µL of Maintenance Medium and count each cell population using a hemocytometer or automated cell counter. Place the cells on ice while counting.

NOTE: If genetic manipulation of the cell fractions is desired, primary cells can be grown on low adhesion dishes and infected with lentivirus[20].

Day 3: Combining and embedding cell fractions in an extracellular matrix

NOTE: Once the MyoEC and LEC fractions have been collected and counted, they can be combined. The typical MyoEC/LEC ratio is 1:3 (**Figure 3A**)[19]. Different studies can be performed. For example, to perform mosaic studies, fractions can be generated from wild type (WT) and mutant (Mut) mice and combined (MyoEC/LEC: WT/WT; WT/Mut; Mut/WT; Mut/Mut)[21], or fractions can be combined using different ratios of MyoECs/LECs[19].

4.1. Based on cell counts, calculate the number of wells (8 well chamber, see **Table of Materials**) that need to be prepared for 12,000 cells/well (e.g. 3,000 MyoECs:9,000 LECs).

4.2. Establish the base layer for 3D culture by adding 90 μL of 50% ECM (50% ECM/50% DMEM/F12, without phenol red – see the **Table of Materials**) to each well. Ensure there are no bubbles and the wells are coated evenly. To solidify the base layer, incubate the slides at 37 ˚C, 5% CO_2 for 30 min.

Note: The ECM needs to stay ice-cold until this step, otherwise it will polymerize prematurely and lead to uneven base coating and polymerization. Using a base ECM enhances organoid growth in a single plane, which aids image capture. This also obtains faster organoid growth and uses less ECM[22].

4.3. During polymerization, prepare the cell mixes. Pellet the MyoEC and LEC fractions at 300 x *g* for 5 min and resuspend each cell fraction in 10% ECM/90% Growth Medium so each well has 100 μL (see **Table 1** for how to make Growth Medium).

Note: For ease of preparation, replicate wells using the same cell mixes. These can be combined and prepared in one tube (e.g., four wells of the same cell mix can be prepared in 400 μL of 10% ECM/90% Growth Medium).

4.4. Add 100 µL of each cell mix in 10% ECM/90% Growth Medium to each well and allow organoids to settle for 20 min at 37 ˚C, 5% CO_2.

4.5. Once the cells have settled, gently add 100 µL of Growth Medium by gently pipetting down the chamber wall of each well. Incubate the slides at 37 ˚C, 5% CO_2 (see **Figure 3A** for the total composition of each well).

NOTE: The Rho Kinase inhibitor, R-spondin, and Nrg1 are factors that have been identified as important for the long-term culture of organoids grown from both primary murine mammary cells and human breast cancer cells[13,14]. In addition, the stem cell factors B27 and N2 extend the time that organoids can be cultured.

4.6. Image cells every 24 h to track their growth and gently renew the Growth Medium every 2–3 days using 100 µL/well (**Figure** 3.**3 B**–**E**).

NOTE: Use extreme care when renewing the medium. Tilt the chamber slides to collect the medium at one corner of the wells. Remove ≤100 µL of the medium and replenish with care to leave the ECM layer undisturbed.

4.7. If researchers are interested in investigating lactation/alveologenesis, switch to Alveologenesis Medium (see **Table 1**) on day 5 and continue to renew the medium every 2–3 days until day 10 (**Figure 3F**) or beyond by passaging using recovery solution (see the **Table of Materials**)[13].

NOTE: At this point, organoids can be isolated from the ECM by incubating at 4 ˚C in 400 µL of 4 ˚C recovery solution (see **Table of Materials** for protocol and reagent info).

Day 5 or 10: Fixing and immunostaining organoids

5.1. Remove the medium carefully by gently pipetting off the media (a bulb pipette works best). Rinse each well using 200 µL of 1x Dulbecco's Phosphate Buffered Saline (DPBS, see recipes).

5.2. Fix the organoids using cold (4 ˚C) 4% (w/v) paraformaldehyde (PFA, see recipes) for 10 min at room temperature.

CAUTION: PFA is hazardous. Wear personal protective equipment (lab coat, gloves, and safety glasses). This step should be performed inside a fume hood.

NOTE: The ECM is dissolved by the PFA treatment. Incomplete ECM removal can lead to background staining when the organoids are analyzed by immunofluorescence.

5.3. Remove the 4% PFA and add 200 µL of 0.2% (w/v) glycine/DPBS (see **Table 1**) to each well. Incubate the slides at room temperature for 30 min or 4 ˚C overnight on a rocking surface set to a slow setting.

NOTE: The organoids can be stored for 1–3 days in DPBS at 4 ˚C prior to the next step.

5.4. Permeabilize the organoids using DPBS + 0.25% Triton X-100 (PBST, see **Table 1**) for 10 min at room temperature.

5.5. Block the organoids using 5% donkey serum (DS) in DPBS for 1 h on a rocking surface.

NOTE: This step can be performed overnight at 4 ˚C on a rocking surface.

5.6. Prepare primary antibodies in 1% DS/DPBS. Use 125–200 µL for each well. Perform immunostaining by incubating the organoids in primary antibody overnight at 4 ˚C on a rocking surface.

Day 11: Complete immunofluorescence

6.1. Wash each well 2X with 200 µL PBST for 5 min. Add secondary antibody in 1% DS/DPBS using 125–200 µL for each well. Incubate at room temperature on a rocking surface for 45 min.

6.2. Wash each well 2X using 200 µL DPBS per well.

6.3. Stain the nuclei using Hoechst DNA dye in DPBS (1:2,000 in DPBS) for 5 min at room temperature.

6.4. Remove all liquid left on the well by gently suctioning with a vacuum.

6.5. Carefully remove the chambers and gasket, place one drop (~30 µL) of mounting media (see **Table of Materials**) on each well and coverslip, taking care to remove bubbles. Allow the slide to dry in a dark space for 1–2 days. Seal with clear nail polish. Image the organoids on a confocal microscope (**Figure** 3.**3 E**–**F**).

REPRESENTATIVE RESULTS:

The protocol presented here describes a method for investigating specific lineage contributions of mammary epithelial cells by making use of mosaic organoids. To obtain primary murine cells for organoids, the mammary gland epithelium must first be isolated from the surrounding adipocyte rich stroma (**Figure 1**). This process is described briefly here and is also described in a previously published study[18]. To obtain enough cells, it is recommended that #2, 3, 4, and 5 MGs be removed (**Figure 1A**). An important step key to isolating a pure population of epithelial cells is removal of the lymph nodes from the #4 MGs, which are rich in immune cells that will contaminate the preparation (**Figure** 3.**1 A**, **B**). The MGs were minced to generate fragments ~0.1 mm in size (**Figure** 3.**1 B**). The tissue fragments were then enzymatically digested, a process occurring in the presence of collagenase, to release epithelia from stroma, and in the absence of trypsin, to prevent the digestion of proteins such as cadherins that maintain cell-cell contacts. The digested tissue was then centrifuged to remove lipids and filtered through a cell strainer and washed (**Figure** 3.**1 C**). Epithelial fragments, adhering to the strainer, were released by inverting the filter and washing the membrane, which transferred the epithelial fragments onto a polystyrene dish (**Figure 1D**). These fragments appeared as small, branched structures (**Figure** 3.**1 E**).

The purified epithelial fragments were incubated for 24 h. They settled down onto the dish and adhered, forming flat, pancake-like structures with an outer layer of

MyoECs encircling inner LECs (**Figure** 3.**2 A**–**B**). **Figure 2C** shows the edge of such a pancake-like structure from a wild type animal. Trypsin treatment differentially detached the MyoECs, which detached first and appeared as bright, rounded cells that encircled the core of remaining cuboidal LECs (**Figure** 3.**2 C**, **2F**). The detachment of the MyoECs was carefully monitored using brightfield microscopy and occurred within 3–6 min. Once the MECs were collected, LECs were subsequently detached through a second, longer trypsin treatment of 7–15 min. The time required for cell detachment depends on the trypsin concentration and freshness. The overall purity of the two cell compartments was ~90%, as assayed by counting cells that were KRT14-positive and E-Cadherin (CDH1)-negative in the MyoEC fraction and cells that were KRT14-negative and E-Cadherin-positive in the LEC fraction (**Figure 2D**–**E**)[19]. We discovered that some of the MyoECs were removed from the top of the pancake-like structure as well as from the outer edges. This was observed by using tissue fragments collected from mice labeled with an inducible, fluorescent basal marker (Cytokeratin 14 (KRT14)-CreERT1; R26RYFP/+) and injected with 75 mg/kg tamoxifen 5 days prior to harvest. In **Figure** 3.**2 F**, G the detachment of MyoECs from around the edges of the pancake structure is readily apparent. This occurred within the first 2 min of trypsin treatment (**Figure** 3.**2 F**). In addition, YFP-KRT14-positive cells were observed on top of the structure, where they rounded up after trypsin treatment and were removed by the rinse/collection step (**Figure** 3.**2 G**). The unlabeled core of LECs (**Figure** 3.**2 H**), which contained few or no YFP-KRT14-positive cells, (**Figure** 3.**2 I**) subsequently detached in the second round of trypsin treatment.

The MyoEC and LEC fractions were collected, combined, and embedded into 10% ECM plated onto a 50% ECM base. This allowed for better optical resolution of the organoids that grew primarily along the base layer (**Figure** 3.**3 A**). After 24 h, the cells assembled into aggregated structures that largely lacked a lumen (**Figure** 3.**3 B**). After 48 h, nascent organoids formed as the central lumens hollowed and appeared as a lighter internal space (**Figure** 3.**3 C**). After 10 days, the organoids were large, branched structures with well-developed lumens. Mosaic organoids generated from MyoECs harvested from wild type mice and LECs harvested from ACTb-EGFP mice were fixed in situ, immunostained with an antibody against the basal marker alpha-smooth muscle actin (SMA), and stained with the Hoechst DNA stain to show the nuclei. In the figures, the top and section views show different sets of images collected as a Z-stack and reconstructed into a 3D view (**Figure 3.3 D**). The top view reveals the branched morphology of the organoids (**Figure 3.3 E'**). The section view shows the bilayered epithelial structure and open lumen of these organoids (**Figure 3.3 E''**). These organoids can also be differentiated at Day 5 using Alveologenesis Medium and incubated for an additional 5 days (**Figure 3.3 F**). The organoids grew larger, had more branches, and contained milk. Differentiated organoids were generated as described above and immunostained with an antibody directed against the milk marker, whey acidic protein (WAP, **Figure** 3.**3 F**). WAP is a soluble protein secreted into milk. Much of this liquid was lost when the cells were fixed and immunostained in situ. Therefore, in the top and section views, WAP staining is visible intracellularly in secreting cells and extracellularly in milk that was trapped at the cell surface during fixation (**Figure 3.3 F**), although in section view a small organoid appears to contain liquid milk (**Figure** 3.**3 F''** boxed overlay).

DISCUSSION

Here, a method is presented detailing how researchers can generate 3D organoid cultures using primary MG cells. The difference between this and other protocols is that we detail a method to separate the two, distinct MG cell compartments: the outer basal MyoECs and inner LECs. Our method employs a two-step trypsin-EDTA (0.5%) treatment that we call differential trypsinization[19]. This procedure allows researchers to isolate basal and luminal cells without using sophisticated flow cytometry and thus can be used for studying MGs harvested from a wide variety of mammalian species that may not have the well-characterized biomarkers required for FACS. The ability to segregate the two cell subpopulations enables researchers to genetically modify the isolated cells independently or recombine cells from animals harboring genetic mutations or labels, and thus generate mosaic organoids in 3D culture. A limitation of the current protocol is that the stromal compartment is not included in the culturing conditions. However, new methods are being developed to coculture stromal components with organoids generated from either primary cells or cell lines to better recapitulate in vivo ECM[23-26], and these methods may be adapted to this protocol. In addition, it is important to note that while this protocol achieves a great enrichment of the MyoEC and LEC fractions (~90% purification), the fractions do not represent pure cell lineages.

The success of this protocol relies on a number of key steps. First, it is important to gently but thoroughly digest the MG tissue. Overdigestion of the tissue will lead to cell death and lower recovery of epithelial cells. Incomplete digestion will result in stromal and adipose cell contamination, which will interfere with later analyses (e.g., immunofluorescence, protein analysis, and mRNA measurements). Second, it is important to thoroughly rinse the MG tissue to remove contaminating cells in protocol step 2.8. In protocol step 2.9, the MG tissue fragments are released into a 60 mm dish. Researchers should monitor the released fragments immediately, before they adhere to the dish. If fat droplets or single cells are observed, protocol steps 2.6 and 2.8–2.11 must be repeated. To do this, the medium and tissue fragments are collected from the dish, placed into a new 70 µm strainer, washed 4X with 37 ˚C DMEM/F12 and then released into a new 60 mm dish. Third, it is essential to watch the first trypsin-EDTA (0.5%) incubation closely because the MyoECs can detach within the first 3 min, but they can also adhere for up to 6 min. There have been instances when the trypsin-EDTA (0.5%) was suboptimal, and incubation proceeded for 10 min with successful purification of MyoECs. However, >10 min of trypsinization resulted in the simultaneous collection of MyoECs and LECs. It is also important that the dish remain undisturbed during the first incubation. Otherwise, contamination of the MyoEC fraction with LECs can occur. The reverse is also true; if MyoECs are not completely detached from the dish, they will contaminate the LEC fraction. If researchers are using reporter mice that label MyoECs or LECs exclusively, it is easier to visualize the separation under a fluorescence microscope (**Figure** 3.**2 F**–**I**). Finally, if researchers plan on fixing organoids for immunofluorescence analyses, the pH (7.4) and temperature (4 ˚C) of the 4% PFA is important for successful dissociation of the ECM.

If the organoids are collected for other analyses (e.g., protein and mRNA measurements), it is important that the recovery solution be at 4 ˚C. If the ECM is not dissolving, incubation with the recovery solution can be extended by 10 min (i.e., 30 min total incubation). However, longer incubation periods will lead to loss of 3D structure and cell death. The recovery protocol (listed in the **Table of Materials**) specifies the use of wide-bore tips. This is important for maintaining the 3D structure of the organoids as well as the integrity of the cells.

In addition to these four key steps, there are two factors that influence the success of the protocol. First, organoid growth can be limited by genetic mutations that reduce cell proliferation and therefore reduce organoid growth in ECM. If only a few organoids are obtained, the subsequent fixation step frequently results in their loss. To address this, the number of cells embedded within the ECM should be increased while retaining the ratio of MyoECs:LECs (protocol steps 4.1–4.2). Second, once the cells are transferred into an ECM it is important to watch their growth daily and be vigilant about media renewal (every 2–3 days). This protocol specifies phenol red free reagents for better visualization, but the same success and growth is achieved using phenol red positive reagents. The days when medium renewal occurs prior to fixation (protocol step 4.6) should be performed with extreme care to reduce cell loss. The 10% ECM top layer is delicate; therefore, washes or medium renewal should be performed by pipetting fluid down the chamber walls to minimize mechanical disturbances.

Differentiation of the organoids into milk-producing acini requires treatment with differentiation supplements: hydrocortisone or dexamethasone, insulin, and prolactin. In this protocol, dexamethasone is recommended. In addition, while prolactin is commercially available, the prolactin used in this protocol was obtained from the National Hormone and Peptide Program. Again, it is very important to leave the organoids undisturbed when changing the Alveologenesis Medium. Differentiation requires a minimum of 5 days. This can be extended another 3–5 days, but the base layer of ECM degrades after 10–12 days. Differentiated organoids are filled with milk and their lumens appear darker.

This is an efficient technique that can be used to address compartment-specific, lineage contributions to mammary epithelial morphogenesis and differentiation. With this technique, researchers can generate mosaic organoids comprising differentially genetically manipulated MyoECs and LECs[21], or MyoECs and LECs obtained from mice harboring different genetic mutations. This allows researchers to better understand the contributions of lineage-specific cell compartments to organ morphogenesis and the acquisition of specialized functions such as milk production.

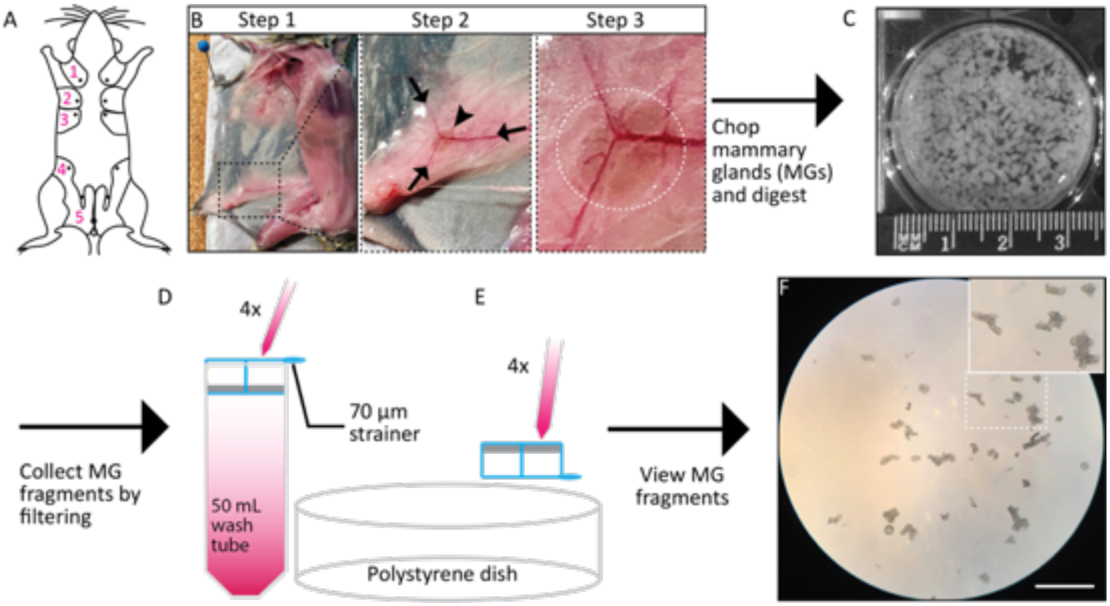

Figure 3.1. Mammary fragment isolation. (**A**) Labeled schematic of a mouse's 5 MGs with unlabeled, contralateral paired MGs. (**B**) Images of mouse MGs with the #4 MG boxed and magnified to show how to identify the lymph node for removal. (**C**) Image of chopped MGs in a 6 well low adhesion plate with a ruler showing the size of the tissue pieces (~0.1 mm each). (**D**–**E**) Schematic illustrating protocol steps 2.7–2.9. (**D**) MG fragments were filtered through a 70 µm strainer and rinsed 4X. (**E**) The strainer was then inverted over a 60 mm polystyrene tissue culture dish and fragments were released into the dish. (**F**) Image showing the filtered tissue fragments collected on a 60 mm dish that are free of stroma. The arrows point to the smallest fragments that are collected on the 70 µm strainer. Scale bar = 100 µm.

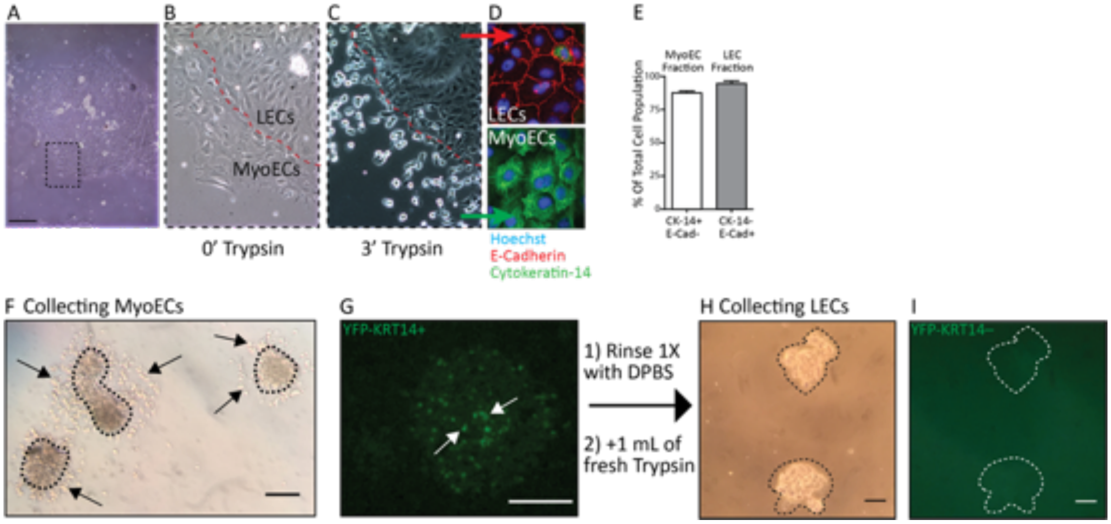

Figure 3.2. Differential trypsinization. (**A**) Brightfield image showing a tissue fragment adhered on a polystyrene dish, forming a pancake-like structure. (**B**–**C**) The first differential trypsinization step detached MyoECs that are clearly visible as bright, rounded cells after 3 min. (**D**) Immunofluorescent images of MyoECs (bottom) and LECs (top) using the Cytokeratin 14 (KRT14) cell marker for MyoECs, and E-Cadherin (CDH1) cell marker for LECs. (**E**) The expression of KRT14 and CDH1 was used to quantify the yield and purity of the differentially trypsinized cell fractions. (**F**–**I**). Representative phase-contrast and fluorescence (YFP) images of tissue fragments from Cytokeratin 14 (KRT14)-CreERT1; R26RYFP/+ MGs. Mice were injected with 75 mg/kg tamoxifen 5 days prior to harvest. (**F**) Detaching MyoECs (arrows) during the initial trypsin-EDTA (0.5%) 2 min after incubation. (**G**) A sprinkling of KRT14-YFP-MyoECs (arrows) on top of a pancake of unlabeled LECs. (**H**) Brightfield image of LECs after initial trypsinization and MyoEC detachment. (**I**) After MyoEC detachment, KRT14-YFP-MyoECs are no longer visible as shown by the absence of YFP expression. Scale bars = 30 µm (A, brightfield) 100 µm (F, brightfield), 50 µm (G, fluorescence), 100 µm (H, I). Panels A–E of this figure are modified from Macias et al.[19]

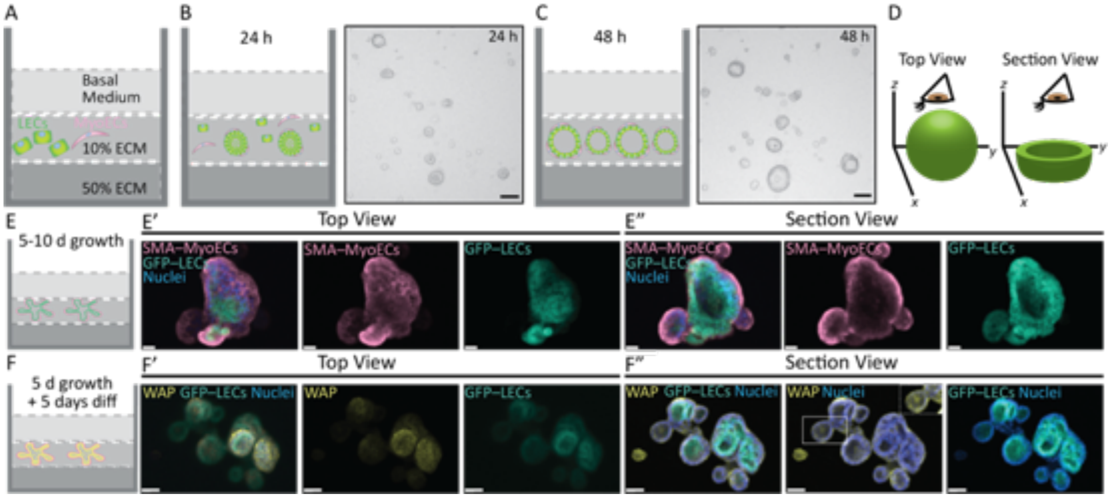

Figure 3.3. Three-dimensional organoid culture. (**A**) Schematic representation of single cells embedded in 10% ECM/90% Growth Medium and grown on a 50% ECM/50% DMEM base layer (protocol step 4.5). (**B–C**) Illustrations and phase-contrast images showing the rapid self-organizing capacities of mammary organoids generated from differentially trypsinized and recombined MyoECs and LECs at 24 h (**B**) and 48 h (**C**). Images collected using a digital widefield microscope (**D**) Schematic representation illustrating the top (left) or section (right) views used in E–F to show immunostained organoids. (**E**) Schematic representation of a single well of an 8 well chamber slide containing mammary organoids grown for 5–10 days in Growth Medium. (**E'-E"**) Top view (**E'**) and section view (**E"**) of immunostained organoids at day 10 of growth. MyoECs are marked with smooth actin muscle (SMA) in pseudocolor magenta. The LECs are from ACTb-EGFP mice and are shown in pseudocolor green. Nuclei were stained with Hoechst dye. (**F**) Schematic representation of a single well of an 8 well chamber slide containing mammary organoids grown for 5 days in Growth Medium and 5 days in Alveologenesis Medium. (**F'-F"**). Top view (**F'**) and section view (**F"**) of immunostained organoids at day 10 of growth. The MyoECs are unmarked. The LECs from ACTb-EGFP mice are shown in pseudocolor green. The milk protein, whey acidic protein (WAP), is shown in pseudocolor yellow in the LECs and coating the inside of the organoids' lumens. Nuclei were stained with Hoechst dye. Images collected using a spinning disk confocal microscope and reconstructed in 3D using Imaris (E', E') or bottom section ~30 slices (F', F"). Scale bars = 100 µm (C), 20 µm (E), 40 µm (F).

REFERENCES

1. Macias, H., Hinck, L. Mammary gland development. *Wiley Interdisciplinary Reviews in Developmental Biology*. **1** (4), 533–557 (2012).

2. Daniel, C. W., De Ome, K. B., Young, J. T., Blair, P. B., Faulkin, L. J., Jr. The in vivo life span of normal and preneoplastic mouse mammary glands: a serial transplantation study. *Proceedings of the National Academy of Science U S A.* **61** (1), 53–60 (1968).

3. Ip, M. M., Asch, B. B. *Methods in Mammary Gland Biology and Breast Cancer Research*. (Kluwer Academic/Plenum Publishers, 2000).

4. Shackleton, M. et al. Generation of a functional mammary gland from a single stem cell. *Nature.* **439** (7072), 84–88 (2006).

5. Stingl, J. et al. Purification and unique properties of mammary epithelial stem cells. *Nature.* **439** (7079), 993–997 (2006).

6. Lasfargues, E. Y. Cultivation and behavior in vitro of the normal mammary epithelium of the adult mouse. II. Observations on the secretory activity. *Experimental Cell Research.* **13** (3), 553–562 (1957).

7. Simian, M., Bissell, M. J. Organoids: A historical perspective of thinking in three dimensions. *Journal of Cell Biology*. **216** (1), 31–40 (2017).

8. Orkin, R. W. et al. A murine tumor producing a matrix of basement membrane. *Journal of Experimental Medicine.* **145** (1), 204–220 (1977).

9. Lee, E. Y., Parry, G., Bissell, M. J. Modulation of secreted proteins of mouse mammary epithelial cells by the collagenous substrata. *Journal of Cell Biology.* **98** (1), 146–155 (1984).

10. Lee, E. Y., Lee, W. H., Kaetzel, C. S., Parry, G., Bissell, M. J. Interaction of mouse mammary epithelial cells with collagen substrata: regulation of casein gene expression and secretion. *Proceedings of the National Academy of Science U S A.* **82** (5), 1419–1423 (1985).

11. Bissell, M. J., Barcellos-Hoff, M. H. The influence of extracellular matrix on gene expression: is structure the message? *Journal of Cell Science. Supplement.* **8**, 327–343 (1987).

12. Petersen, O. W., Ronnov-Jessen, L., Howlett, A. R., Bissell, M. J. Interaction with basement membrane serves to rapidly distinguish growth and differentiation pattern of normal and malignant human breast epithelial cells. *Proceedings of the National Academy of Science U S A.* **89** (19), 9064–9068 (1992).

13. Jarde, T. et al. Wnt and Neuregulin1/ErbB signalling extends 3D culture of hormone responsive mammary organoids. *Nature Commununications.* **7**, 13207 (2016).

14. Sachs, N. et al. A Living Biobank of Breast Cancer Organoids Captures Disease Heterogeneity. *Cell.* **172** (1–2), 373–386 e310 (2018).

15. Daniel, C. W., Strickland, P., Friedmann, Y. Expression and functional role of E- and P-cadherins in mouse mammary ductal morphogenesis and growth. *Developmental Biology*. **169** (2), 511–519 (1995).

16. Runswick, S. K., O'Hare, M. J., Jones, L., Streuli, C. H., Garrod, D. R. Desmosomal adhesion regulates epithelial morphogenesis and cell positioning. *Nature Cell Biology.* **3** (9), 823–830 (2001).

17. Chanson, L. et al. Self-organization is a dynamic and lineage-intrinsic property of mammary epithelial cells. *Proceedings of the National Academy of Science U S A.* **108** (8), 3264–3269 (2011).

18. Honvo-Houeto, E., Truchet, S. Indirect Immunofluorescence on Frozen Sections of Mouse Mammary Gland. *Journal of Visualized Experiments.* (106), e53179 (2015).

19. Macias, H. et al. SLIT/ROBO1 signaling suppresses mammary branching morphogenesis by limiting basal cell number. *Developmental Cell.* **20** (6), 827–840 (2011).

20. Welm, B. E., Dijkgraaf, G. J., Bledau, A. S., Welm, A. L., Werb, Z. Lentiviral transduction of mammary stem cells for analysis of gene function during development and cancer. *Cell Stem Cell.* **2** (1), 90–102 (2008).

21. Smith, P. et al. VANGL2 regulates luminal epithelial organization and cell turnover in the mammary gland. *Scientific Reports.* **9** (1), 7079 (2019).

22. Lee, G. Y., Kenny, P. A., Lee, E. H., Bissell, M. J. Three-dimensional culture models of normal and malignant breast epithelial cells. *Nature Methods.* **4** (4), 359–365 (2007).

23. Campbell, J. J., Davidenko, N., Caffarel, M. M., Cameron, R. E., Watson, C. J. A multifunctional 3D co-culture system for studies of mammary tissue morphogenesis and stem cell biology. *PLoS One.* **6** (9), e25661 (2011).

24. Labarge, M. A., Garbe, J. C., Stampfer, M. R. Processing of human reduction mammoplasty and mastectomy tissues for cell culture. *Journal of Visualized Experiments.* (71), e50011 (2013).

25. Marlow, R., Dontu, G. Modeling the breast cancer bone metastatic niche in complex three-dimensional cocultures. *Methods in Molecular Biology.* **1293**, 213–220 (2015).

26. Koledova, Z., Lu, P. A 3D Fibroblast-Epithelium Co-culture Model for Understanding Microenvironmental Role in Branching Morphogenesis of the Mammary Gland. *Methods in Molecular Biology.* **1501**, 217–231 (2017).

Chapter 4: ROBO1 inhibits NOTCH4 Nuclear localization in Estrogen Therapy Resistant Cancer Stem Cells

INTRODUCTION

Breast cancer onset is complex and how cells transform into cancerous cells is not well understood. The mammary gland is comprised of a heterogenous epithelial cell population organized into two main cell compartments, the outer myoepithelial cells (MyoECs) and the luminal epithelial cells (LECs). These subpopulations of cells are further sub-categorized into their respective hormone sensing abilities, estrogen or progesterone Receptor: ER^+ and PR^+ respectively (Visvader, 2014). Estrogen and progesterone are membrane soluble ligands that bind ER and PR, which are cytosolic proteins that when activated translocate to the nucleus to drive gene transcription. Therapies that target ER aim to inhibit its nuclear translocation. Hormone sensing mammary cells are the most frequent to transform into breast cancer cells and lead to the most common breast cancer, which is ER+ subtype (Dai, 2015). The ER is thus a frequent target for treatment with endocrine therapies, such as the selective ER modulator tamoxifen. ER^+ breast cancer cells, however, can acquire resistance to hormonal therapies, like tamoxifen, and consequently lose or mutate their ER; these cells then become refractory to treatment. Their gained resistance and loss of ER leads to the transformation of these cells into cancer stem cells (CSCs) or tumor initiating cells (TICs). Such breast cancer cells gain mobility and can traverse the blood vessels to become metastatic.

Many breast cancers are positive for the ER and are often treated with therapies that target the ER (Clarke, 2015). Tamoxifen is a selective ER modulator (SERM) that is the most frequent chemotherapy agent for patients harboring an ER+ breast cancer (Chang, 2012). Tamoxifen competes with estrogen binding to the estrogen receptor, thus blocking its downstream activity as a transcription factor. After a few years of tamoxifen exposure, a subset of cells can become resistant to the treatment, often because these cells loose or have modifications to the ER. This de novo gain-in-resistance is thought to occur in two ways, by silencing of the ER gene and by population remodeling (overpopulation of ER negative cells) (Chang, 2012). The loss or change of ER expression makes it impossible to target these cells using endocrine therapies and finding other cell receptors to target is important for treating such a prevalent disease. In addition to being difficult to target, these cells also become more proliferative and mobile leading to worse patient prognosis and tumor reoccurrence and worse patient prognosis. When the disease returns, it is more aggressive and difficult to treat, and more studies are needed to understand the molecular mechanisms that drive endocrine, therapy-resistant breast cancers.

In addition to the gained stem cell identity and abilities of these endocrine resistant breast cancer cells, they also undergo changes in gene and protein expression. Pathways that contribute to normal development frequently adopt different functions in a cancer setting. The SLIT/ROBO signaling pathway has been implicated in breast cancer and functions in a tumor context-specific fashion. In some tumors, SLIT/ROBO signaling can functions to promote oncogenesis by positively driving cell growth and migration (Zhou et al., 2011). In other contexts, SLIT/ROBO functions to suppress tumors and when the expression of these ligands or receptors decreases cells become more proliferative and gain more cancerous properties. The gene and protein expression changes that endocrine resistant cells undergo can contribute to the ability or inability to target these cells making it difficult to stop them before they expand.

ROBOs were originally identified as axon guidance receptors in the nervous system. The name ROBO comes from the word roundabout, which is a traffic circle. This term describes the appearance of neurons in the Robo Drosophila mutant in which the commissural axons circle the midline rather than extending outwards to innervate the periphery (Kidd, 1999; Ballard, 2012). ROBOs belong to the Ig-superfamily of receptors that are single pass transmembrane receptors containing no enzymatic activity. Instead, they mediate their action by binding to a variety of downstream signaling proteins. In Drosophila, ROBOs regulate axon guidance by binding small GTPases (e.g., Rac, Rho and Cdc42) and signaling to the actin cytoskeleton to govern the motility and directional outgrowth of neuronal growth cones (Bashaw, 2000). In mammals, there are 4 Robo receptors and their regulatory roles are more complex. In addition to governing axonal outgrowth, ROBOs also regulate cell proliferation/differentiation by controlling the subcellular localization of the transcription factors ß-Catenin and Snail (Macias 2011; Harburg 2014; Ballard 2015).

The SLITs are a conserved family of extracellular matrix secreted proteins that were originally discovered in the nervous system, where they signal through ROBO receptors to mediate axonal guidance and branching. In humans there are three Slit proteins (Slit1, Slit2, and Slit3) that are highly conserved structurally. The SLITs are composed of four unique leucine rich repeats (LLR, D1-4) that are connected via disulfide bonds at the N-terminus and seven to nine epidermal growth factor (EGF)-like domains along with laminin G-like domain capped by a cystine-module at the C-terminus. The SLITs are proteolytically cleaved within the fifth EGF-like domain to release an N-terminal fragment that bind Robo receptors and mediates cell guidance functions of Slit/Robo signaling (Nguyen Ba-Charvet et al., 2001). Beyond the nervous system the SLIT/ROBO signaling pathway has been implicated in driving the development of other branched tissues, like that of the mammary gland. Studies have hinted at SLIT/ROBO playing a role in breast cancer but there is little knowledge about it signaling in endocrine resistant breast cancers (Marlow, 2008; Legg, 2008; Dallol, 2002a; Prasad, 2008; Ballard, 2012).

NOTCH4 is type I transmembrane protein with an intracellular domain (ICD) that is cleaved by the γ-secretase. The $N4_{ICD}$ activates an array of stem cell transcription factors, and inhibiting its cleavage is frequently targeted by pharmacological inhibitors.

Keeping N4ICD out of the nucleus decreases the activity of CSCs and potentiates their differentiation. In a tamoxifen resistant cell line ROBO1 expression decreases and NOTCH4 signaling increases in comparison to control cells. Previous work in the Hinck lab has shown that during mammary alveologenesis, loss of *Robo1* in basal cells results in the nuclear accumulation of ß-catenin. This, in turn, upregulates *Jag1*, activating NOTCH signaling in the adjacent luminal cells. To probe the mechanism, we generated a peptide that spans the extracellular immunoglobin-like domains of ROBO1 (Ig5), a region that bind SLITs (Aleksandrova, 2018; Morlot, 2007). When we treated cells with the Ig5 peptide we inhibited the translocation of NOTCH4 to the nucleus. The exact mode of action of this Ig5 fragment remains unknown and further studies are necessary to understand how ROBO1 might be working with NOTCH4 at the cell membrane.

RESULTS

Loss of ROBO1 leads to an increase in the expression of the NOTCH4 intracellular domain ($N4_{ICD}$).

To test our hypothesis that ROBO1 expression levels influence that of NOTCH4 we analyzed the protein expression by western blotting of ROBO1 and NOTCH4 lysates from WT and *Robo1* knock-down MCF7 cells that are resistant to tamoxifen (Figure 4.2 A, B). Cell lysates from wild type and tamoxifen-resistant MCF7 cells in which *Robo1* is knocked-down (Figure 4.2 A) I found that NOTCH4 expression increases when ROBO1 expression is knocked-down (Figure 4.2 B). Though, this data only captures the expression pattern of one estrogen-resistant cell line and gained resistance can arise via different mechanism (e.g., mutations, chromatin modifications, cell identity changes). Work in other estrogen resistant cell lines is needed to understand this mechanism further. Alongside, cell lines that are resistant to other estrogen therapies is important (e.g., aromatase inhibitors). Increases in NOTCH4 expression is correlated with higher cancer stem cell activity and poor patient prognosis (Simoes, 2015). Cancer stem cells can initiate tumor formation and with gained estrogen therapy resistance these cells become extremely difficult to target for treatment. The retention of NOTCH4 at the cell membrane keeps these cells from becoming CSC and inhibits their tumorigenic activity.

The nuclear localization of $N4_{ICD}$ is regulated by ROBO1.

Inhibiting the nuclear localization of the NOTCH4 ICD keeps cells from adopting a CSC identity. Our lab generated a powerful reagent that allows for the direct interrogation of the ROBO1 and NOTCH4 collaborative function in CSC. This reagent is the five external IgG repeats of ROBO1 and recapitulates the binding of ROBO1 to SLITs. We discovered that ROBO1-Ig5 is also able to decrease the stem cell activity of estrogen resistant cells. To test the mechanism between ROBO1 and NOTCH4 I treated tamoxifen resistant cells with the Ig5 domain or the gamma secretase inhibitor (GSI, RO4929097) for five days. After five days, I fractionated the different cell fractions (membrane, cytosolic, and nuclear) from wild type and treated cells. To analyze if the treatments decreased the nuclear localization of the NOTCH4 intracellular domain ($N4_{ICD}$) I probed 50 μg of protein using western blotting (Figure 4.3 A). The data, comparing the treated nuclear samples to the untreated nuclear samples, show the Ig5 treatment inhibits $N4_{ICD}$ nuclear translocation at similar levels to the GSI treatment (Figure 4.3 B). These data are interesting because we know that Ig5 binds and sequesters the SLITs but what we don’t know is how sequestering the SLITs matters if *Robo1* is down regulated in these cells. We deduce that perhaps the other Robo protein, ROBO2 plays a role in this mechanism. Experiments that analyze the expression of ROBO2 in cells that are resistant to estrogen therapies are outstanding.

ROBO1 decreases the mammosphere formation efficiency of MCF7 cells.

Taking the observation from our western blot data that ROBO1 inhibits NOTCH4 ICD translocation, I tested the ROBO1-Ig5 ability to influence the formation of mammospheres. This activity can be measured by measuring the colony size of cells cultured in suspension, mammospheres, relative to the number of cells that are seeded. For this experiment, I seeded 1,000 cells of the parent line per well of a 6-well dish (TamR shScr and shR1) and allowed them to grow for five days under wild type conditions or Ig5 treatment. We find that ROBO1-IgG5 decreases the activity of CSCs using a well-established method in the breast cancer and mammary gland biology field that measures the stem cell activity of cells, mammosphere formation efficiency (MFE). These data present a novel and interesting role for ROBO1 in CSCs (Figure 4.4). The ROBO1 IgG fragment has the potential to serve as a novel targeted therapeutic of these transformed cells that are resistant to estrogen therapies.

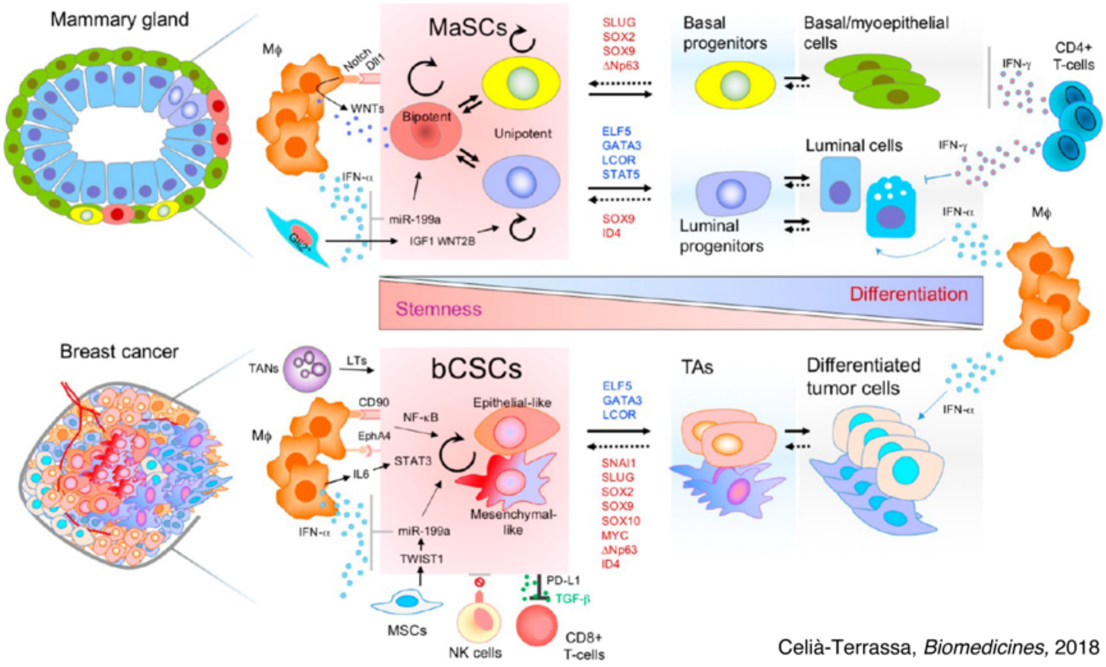

Celià-Terrassa, *Biomedicines,* 2018

Figure 4. 1 The mammary gland and breast cancer stemness hierarchy.

An illustration from a previously published paper that shows the different cell types in the mammary gland (top) and the breast cancer tumor cell composition (bottom).

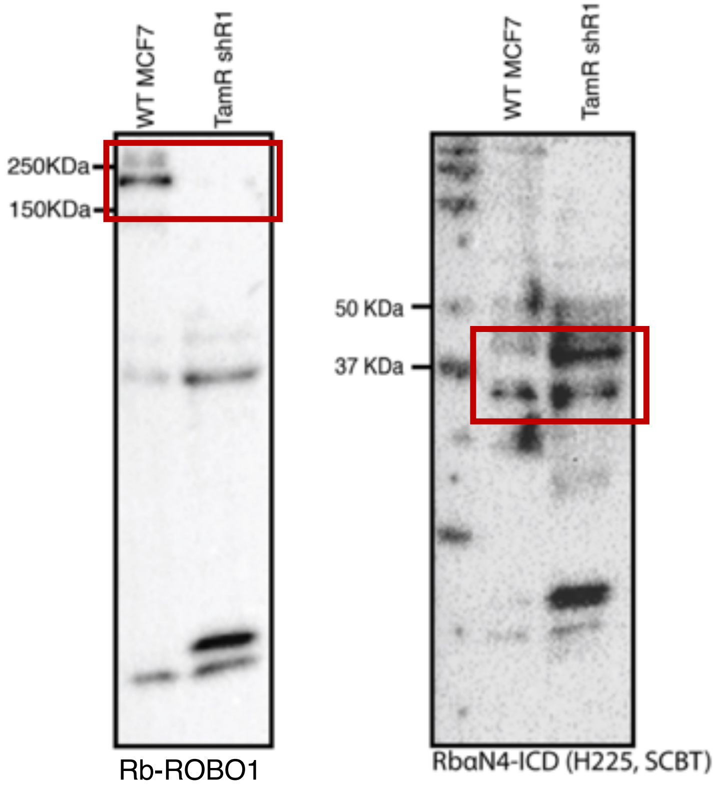

Figure 4.2 Loss of ROBO1 leads to an increase in the expression of the NOTCH4 intracellular domain (N4$_{ICD}$).

(Left) The expression of ROBO1 is analyzed using western blotting. Whole cell lysates from MCF7 cells show little to no expression in the Robo1 knock-down cells in comparison to the control wild type cells. N=1.

(Right) The shR1 cells also show an increase in NOTCH$ expression in comparison to the control wild type cells. N=1.

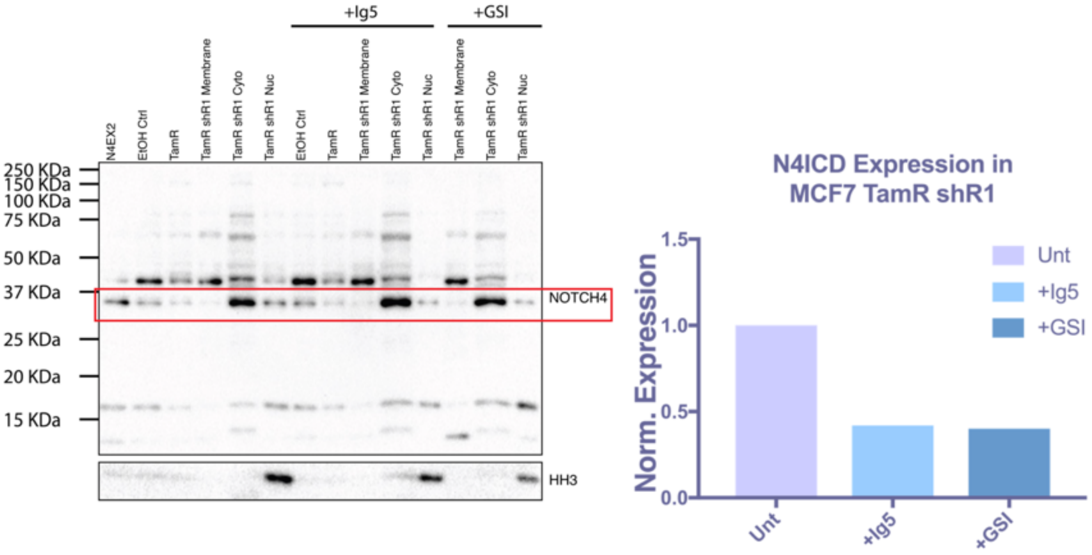

Figure 4.4 The nuclear localization of $N4_{ICD}$ is regulated by ROBO1.

Western blot analysis of NOTCH4 intracellular domain (ICD) expression outlined by the red box. The wildtype sample (well 6) shows more Notch4 ICD in comparison to the samples treated with Robo1-Ig5 (well 11) and GSI (well 14). Well 1, 6 and 11 are quantified in the plot. The nuclear Notch4 expression is normalized to the Histone H3 (HH3) loading control. N=1.

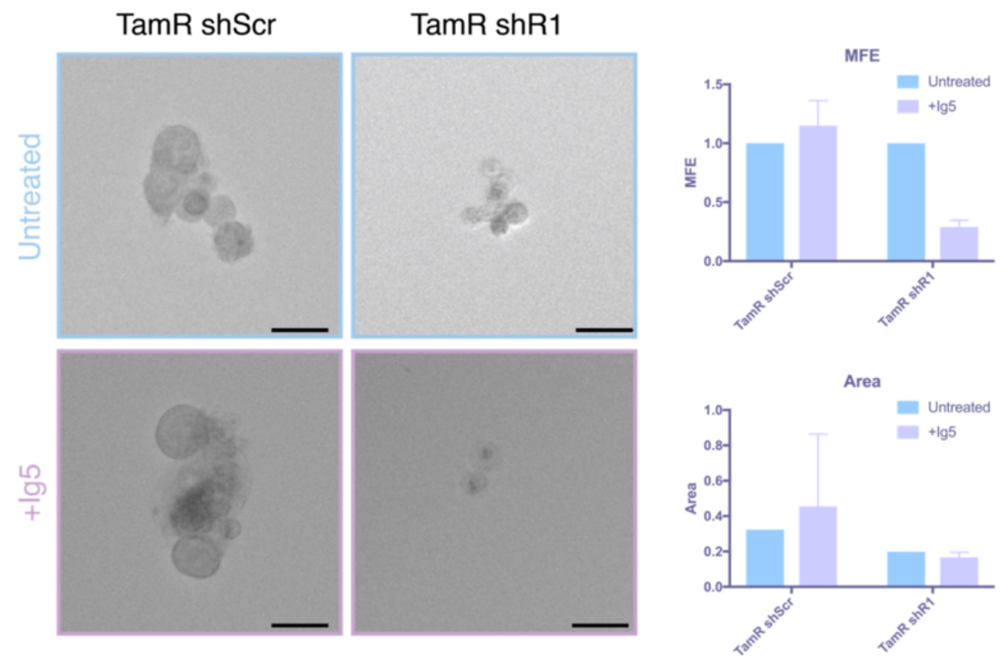

Figure 4.4 ROBO1 decreases the mammosphere formation efficiency of MCF7 cells.

Brightfield images of mammospheres from MCF7 cells that are Tamoxifen resistant and have been infected with lentivrus constructs specific for control shScramble (shScr) and *Robo1* knock-down (shR1). These stable cell lines were used to measure the mammosphere formation efficiency (MFE) of shR1 in comparison to shScr treated or untreated with Ig5. Only, the MFE of the shR1 cells was decreased with the Ig5 treatment after 5 days. The area of these cells was unchanged by the Ig5 treatment.

METHODS AND MATERIALS

Tissue Culture and Mammospheres

MCF7 cells were grown on tissue culture treated dishes until about 80% confluent. In preparation for mammospheres, the cells were detached from the TC dishes and dissociated into single cells. The cells were detached using Trypsin/EDTA 0.05% and dissociated into single cells using a 26G needle. Once the cells are counted, 1000 cells per well were used for each condition and allowed to grow into mammospheres undisturbed for 5 days ± treatment. The mammosphere formation efficiency (MFE) was calculated by dividing the number of mammospheres formed (≥50 μm) by the original number of single cells seeded (1000 cells per well) and is expressed as fold change normalized to control (Shaw et al., 2012).

Western Blotting

Subcellular fractionation was done as reported previously (Baghirova *et al.*, 2015). Whole cell lysates were collected using RIPA buffer. Protein expression was determined by running the lysates dissolved in equal volume of 2X Laemli Buffer on an SDS-Page gel for 1.5 hours at 100 V. The proteins were transferred to a PVDF membrane for 1.5 H at 400 mA and blocked using 5 % Non-fat dry milk rocking at room temperature for 1 hour. Primary antibody (in 5 % BSA) incubation was done overnight on a rocking platform at 4 ˚C. Membranes were washed 3X using TBST-High Salt for 5 minutes on a rocking surface at room temperature before being incubated with a secondary antibody, that is specific to the species of the primary antibody and tagged with Horseradish Peroxidase (HRP), for 45 minutes in 5% Non-fat dry milk rocking at room temperature. The membranes were washed 3X using TBST-High Salt and 1X using TBST-Low Salt for 5 minutes rocking at room temperature. Protein expression was determined relative to a house keeping protein specific to each cell compartment probed.

REFERENCES

1. Alluri, P.G., Speers, C., Chinnaiyan, A.M., 2014. Estrogen receptor mutations and their role in breast cancer progression. Breast Cancer Res. 16, 1–8. [PubMed: 25928204]

2. Aleksandrova N, Gutsche I, Kandiah E, Avilov SV, Petoukhov MV, Seiradake E, McCarthy AA. Robo1 Forms a Compact Dimer-of-Dimers Assembly. Structure. 2018 Feb 6;26(2):320-328.e4. [PubMed: 29307485]

3. Ballard, M.S., Hinck, L., 2012. A Roundabout Way to Cancer, 1st ed, Advances Cancer Research. Elsevier Inc. [PubMed: 22588058]

4. Ballard, M.S., Zhu, A., Iwai, N., Stensrud, M., Mapps, A., Postiglione, M.P., Knoblich, J.A., Hinck, L., 2015. Mammary Stem Cell Self-Renewal Is Regulated by Slit2/Robo1 Signaling through SNAI1 and mINSC. Cell Rep. 13, 290–301. [PubMed: 26440891]

5. Bashaw GJ, Kidd T, Murray D, Pawson T, Goodman CS. Repulsive axon guidance: Abelson and Enabled play opposing roles downstream of the roundabout receptor. Cell. 2000; 101:703–715. [PubMed: 10892742]

6. Brose K, Bland KS, Wang KH, Arnott D, Henzel W, Goodman CS, Tessier-Lavigne M, Kidd T. Slit proteins bind Robo receptors and have an evolutionarily conserved role in repulsive axon guidance. Cell. 1999; 96:795–806. [PubMed: 10102268]

7. Chang, M., 2012. Tamoxifen resistance in breast cancer. Biomol. Ther. 20, 256–267. [PubMed: 24130921]

8. Chen JH, Wen L, Dupuis S, Wu JY, Rao Y. The N-terminal leucine-rich regions in Slit are sufficient to repel olfactory bulb axons and subventricular zone neurons. J Neurosci. 2001; 21:1548–1556. [PubMed: 11222645]

9. Dallol A, Da Silva NF, Viacava P, Minna JD, Bieche I, Maher ER, Latif F. SLIT2, a human homologue of the Drosophila Slit2 gene, has tumor suppressor activity and is frequently inactivated in lung and breast cancers. Cancer Res. 2002a; 62:5874–5880. [PubMed: 12384551]

10. Fan, P., Craig Jordan, V., 2019. New insights into acquired endocrine resistance of breast cancer. Cancer Drug Resist. 2, 198–209. [PubMed: 31815253]

11. Hanker, A.B., Sudhan, D.R., Arteaga, C.L., 2020. Overcoming Endocrine Resistance in Breast Cancer. Cancer Cell 37, 496–513. [PubMed: 32289273]

12. Harburg, G., Compton, J., Liu, W., Iwai, N., Zada, S., Marlow, R., Strickland, P., Zeng, Y.A., Hinck, L., 2014. SLIT/ROBO2 signaling promotes mammary stem cell senescence by inhibiting wnt signaling. Stem Cell Reports 3, 385–393. [PubMed: 25241737]

13. Hinck L. The versatile roles of “axon guidance” cues in tissue morphogenesis. Dev Cell. 2004; 7:783–793. [PubMed: 15572123]

14. Hultsch, S., Kankainen, M., Paavolainen, L., Kovanen, R.M., Ikonen, E., Kangaspeska, S., Pietiäinen, V., Kallioniemi, O., 2018. Association of tamoxifen resistance and lipid reprogramming in breast cancer. BMC Cancer 18, 1–14. [PubMed: 30143015]

15. Kidd T, Bland KS, Goodman CS. Slit is the midline repellent for the robo receptor in Drosophila. Cell. 1999; 96:785–794. [PubMed: 10102267]

16. Kramer SG, Kidd T, Simpson JH, Goodman CS. Switching repulsion to attraction: changing responses to slit during transition in mesoderm migration. Science. 2001; 292:737–740. [PubMed: 11326102]

17. Legg JA, Herbert JM, Clissold P, Bicknell R. Slits and Roundabouts in cancer, tumour angiogenesis and endothelial cell migration. Angiogenesis. 2008; 11:13–21. [PubMed: 18264786]

18. Liu Z, Patel K, Schmidt H, Andrews W, Pini A, Sundaresan V. Extracellular Ig domains 1 and 2 of Robo are important for ligand (Slit) binding. Mol Cell Neurosci. 2004; 26:232–240. [PubMed: 15207848]

19. Ma XJ, Wang Z, Ryan PD, Isakoff SJ, Barmettler A, Fuller A, Muir B, Mohapatra G, Salunga R, Tuggle JT, Tran Y, Tran D, Tassin A, Amon P, Wang W, Enright E, Stecker K, Estepa-Sabal E, Smith B, Younger J, Balis U, Michaelson J, Bhan A, Habin K, Baer TM, Brugge J, Haber DA, Erlander MG, Sgroi DC. A two-gene expression ratio predicts clinical outcome in breast cancer patients treated with tamoxifen. Cancer Cell. 2004; 5:607–616. [PubMed: 15193263]

20. Macias H, Moran A, Samara Y, Moreno M, Compton JE, Harburg G, Strickland P, Hinck L. SLIT/ROBO1 signaling suppresses mammary branching morphogenesis by limiting basal cell number. Dev Cell. 2011; 20:827–840. [PubMed: 21664580]

21. Marlow R, Binnewies M, Sorensen LK, Monica SD, Strickland P, Forsberg EC, Li DY, Hinck L. Vascular Robo4 restricts proangiogenic VEGF signaling in breast. Proc Natl Acad Sci U S A. 2010; 107:10520–10525. [PubMed: 20498081]

22. Marlow R, Strickland P, Lee JS, Wu X, Pebenito M, Binnewies M, Le EK, Moran A, Macias H, Cardiff RD, Sukumar S, Hinck L. SLITs suppress tumor growth in vivo by silencing Sdf1/Cxcr4 within breast epithelium. Cancer Res. 2008; 68:7819–7827. [PubMed: 18829537]

23. Morlot C, Thielens NM, Ravelli RB, Hemrika W, Romijn RA, Gros P, Cusack S, McCarthy AA. Structural insights into the Slit-Robo complex. Proc Natl Acad Sci U S A. 2007b; 104:14923–14928. [PubMed: 17848514]

24. Plump AS, Erskine L, Sabatier C, Brose K, Epstein CJ, Goodman CS, Mason CA, Tessier-Lavigne M. Slit1 and Slit2 cooperate to prevent premature midline crossing of retinal axons in the mouse visual system. Neuron. 2002; 33:219–232. [PubMed: 11804570]

25. Prasad A, Paruchuri V, Preet A, Latif F, Ganju RK. Slit-2 induces a tumor-suppressive effect by regulating beta-catenin in breast cancer cells. J Biol Chem. 2008; 283:26624–26633. [PubMed: 18611862]

26. Rhee J, Buchan T, Zukerberg L, Lilien J, Balsamo J. Cables links Robo-bound Abl kinase to N-cadherin-bound beta-catenin to mediate Slit-induced modulation of adhesion and transcription. Nat Cell Biol. 2007; 9:883–892. [PubMed: 17618275]

27. Simões BM, O'Brien CS, Eyre R, Silva A, Yu L, Sarmiento-Castro A, Alférez DG, Spence K, Santiago-Gómez A, Chemi F, Acar A, Gandhi A, Howell A, Brennan K, Rydén L, Catalano S, Andó S, Gee J, Ucar A, Sims AH, Marangoni E, Farnie G, Landberg G, Howell SJ, Clarke RB. Anti-estrogen Resistance in Human Breast Tumors Is Driven by JAG1-NOTCH4-Dependent Cancer Stem Cell Activity. Cell Rep. 2015 Sep 29;12(12):1968-77. [PubMed: 26387946]

28. Stein E, Tessier-Lavigne M. Hierarchical organization of guidance receptors: silencing of netrin attraction by slit through a Robo/DCC receptor complex. Science. 2001; 291:1928–1938. [PubMed: 11239147]

29. Viedma-RodríGuez, R., Baiza-Gutman, L., Salamanca-Gómez, F., Diaz-Zaragoza, M., Martínez-Hernández, G., Esparza-Garrido, R.R., Velázquez-Flores, M.A., Arenas-Aranda, D., 2014. Mechanisms associated with resistance to tamoxifen in estrogen receptor-positive breast cancer (review). Oncol. Rep. 32, 3–15. [PubMed: 24841429]